이학박사 학위논문

Neural circuits for behavioral regulation of homeostasis: ingestive and thermoregulatory behaviors

행동적 항상성 조절의 신경회로: 섭식 행동과 체온조절 행동 중심으로

2022년 8월

서울대학교 대학원

협동과정 뇌과학 전공

김 동 윤

Neural circuits for behavioral regulation of homeostasis: ingestive and thermoregulatory behaviors

지도 교수 김 성 연

이 논문을 이학박사 학위논문으로 제출함

2022년 8월

서울대학교 대학원

협동과정 뇌과학 전공

김 동 윤

김동윤의 이학박사 학위논문을 인준함

2022년 7월

위 원 장 최 세 영 (인)

부위원장 김 성 연 (인)

위 원 이 용 석 (인)

위 원 최 명 환 (인)

위 원 김 대 수 (인)

Abstract

Maintaining physiological conditions (e.g., nutrients, water, and body temperature) within a narrow range is a distinct quality of living organisms. Among them, animals utilize diverse behaviors to suffice materials in need to maintain internal stability, called homeostasis. As such, understanding the neural mechanisms for behavioral regulations of homeostatic conditions has been a key interest in neurobiology and physiology. However, despite the importance of this question, neural processes underlying some of the fundamental behaviors for maintaining organismal homeostasis are still elusive. In this dissertation, I describe the data revealing neural circuit mechanisms underlying two basic behaviors for regulating homeostasis: ingestive and thermoregulatory behaviors.

Chapter one of this dissertation briefly overviews the origin of the homeostasis concept and provides a short historical perspective on studying neural processes for behavioral regulation of homeostasis. Chapter two describes a molecularly defined neural population in a hindbrain area called the parabrachial nucleus for monitoring and suppressing ingestion and demonstrates a gut-to-brain neural circuit spanning from the peripheral sensory ganglia to the hypothalamus for mechanosensory feedback control of ingestion.

Chapter three describes a parabrachial-to-hypothalamic neural circuit for thermoregulatory behaviors and the neural coding of motivational aspects of thermal stimuli by a subpopulation of hypothalamic neurons. Chapter four describes a summary of the data presented in this dissertation and provides directions for further investigations. Together, this dissertation presents studies on understanding neural circuit mechanisms underlying fundamental behaviors for regulating crucial homeostatic conditions, including energy, fluid, and body temperature.

Keywords: homeostasis, neural circuit, ingestive behavior, thermoregulatory behavior
Student Number: 2016-20453

Acknowledgements

I am deeply grateful to my advisor, Sung-Yon Kim, for giving me the opportunity to join the lab and teaching me patiently and passionately throughout my Ph.D. period. The past six years in graduate school were indeed a season of growth as a scientist and he has been a great mentor and a role model. I am thankful that I had the chance to learn from him.

I am also grateful to my dear colleagues and friends, Gyuryang, Minyoo, Sieun, and Myungsun, from whom I have learned so many things in terms of both science and life. All work presented here would not have been possible without them. I would also like to thank all previous and current K-Lab members for being my friends and teachers. I understand more and more that our bonds are so special and will last for a lifetime in terms of both research colleagues and friends. I also learned a lot from professors and friends outside the lab whom I would like to thank for giving me important input in my short research life.

I would also like to thank the committee members, Prof. Se-Young Choi, Yong-Seok Lee, Myunghwan Choi, and Daesoo Kim for their valuable comments and advice.

Lastly, I have my family members to thank for giving me invaluable support during this challenging period: my parents and sister; father and mother-in-law; and finally, but most importantly, my wife, Minjung, for being my beloved friend on this eternal journey of life.

The material in this dissertation is reprinted with permission from the following publications:

D.-Y. Kim*, G. Heo*, M. Kim*, H. Kim, J. A. Jin, H.-K. Kim, S. Jung, M. An, B. H. Ahn, J. H. Park, H.-E. Park, M. Lee, J. W. Lee, G. J. Schwartz, S.-Y. Kim, A neural circuit mechanism for mechanosensory feedback control of ingestion. *Nature*. 580, 376-380 (2020). * These authors contributed equally

S. Jung*, M. Lee*, D.-Y. Kim*, C. Son, B. H. Ahn, G. Heo, J. Park, M. Kim, H.-E. Park, D.-J. Koo, J. H. Park, J. W. Lee, H. K. Choe, S.-Y. Kim, A forebrain neural substrate for behavioral thermoregulation. *Neuron*. 110, 266-279.e9 (2022). *These authors contributed equally

The co-authors of the above papers gratefully agreed to use the figures and materials, which was inevitable due to the difficulties in separating materials corresponding to the contribution of the co-authors. The practice of reusing the data and figures used in the published papers listed above by multiple co-authors for their dissertations has been consulted by the Research Ethics Team at Seoul National University.

Table of Contents

Chapter 1. Introduction

> *A fairly constant or steady state, maintained in many aspects of the bodily economy even when they are beset by conditions tending to disturb them, is a most remarkable characteristic of the living organism.* —Walter B. Cannon, 1925

This statement reflects the view that maintaining stability against external forces or environmental changes is one of the most peculiar qualities of living organisms. Shortly after addressing this argument, Walter Bradford Cannon coined and defined the term *homeostasis* which indicates the attribute of living beings in his remarkable review paper, *Organization for physiological homeostasis* (*1*). Homeostasis is a compound of two Greek words: *homeo* (meaning "like" or "similar") and *stasis* (meaning "standing still" or "stagnation"). By choosing the term *homeo* rather than *homo* (meaning "same" or "fixed"), Cannon intended to describe the concept that internal variables of living organisms are maintained 1) within a narrow range (rather than a fixed value) 2) by active and dynamic stabilization against environmental changes. Despite his neologism, Cannon attributed the general ideas regarding the concept of homeostasis to many

prominent figures before his era, and, particularly, he thought the first credit belonged to a French physiologist, Claude Bernard (*1*). "[Bernard] pointed out that in animals with complex organization the living parts exist in the fluids which bathe them, i.e., in the blood and lymph, which constitute the "melieu interne" or "intérieur" —the internal environment, or what we may call the fluid matrix of the body," Cannon wrote (*1*). To Bernard, the teleology and the most distinct quality of some higher living beings were maintaining the condition of their internal environment. He wrote that "all the vital mechanisms, however varied they may be, have only one object, that of preserving constant the conditions of life in the internal environment (cited in (*1*))."

After defining the term homeostasis, Cannon further discussed the physiological and neuronal mechanisms by which organisms maintain various homeostatic conditions like the amounts of internal materials (e.g., nutrients, water, and ions) and the environmental factors affecting cellular functions (e.g., temperature and osmotic pressure). Interestingly, in a section of this part, he shortly mentioned the critical regulatory functions of hunger and thirst (which induce motivated behaviors like eating and drinking) for material supplies (*1*). It shows that he was already aware of the role of behaviors in regulating homeostasis, even though his review

mainly focuses on the autonomic and metabolic functions in maintaining homeostasis. Accordingly, numerous prominent philosophical, psychological, and physiological perspectives emerged over the next few decades on behavioral regulation of internal needs (*2–5*).

Naturally, numerous classic neuroscience discoveries in that era focused on identifying brain areas involved in controlling homeostatic behaviors (*6*, *7*). For example, electrical and pharmacological activation of brain areas was shown to elicit behavioral responses satiating internal needs such as eating (*8*, *9*), drinking (*10*, *11*), thermoregulation (*12*), and sexual behaviors (*13*). On the other hand, electrical lesions in some brain regions were shown to impair the behavioral responses of animals in the need states (*14–18*). These studies have established many brain areas (especially those in the hypothalamus) as critical brain nodes for homeostatic behaviors. However, at the same time, the classical approaches (i.e., region−specific stimulations and lesions) revealed some significant concerns and problems. For example, electrical stimulation of a brain area, the lateral hypothalamus, elicited multiple homeostatic behaviors, including eating, drinking, and some social behaviors (*19*, *10*, *13*, *20*). It implied the cellular and functional heterogeneity of an anatomically defined brain area.

Indeed, in the next phase of neuroscience research focusing on the role of neuropeptides, it has been revealed that a brain region contains diverse neurochemically defined neuronal subpopulations engaged in various functions. In addition, different types of neurons imposing opposite behavioral responses could be intermingled in the same area (*7*). A typical example is the cellular composition of arcuate nucleus of the hypothalamus (ARC), which contains both neurons expressing orexigenic peptide, agouti-related protein (AgRP), and those expressing anorexigenic peptide, α-melanocyte stimulating hormone (which is derived from the precursor, proopiomelanocortin, or POMC) (*7*). This neurochemical or molecular complication of brain areas implies the requirement of tools to specifically target molecularly defined neuronal subpopulations, or cell types, to elucidate their designated homeostatic functions.

Indeed, modern neuroscience research studying the neural circuits for homeostatic behaviors seems to largely rely on the genetic toolbox that allows us to manipulate and monitor the activities of molecularly defined neuronal cell types (*7*, *21-24*). For example, optogenetics and chemogenetics have enabled the activation or inhibition of neural activities by expressing opsins or GPCRs in a specific cell type (*22*, *25-27*). Genetically encoded

calcium indicators allowed us to monitor neuronal activities of neuronal subpopulations (*28*, *29*), and viral tools are being actively used to define anatomical connections of molecularly defined neuronal populations (*30*–*33*). This rapidly expanding neurobiology toolbox has led the field to reveal numerous designated neural circuits for the regulation of homeostatic behaviors such as eating (*6*, *34*–*39*), drinking (*40*, *41*), social behaviors (*42*–*44*), and so forth. Now we have countless example studies examining the role of molecularly identified neural circuits for homeostatic behaviors; however, there remain many fundamental questions regarding how we maintain the internal environment or *melieu intérieur*. By using state-of-the-art neuroscience techniques, this research aims to identify molecularly defined neural circuits for two basic behaviors for regulating homeostasis: first, I identify a gut-brain neural circuit that mediates mechanosensory feedback from the gastrointestinal tract to regulate ingestive behaviors; second, I establish a neural substrate that is critical for the manifestation of diverse thermoregulatory behaviors.

Chapter 2. A neural circuit mechanism for mechanosensory feedback control of ingestion*

Abstract

Mechanosensory signals from the digestive tract to the brain is crucial for regulating food and water intake, however, the underlying gut-to-brain communication pathways and mechanisms are still poorly understood (*4*, *34*, *40*, *45-53*). Here, I demonstrate that prodynorphin-expressing neurons in the parabrachial nucleus (PB^{Pdyn} neurons) monitor the intake of liquids and solids, using mechanosensory signals from the upper digestive tract. The majority of individual PB^{Pdyn} neurons are activated by ingestion and the stimulation of the mouth and stomach, indicating the representation of integrated sensory inputs across distinct digestive tract organs. I also reveal that PB^{Pdyn} neurons are connected to the digestive periphery via cranial and spinal pathways; among these pathways, the vagus nerve transmits the stomach distension signals to these neurons. Activation of PB^{Pdyn} neurons is avoided and

---

* The material in this chapter is reprinted from:

D.-Y. Kim*, G. Heo*, M. Kim*, H. Kim, J. A. Jin, H.-K. Kim, S. Jung, M. An, B. H. Ahn, J. H. Park, H.-E. Park, M. Lee, J. W. Lee, G. J. Schwartz, S.-Y. Kim, A neural circuit mechanism for mechanosensory feedback control of ingestion. *Nature*. 580, 376-380 (2020). * These authors contributed equally

produces sustained appetite-suppressing signals to discourage the initiation of eating and drinking, which fully recapitulates the symptoms of gastric distension, in part via signaling to the paraventricular hypothalamus (PVH). In contrast, the inhibition of the same population induces overconsumption only when a drive for ingestion exists, confirming that PB^{Pdyn} neurons mediate negative feedback signaling. Together, these findings provide a neural circuit mechanism underlying mechanosensory monitoring of ingestion (*4*, *34*, *40*, *45–53*) and negative feedback control of ingestive behaviors upon digestive tract mechanosensation (*4*, *53*).

2.1. Introduction

Multiple aspects in organismal homeostasis, including the cellular nutrient, osmolality levels and the volume of digestive organs, depend on the proper regulation of food and water intake (*45–47*, *34*, *48*, *40*, *49–51*). Unchecked consumption can mechanically harm the gastrointestinal tract tissues, burden the functions of digestive and excretory organs, and disturb the balance of nutrients and fluids. These effects are harmful to animals, as exemplified by obesity, overhydration-induced hyponatremia, seizure and cerebral edema (*49*, *50*).

To avoid adverse consequences, animals use negative

feedback signals originating from the chemosensory and mechanosensory modalities of the digestive tract organs, such as the oropharyngeal cavity (*40*, *48–51*) and the stomach (*4*, *51–55*)) for monitoring and limiting consumption (*4*, *34*, *40*, *45–53*). In contrast to the chemosensory modalities underlying taste, nutrition detection and osmolality (*56–61*), mechanosensation in the digestive system offers information on the amount of intake regardless of the content of ingesta (*45–47*, *34*, *48*, *40*, *49–52*). Classic studies have demonstrated that stomach distension inhibits both drinking and eating, is avoided, and that vagal and spinal afferents are involved in its signaling (*4*, *46*, *47*, *51–53*). Recently, it was discovered that a certain population of vagal afferents can detect gastrointestinal distension (*62*) and suppresses consumption (*63*). However, a specific neuronal population in the brain encoding mechanosensation from the gastrointestinal tract organs has not yet identified, and the gut–brain neural circuit mechanism underlying negative mechanosensory feedback signaling for reducing appetite remains largely unknown.

Four cranial (CN V, VII, IX and X) and spinal afferents innervate the digestive tract extensively, conveying oral, oropharyngeal and visceral sensory signals to the caudal part of the hindbrain (*34*, *45–47*, *64*). Cranial nerve afferents and spinal

afferent collaterals converge on the nucleus solitary tract (NTS), with afferents originating from various organs innervating subregions of the NTS in a viscerotopic 'labeled-line' fashion (*34*, *64-66*). Along with spinal collaterals, the NTS projects to the parabrachial nucleus (PB) (*67*, *68*). The PB then innervates multiple midbrain and forebrain regions implicated in drinking and feeding (*68*, *69*). Given this architecture, the PB is well adapted to play a significant role in mechanosensory monitoring and feedback regulation of ingestive behaviors. Indeed, through lesion, pharmacological interventions, neural activity manipulations and recordings, the PB has been suggested to regulate intake behaviors (*34*, *50*, *54*, *70*, *71*). Thus, I focused on the PB to identify a molecularly defined subpopulation that encodes mechanosensory signals that emerge from the digestive tract upon consumption and transmits appetite-suppressing signals.

2.2. PB^{Pdyn} neurons monitor ingestion of both liquids and solids

I started by looking at a marker for PB neurons signaling water intake, as an index of overall consumption. I first found that water intake in dehydrated mice showed a robust expression of a neural activity marker Fos in the dorsolateral subnucleus of the PB (PBdl);

where prodynorphin-encoding *Pdyn* gene is highly expressed (Figure 1a). Then, I used mice in which $Pdyn^{+}$ neurons were fluorescently labeled and found that ~80% of Fos^{+} neurons were $Pdyn^{+}$, and ~72% of $Pdyn^{+}$ neurons were Fos^{+} in the PBdl, which indicates *Pdyn* as a useful genetic marker for targeting water intake-activated neurons in the PB (Figures 1b-d). *In situ* hybridization uncovered that PB^{Pdyn} neurons are glutamatergic, partially overlaps with $Oxtr^{+}$ neurons (*71*), but are separate from $Calca^{+}$ neurons that are implicated in noxious visceral signaling (*72*) and meal termination (*68*) (Figure 1e).

To monitor the real-time activity of PB^{Pdyn} neurons in behaving mice, I performed fiber photometry recordings from GCaMP-expressing PB^{Pdyn} neurons (Figure 2a). Surprisingly, when mice drank water, PB^{Pdyn} neurons were acutely activated, and when mice stopped drinking, their activity quickly returned to the baseline level (Figures 2b, c). The act of licking was not sufficient to activate these neurons; there was no response to empty spout licking (Figures 2c, 3b, 3c). In addition, PB^{Pdyn} neurons were also activated by the consumption of various fluids (liquid food, basic bicarbonate solution, hypertonic saline, and silicone oil) and solids (hydrogel and chow food) (Figures 2c-e). I observed a considerable positive correlation between the response amplitude of

PB^{Pdyn} neurons and the intake rate across the intake of diverse fluids and solids (Figures 2f, 4c, 4d). Thus, the intake of either fluids or solids activates PB^{Pdyn} neurons, and the response amplitude of this population scales with the rate of consumption. This suggests that PB^{Pdyn} neurons use mechanosensory signals from the digestive tract to monitor ingestion.

2.3. PB^{Pdyn} neurons receive mechanosensory signals from the upper digestive tract organs

I applied a variety of mechanical stimuli to the upper digestive tract components to directly test this hypothesis. First, PB^{Pdyn} neurons did respond vigorously when the tongue was touched with a gavage needle (Figure 2g). These neurons were also robustly activated when the gavage needle was inserted into the esophagus, touching and stretching the esophageal wall (Figure 2h). In addition, PB^{Pdyn} neurons demonstrated a inflation rate–dependent response to intragastric balloon inflation (Figures 2i–k). The activity of these neurons decreased as the balloon was deflated and no prolonged activity followed; maintaining balloon inflation for a long time demonstrated adaptation–like responses that resembled the responses of vagal afferents and mechanosensory PB neurons to stomach distension (*73*, *74*). Locally pressing the stomach wall also

robustly stimulated PB^{Pdyn} neurons, and direct infusion of liquids or air in each part of the upper digestive tract using a gastric catheter or oral gavage activated these neurons (Figures 3d–l, 4a, 4b). In contrast, the balloon–mediated distension of either the duodenum or proximal colon did not significantly activate PB^{Pdyn} neurons (Figures 2l, 2m, 4e, 4f). Therefore, I could conclude that PB^{Pdyn} neurons respond to mechanosensation from the upper digestive tract organs.

In a series of control experiments, I observed that taste, osmolality or temperature of ingesta do not modulate the responses of PB^{Pdyn} neurons (Figure 3m–p). Additionally, I discovered that the PB^{Pdyn} population's activity was unrelated to general movement or anxiety and that these neurons were not responsive to dorsum stroke, sensory detection of peanut butter, whisker touch, and conditioned tone predicting water delivery (Figure 5). Moreover, neither PB^{Pdyn} neurons' basal activity nor their responses were modulated by the internal need state (Figure 6). Collectively, these findings indicate that PB^{Pdyn} neurons play a crucial role in signaling interoceptive mechanosensation from the upper digestive tract to monitor ingestion.

2.4. Individual PB^{Pdyn} neurons represent integrated

mechanosensory signals

Considering that the PB^{Pdyn} population is stimulated by a variety of ostensibly different stimuli, such as water and food intake and mechanical stimulation of digestive tract organs, I used two-photon microscopy to examine how these stimuli are represented by individual PB^{Pdyn} neurons (Figures 7a, b). I first investigated the representation of ingestion. Water and liquid food intake acutely and strongly activated ~82% and ~75% of PB^{Pdyn} neurons, respectively, which is in line with our Fos experiments (Figures 7c-e). Interestingly, registration of neurons across trials showed that these two populations largely overlapped one another (Figure 7f), and there was a linear correlation between their response amplitudes (Figure 7g). Therefore, most PB^{Pdyn} neurons respond to the ingestion of both liquid food and water.

I next investigated the representation of gastric distension (Figure 7h). I found strong activation in the majority of PB^{Pdyn} neurons (Figures 7i, j)., which is consistent with the findings from fiber photometry recordings (Figures 2i-k. Importantly, as the inflation volume increased, both the response strength and the number of neurons that were activated were increased (Figure 7k-m). I also monitored how PB^{Pdyn} neurons responded when a liquid drop (10 μl) was delivered orally (Figure 7n). Similar strong

responses were elicited by this stimulation in a high percentage of PB^{Pdyn} neurons (76.3%) (Figures 7o, p). Surprisingly, registration of neurons across imaging experiments showed that the majority of PB^{Pdyn} neurons responded to all of the following: water intake, stomach distension, and oral liquid drop administration (Figure 7q). These include the stimuli delivered by different cranial and spinal nerve pathways (*34*, *45*, *47*, *49*, *64*, *65*, *75*). The majority of PB^{Pdyn} neurons, therefore, represent the integrated visceral mechanosensory signals from diverse digestive tract parts. Furthermore, these findings also significantly support the idea that PB^{Pdyn} neurons monitor intake using integrated mechanosensory signals from distinct digestive tract organs because the same neurons are engaged by both the ingestion and digestive tract distension.

2.5. Vagus nerves relay stomach-distension signals to PB^{Pdyn} neurons

How do PB^{Pdyn} neurons receive the mechanosensory signals from the digestive tract organs? To tackle this question, I used engineered rabies viruses to map the monosynaptic inputs of PB^{Pdyn} neurons (Figure 8a, see Methods). The input neurons were observed throughout the brain; the trigeminal nerve nuclei and

certain NTS subregions, which receive oral, oropharyngeal, and visceral sensory information provided by the trigeminal, facial, glossopharyngeal, and vagus nerves (*65*), were particularly notable locations (Figures 8b, 8c, and 9a). By the additional synaptic spread of the virus from the NTS or the trigeminal nucleus, which are primary sensory nuclei, we found input neurons in the sensory cranial ganglia (Figures 8d, 8e, 9b–e), showing the anatomical connections between cranial afferent pathways and PB^{Pdyn} neurons.

Although it is widely thought that the spinal and vagal pathways, respectively, relay visceral and physiological gastric distension signals (*64*, *76*), some studies have suggested that spinal afferents may also play a key role in mechanosensory feedback signaling of consumption (*47*, *76*). Indeed, I also found direct inputs from neurons in the dorsal horn to PB^{Pdyn} neurons (Figure 9a). Therefore, I explored if spinal transection or vagotomy abolished PB^{Pdyn} neurons' responses to stomach distension in order to identify the pathway relaying mechanosensory signals to PB^{Pdyn} neurons (see Methods). Remarkably, subdiaphragmatic vagotomy completely abolished the responses, while spinal transaction did not (Figures 8f–k, 9f, 9g). Therefore, vagal, not spinal, pathways are used to relay mechanosensory signals from the gut to PB^{Pdyn} neurons. I also discovered that intraperitoneal injection of

cholecystokinin (CCK), a gut hormone that has been demonstrated to stimulate gastric distension-sensitive vagal afferents (*62*, *73*), activates PB^{Pdyn} neurons, supporting the idea that PB^{Pdyn} neurons get stomach distension signals through mechanosensory vagal fibers (Figure 9h).

2.6. PB^{Pdyn} neurons suppress ingestion

I next sought to probe the causative role of PB^{Pdyn} neurons by using optogenetic and chemogenetic tools. Surprisingly, food and water intake were potently decreased by chemogenetic activation of PB^{Pdyn} population, and these effects were mediated by a decrease in bout number, but not bout duration (Figures 10a-c, 11a). When PB^{Pdyn} neurons were briefly stimulated optogenetically upon the detection of each lick or throughout the entire session, fluid intake was decreased by a decrease in the number of bouts as well (Figures 10d, 10e, 11b-j). Therefore, rather than terminating initiated intake bouts, PB^{Pdyn} neuronal activation suppresses ingestion by deterring the initiation of bouts. Importantly, the effect of stimulating PB^{Pdyn} neurons resembles the symptoms of stomach distension, since stomach distension similarly lowers water intake by reducing bout number, rather than bout duration (*77*) (Figures

11l–s). This indicates that PB^{Pdyn} neurons may mediate the appetite suppression induced by the distension of digestive tract organs.

I further explored the causative roles of PB^{Pdyn} neurons to gain insights into how these neurons suppress intake. I discovered that PB^{Pdyn} neurons convey a negative–valence signal (Figures 10f, 11k), which is consistent with previous discoveries that stomach distension is avoided (*4*). On the other hand, our findings that PB^{Pdyn} neurons are most active at the start of intake and that lick–paired stimulations do not shorten bout duration imply that PB^{Pdyn} neurons produce sustained appetite–suppressing signals exerting effects over a prolonged time. Indeed, PB^{Pdyn} neuron pre–stimulation before water intake tests reduced drinking for at least 10 minutes (Figure 10g). As control results, I observed that PB^{Pdyn} neuron activation had no impact on social or anxiety–like behaviors (Figures 5i, j). Together, the data demonstrate, first, that PB^{Pdyn} neurons inhibits ingestive behaviors by conveying sustained appetite–suppressing signals, and, second, the effects of activating PB^{Pdyn} neurons closely resemble the symptoms of stomach distension.

2.7. PB^{Pdyn} neurons mediate negative feedback control of ingestion

To determine the physiological role of the signals transmitted by PB^{Pdyn} neurons, I then chemogenetically inhibited PB^{Pdyn} neurons (Figure 10h). Inhibiting these neurons increased the consumption of chow food in fasted mice (Figure 10i), and both water and hypertonic saline consumption in dehydrated mice (Figure 10j). Intriguingly, the inhibition of PB^{Pdyn} neurons did not alter the intake of either saline or water in euhydrated mice (Figure 10k), and did cause a tendency towards increased consumption of hypertonic saline (but not water) when the mice were salt-depleted (Figure 10l). Therefore, decreased PB^{Pdyn} neuron activity only results in overconsumption when there is already an appetite present, rather than increasing appetite by itself. This is similar to the effects brought on by loss-of-function manipulation of various gut-borne biochemical feedback signals (*55*). These findings demonstrate that PB^{Pdyn} neurons are necessary for the negative feedback regulation of ingestion. Together with the gain-of-function studies, our data show that PB^{Pdyn} neurons are both sufficient and necessary for suppressing appetite upon the distension of digestive tract organs.

To further investigate the circuit mechanism by which PB^{Pdyn} neurons regulate ingestion, I explored the output circuits. Projection

mapping showed that PB^{Pdyn} neurons densely innervate multiple brain regions crucial for ingestive behaviors (Figures 10m, 12a). Among the targets, we optogenetically stimulated the projections to the PVH (*78–81*), and this manipulation potently inhibited food and water intake and caused avoidance (Figures 10n–q, 12b, 12c), similar to the stimulation of PB^{Pdyn} neurons and stomach distension. Contrarily, stimulating subfornical organ (SFO) projections (*40*, *41*) had no effect on either drinking or feeding, but was avoided (Figures 10r–u). These findings imply that the PVH may be a key downstream target of PB^{Pdyn} neurons that, at least in part, mediates the inhibition of intake, which is probably done via recruiting some PVH subpopulations that are known to regulate appetite (*79–81*).

2.8. Discussion

One of the key issues in physiology is how drinking and eating are monitored and limited. This study establishes PB^{Pdyn} neurons as a crucial circuit node that monitor and control ingestion possibly by using mechanosensory signals. PB^{Pdyn} neuron activity appears to encode rapid changes of the digestive tract volume, instead of the steady–state volume of the digestive tract. By providing feedback signals that suppress appetite in proportion to the rate of ingestion, PB^{Pdyn} neurons may protect the organism from the potential risks

associated with excessive consumption. This is consistent with research that links PB neurons to alarming functions (*68*, *82*). Furth ermore, it is possible that PB^{Pdyn} neurons serve as a convergent node to integrate mechanosensory information from various upper digestive tract organs, according to our tracing and two-photon imaging data (74). An outstanding question is how and where the mechanosensory signals from different organs in the digestive tract are conveyed and merged to represent integrated signals.

Appetite can be suppressed by a competing motivational state, not only by satiating hunger or thirst (*4*, *34*, *49*, *55*, *68*, *83*). Since the distension of digestive tract organs does not fundamentally resolve thirst or hunger by replenishing water or nutrients, I hypothesize that PB^{Pdyn} neurons may introduce a anorexi c state, which competes with thirst or hunger; which is different from visceral malaise-induced anorexia which is known to be mediated by neurons located in the external lateral subdivision of the PB (*68*, *72*)). This may be mediated by neurons in the downs tream targets that are suggested to suppress appetite, such as $Pdyn^{+}$ (*80*) and Crh^{+} (*81*) neurons in the PVH, or $Prkcd^{+}$ neurons in the central amygdala (*84*) (which notably regulate the number of intake bouts, alike PB^{Pdyn} neurons). Further research could focus on the mechanism that PB^{Pdyn} neurons limit the initiation of ingestive

behaviors via downstream projection targets. On the other hand, the abundance of monosynaptic inputs to PB^{Pdyn} neurons throughout the brain suggests that these neurons are subject to upstream regulatory mechanisms.

2.9. Methods

Animals

Unless otherwise specified, all mice were housed in a temperature- and humidity-controlled room with a reverse 12-hour light/dark cycle and ad libitum access to chow food and water. For data collection, male and female mice of at least six weeks of age were used. The Jackson Laboratory provided C57BL/6J (JAX stock no. 000664), *Pdyn*$^{Cre/+}$ (JAX stock no. 027958), and Gt(ROSA)26Sor$^{tm14(CAG-tdTomato)Hze/J}$ (Ai14 mice; JAX stock no. 007914) mice. All of the mice used in the experiments were heterozygotes on the C57BL/6J background. *Pdyn*$^{Cre/+}$ mice were crossed with Ai14 mice for the Fos experiment to reveal expression patterns. Mice in each litter were assigned to either the experimental or control groups at random. During the dark cycle, all behavioral procedures were carried out. Mice were acclimated to the test room for at least 5 minutes prior to testing. Mice were fed or water-deprived to induce robust ingestive behaviors, which

allowed researchers to observe neural responses to fluid and food ingestion. Unless otherwise stated, water-deprived (dehydrated) or food-deprived conditions were induced by housing mice without water or food for 48 hours. The Seoul National University Institutional Animal Care and Use Committee approved all experimental protocols.

Viral constructs

The adeno-associated virus (AAV) vectors expressing GCaMP6m (AAV1-hSyn-FLEX-GCaMP6m, 1.2×10^{13} copies/ml) and tdTomato (AAV1-CAG-FLEX-tdTomato, 3.1×10^{12} copies/ml) were purchased from the Penn Vector Core, and the AAV vectors expressing ChR2 (AAV5-EF1α-DIO-hChR2(H134R)-eYFP, 3.2×10^{12} copies/ml) and eYFP (AAV5-EF1a-DIO-eYFP, 3.2×10^{12} copies/ml) were obtained from the UNC vector core. The AAV vector expressing hM3Dq (AAV8-hSyn-DIO-hM3D(Gq)-mCherry, 3.0×10^{12} copies/ml), hM4Di (AAV8-hSyn-DIO-hM4D(Gi)-mCherry, 4.0×10^{12} copies/ml), and mCherry (AAV9-hSyn-DIO-mCherry, 2.1×10^{12} copies/ml) was purchased from Addgene, and the AAV vectors expressing ChR2 (AAV-DJ-EF1a-DIO-hChR2(H134R)-eYFP, 4.7×10^{13} copies/ml), eYFP (AAV-DJ-EF1a-DIO-eYFP, 8.8×10^{12} copies/ml), Cre recombinase

(AAV-DJ-CMV-eGFP-Cre or AAV-DJ-EF1a-mCherry-IRES-Cre-WPRE), and mRuby-fused synaptophysin (AAV-DJ-hSyn-FLEX-GFP-2A-Synaptophysin-mRuby, 4.0 × 10^{13} copies/ml) were purchased from the Stanford Vector Core. The AAV vector expressing optimized rabies G protein (*85*) and enhanced-expression TVA receptor (*86*) (AAV8-DIO-TC66T-2A-oG, 1.64 × 10^{13} copies/ml), blue fluorescent protein (BFP)-fused rabies G protein (AAV1-EF1a-DIO-hBFP-RVG), and the recombinant EnvA-pseudotyped G-deficient rabies virus vector expressing GFP (RV-EnvA-⊿G-GFP) and mCherry (RV-EnvA-⊿G-mCherry) were purchased from the Salk vector core. Some rabies vectors (RV-EnvA-⊿G-GFP) were generously provided by B. K. Lim (University of California, San Diego).

Stereotaxic surgery

Mice were anesthetized with 1.5-3.0% isoflurane and placed in a stereotaxic apparatus (David Kopf Instruments) while resting on a heating pad. A small craniotomy, following a scalp incision, was made using a hand drill at the regions of interest. 100-300 nl of viral vectors were injected to the center of the lateral PB using a pressure injection system (Nanoliter 2000) using a pulled glass capillary at 40-100 nl min^{-1}. The coordinates for the PB were -5.4

mm antero-posterior (AP), ±1.25 mm medio-lateral (ML), -3.5 mm dorso-ventral (DV); in some mice, for more reliable targeting, or in the case of bilateral implants, I targeted the same region at -10 degree (-5.4 mm AP, ±0.6 mm ML, -3.5 mm DV) or 10 degree (-5.3 mm AP, ±1.8 mm ML, -3.1 DV) angle relative to the sagittal plane. The incision was closed using suture and tissue adhesive (Vetbond) and mice were provided with antibiotics and analgesics. Mice were placed in a clean cage on a heating pad to recover from anesthesia, and were kept in their home cage for 2-4 weeks for viral expression and recovery from surgery before behavioral testing. Except for the midline structures, the choice of left or right hemisphere was counterbalanced for all unilateral injections and implantations.

For fiber photometry experiments, recombinant AAVs expressing GCaMP6m were unilaterally injected into the PB of $Pdyn^{Cre/+}$ mice, and a low-autofluorescence 400 μm-core, 0.48 NA fiberoptic cannula (Doric lenses) was implanted 0-100 μm above the virus injection site. The fiberoptic cannulas were affixed to the skull with C&B Metabond (Parkell) and dental cement. For the experiments involving head fixation, a custom-made stainless steel bar (*87*) (4.0×1.0×1.0 mm^3) was attached to the dental cement during surgery to allow subsequent head fixation to a

custom-made station with complementary slots that can accommodate the tips of the attached bars.

For two-photon imaging experiments, GCaMP6m was expressed as above. A custom-built stainless steel blunt needle (0.5 mm diameter) was lowered to the target coordination to create enough hollow space for lens implantation. The needle was withdrawn after 30 min, and a microendoscopic lens (gradient refractive index (GRIN) lens; 6.1 mm length, 0.5 mm diameter; Inscopix 1050-002182) was immediately implanted directly above the PBdl (−5.4 mm AP, ±1.25 mm ML, −3.5 mm DV) at slightly different coordinates than the viral injection site (−5.2 mm AP, ± 1.25 mm ML, −3.5 mm DV) to avoid imaging autofluorescence usually found at the injection track. A custom-made stainless steel bar(*87*) (4.0×1.0×1.0 mm^3) or a ring (*88*) (3.5 mm ID, 11 mm OD) was attached to the dental cement during surgery for head fixation.

For cell soma optogenetic stimulation experiments, recombinant AAVs expressing ChR2 or eYFP were bilaterally injected into the PB of $Pdyn^{Cre/+}$ mice, and 200 μm-core, 0.22 NA fiberoptic cannulas (Newdoon) were bilaterally inserted 100-300 μm above the virus injection site. For some control groups, $Pdyn^{+/+}$ littermates were injected with AAVs expressing ChR2.

For chemogenetic stimulation or inhibition experiments, recombinant AAVs expressing hM3Dq, hM4Di or tdTomato, mCherry, and eYFP were bilaterally injected into the PB of *Pdyn*$^{Cre/+}$ mice.

For terminal optogenetic stimulation experiments, recombinant AAVs expressing ChR2 or eYFP were bilaterally injected into the PB of *Pdyn*$^{Cre/+}$ mice, and 200 μm-core fiberoptic cannulas were implanted above the SFO (−0.6 mm AP, 0 mm ML, −2.6 mm DV) or PVH (−0.6 mm AP, 0 mm ML, −4.2 mm DV).

For anterograde projection mapping experiments, recombinant AAVs expressing GFP and mRuby-fused synaptophysin were unilaterally injected into the PB of *Pdyn*$^{Cre/+}$ mice. After 3-4 weeks, mice were euthanized and processed for histology.

For rabies tracing experiments (*89*), recombinant AAVs carrying Cre-dependent TVA and G were injected into the PB of *Pdyn*$^{Cre/+}$ mice. After 3 weeks, recombinant EnvA-pseudotyped G-deficient rabies virus (RVdG) expressing GFP or mCherry was injected into the PB. RVdG selectively infects TVA-expressing PB^{Pdyn} neurons, and co-expression of G enables PB^{Pdyn} neurons to complement RVdG and produce infectious rabies viruses that spread to their direct presynaptic partners. After 8-15 days, mice were

euthanized and processed for histology. I note that 5 days of expression was insufficient for the complete labeling of the monosynaptic inputs to PB^{Pdyn} neurons. For additional trans-synaptic spread from the monosynaptic inputs to PB^{Pdyn} neurons, a mixture of recombinant AAVs carrying Cre recombinase and Cre-dependent G was injected into the NTS (−7.5 mm AP, ±0.4 mm ML, −5.4 mm DV) or Pr5 (−5.8 mm AP, ±1.4 mm ML, −4.9mm DV) of $Pdyn^{Cre/+}$ mice at the same time when AAVs carrying Cre-dependent TVA and G were injected into the PB. 8−15 days after RVdG injection, mice were euthanized and processed for histology.

Gastric and intestinal catheterization and balloon implantation

Intragastric catheters were constructed by penetrating a 6−mm diameter Dacron felt disc with a Silastic tubing (6 cm long, 0.64 mm inner diameter, 1.19 mm outer diameter), fixing at the 2.2 cm position from an end of the tubing using an adhesive (Loctite 401). Mice were anesthetized with 1.5−3.0% isoflurane, and the surgical areas were shaved and sterilized. A skin incision of ~5 mm was made along the dorsal midline, from the base of the skull to the interscapular region. Another skin incision of ~2 cm was made along the ventral midline, from the xiphoid cartilage to the left flank, and the subcutaneous tissues were dissected. These two incisions

were connected by inserting a sterilized catheter. The stomach was externalized and a small puncture was made using a scissor to insert the catheter, which was sutured into place (NB617, Ailee). The stomach was then placed back in the abdominal cavity, and the abdominal muscle and the skin incision was closed. Lastly, the catheter was secured at the interscapular site with sutures on the skin. For gastric balloon implantation, a latex balloon (7 mm long, 73-3478, Harvard Apparatus) was attached to the end of the intragastric catheter in the stomach using an adhesive (Loctite 401). Following the surgery, mice were provided with liquid food to avoid gastric filling by solid chow. For the duodenum or proximal colon, a smaller Silastic tubing (6 cm long, 0.28 mm inner diameter, 0.61 mm outer diameter was used. Balloon was similarly constructed and implanted in the duodenum or proximal colon.

Vagotomy

Mice were anesthetized with 1.5-3.0% isoflurane and placed in a stereotaxic apparatus while resting on a heating pad. A midline abdominal incision from the xiphoid process (~3 cm) was made along the linea alba to expose abdominal cavity, and the liver was gently retracted to the left side with cotton swabs. Then the stomach was moved out of the cavity and kept moisturized with

saline throughout the surgery. The esophagus was gently lifted and all identifiable vagus nerve fibers above the hepatic branches of the anterior vagus (both anterior and posterior vagal trunk) were excised with micro-scissors to achieve total subdiaphragmatic vagotomy. Vagotomy impairs gastric emptying; therefore, all experiments with vagotomized mice were completed within 6 hrs after the surgery, to avoid any confounding effects caused by the impaired gastrointestinal flow without additional pyloroplasty surgery. Furthermore, mice were provided with liquid food instead of chow food for a day prior to vagotomy, to minimize the amount of solids ingesta in the stomach during the experiment. To validate total subdiaphragmatic vagotomy, retrograde neural tracer Fluorogold (0.8 mg/0.4 ml in 0.9% saline; sc-358883; Santa Cruz) was intraperitoneally injected into the vagotomized mice or sham surgery control mice. 3 days after the injection, mice were euthanized and histologically processed to confirm the absence of Fluorogold in the dorsal motor complex.

Spinal transection

Spinal transection was performed at thoracic level 5, corresponding to the highest spinal cord segment where stomach-innervating splanchnic afferents are joined (*90*). Mice were anesthetized with

1.5–3.0% isoflurane and placed in a stereotaxic apparatus while resting on a heating pad. The surgical areas were shaved and sterilized. A skin incision was made along the dorsal midline at around the T4–T8 level. The incision was expanded with another small incision toward the right flank. Muscles and adipose tissues were cleared from the dorsal spinal lamina. T13 was identified by its dorsal spinous processes, and then T5 was identified by counting 8 ribs upwards. Lower spinal cord was gently lifted and thoracic level 5 spinal transection (T5x) was performed by scissors, surgical blades and micro-scissors. Finally, the skin incision was closed. To validate spinal transection, retrograde neural tracer retrobeads (Red RetroBeads; Lumafluor) was injected into the PB of mice that received thoracic level 5 spinal cord transection or sham surgery control mice. 3 days after the injection, mice were euthanized and histologically processed to confirm the absence of retrobeads in the spinal cord.

Fiber photometry

Fiber photometry recordings were performed as previously described (*91*). Briefly, two excitation lights from 470-nm and 405-nm LEDs (M470F3, M405F1; Thorlabs) were sinusoidally modulated by a real-time processor (RZ5P, Tucker Davis

Technologies) at 211 Hz and 531 Hz, respectively, and were collimated and delivered to the brain via a single low-autofluorescence fiberoptic patchcord and cannula (400 μm-core, 0.48 NA; Doric Lenses). The light intensity was maintained at less than 30 μW during all recordings. The fluorescence signal was then focused onto a femtowatt photoreceiver (2151; Newport) for detection, and the resulting signal was demodulated, amplified and collected at ~1 kHz by the RZ5P processor.

To examine the responses of PB^{Pdyn} neurons to water intake, empty bottle licking and to the intake of various test liquids except for liquid food, water-deprived mice were placed in a soundproof chamber with lickometers (Med Associates). After 5 min of baseline recording without access to liquid spouts, mice were provided with *ad libitum* access to the liquids for 20 min. Mice were habituated to the chamber and spouts for at least 2 days prior to the tests. Responses of PB^{Pdyn} neurons to liquid food were recorded in food-deprived mice.

To investigate the responses of PB^{Pdyn} neurons to hydrogel, water-deprived mice were provided with *ad libitum* access for 20 min to HydroGel (consisting of 98% water and 2% of hydrocolloids; ClearH_2O) after 5 min of baseline recording in a behavior chamber (23 x 43 x 22 cm). For chow food or high-fat chow, the same

experiments were conducted with food-deprived mice. Mice were acclimated to hydrogel or high-fat chow for at least 3 days before the tests. The consumption behavior was recorded using a video camera outside a transparent wall, and the video was analyzed frame-by-frame to determine the onset and offset of consumption events. The intake rate of fluids and solids was calculated by dividing total consumed weight by total bout duration.

For the tongue contact experiment, the dorsal surface of the anterior tongue was pressed for 2 s with the round-headed metal tip of the gavage needle (JD-S-124, 0.9 x 70 mm (20G), Jeung Do B&P), with the force of ~51.0 gf. This is in marked contrast with empty bottle licking (which did not evoke significant responses in PB^{Pdyn} neurons), which is known to exert only ~2 gf of force to the anterior-most part of the tongue for ~70 ms (*92–94*). For the esophageal insertion experiments, the gavage needle was slowly inserted into the esophagus over 3 s, touching and stretching the esophageal walls, and the needle was stably held for more than 30 s.

To investigate the responses of PB^{Pdyn} neurons to balloon inflation, water or saline was infused into the balloon via catheter using a syringe pump at the indicated rates. At the completion of the experiment, mice were immediately euthanized and the secure connection between the balloon and the catheter was confirmed.

Data were discarded if any leakage was detected. For gastric balloon experiments, the balloon was inflated to the volume of 200 μl, 350 μl, or 500 μl, which correspond to the less than half of the volume of the unstretched mouse stomach, the volume of the comfortably full mouse stomach, or the stretched volume (*95*). For duodenum and colon balloon experiments, the balloon was inflated to 50 μl, which approximately correspond to twice the volume of the intestinal segment occupied by 7 mm-long balloon (*96*) and to the volume of physiologically distended intestinal segment following the intake of a high-concentration glucose solution (*63*).

For oral gavage experiments, mice were gently restrained to immobilize the head by a skilled experimenter. A gavage needle attached to a syringe was brought inside the mouth, or inserted into the pharynx, esophagus or stomach via the mouth. A small water drop (10 μl), 200 μl of water or oil, or 500 μl of air was injected as indicated. Control experiments (mock) were performed by repeating the same procedure with an empty syringe.

For direct infusion of air into the stomach via intragastric catheter, a syringe pump (GenieTouch, Kent Scientific) was connected to the implanted catheter via a tubing. Air was injected at the indicated rates. For each recording experiment, three trials were averaged and treated as a single replicate.

To examine the responses of PB^{Pdyn} neurons under anesthesia, mice were anesthetized with 1.5–3.0% isoflurane. For the oral gavage experiment, 200 μl of water was infused directly into the stomach via oral gavage. For the stomach wall push experiment, a gavage needle was inserted into the digestive tract until the stomach and stably maintained. Then, a sphere–tipped blunt metal probe (~1 mm sphere diameter) was inserted into or withdrawn from the gavage needle, to gently distend the stomach wall while minimizing the mechanical disturbance along the digestive tract. All experiments except for these two were conducted in awake animals.

To examine the responses of PB^{Pdyn} neurons to solutions with different osmolality, taste and temperature, water–deprived mice were head–restrained using a custom–machined metal plate and habituated for >10 min a day for >3 days. The composition of each tastants was as follows: Artificial saliva, 4 mM sodium chloride, 10 mM potassium chloride, 6 mM potassium bicarbonate, 6 mM sodium bicarbonate, 0.5 mM calcium chloride, 0.5 mM magnesium chloride, 0.24 mM Dipotassium phosphate, 0.24 mM Monopotassium phosphate; sweet, 8 mM acesulfame potassium; sour, 10 mM citric acid; salty, 60 mM NaCl; umami, 50 mM monopotassium glutamate and 1 mM inosine monophosphate. Each solution was delivered to

the mouth with a 22 gauge metal tube using a pressure injection system operated by TTL pulses (GenieTouch, Kent Scientific). The tip of the tube was placed right above the tongue, such that liquid drops formed by the injection directly touched the tongue. For each trial, fluid was injected at a rate of 200 μl/min for 15 s to deliver a total amount of 50 μl. Dotted lines in Figures 3n–p indicate the time when the operation signal was sent to the syringe pump. The apparent lag in calcium response can largely be explained by the experimental delay of solution delivery to the mouth from the onset of syringe pump action.

For the open field test, mice were placed in an open field arena (50×50 cm^2) for 10 min for assessing locomotor activity and anxiety–related features. The center zone was defined as the 25×25 cm^2 square at the center of the arena. For the elevated plus maze test, mice were placed on an elevated plus maze, consisting of two open and two closed arms (30×5 cm^2) extending from a central platform elevated from the ground by 50 cm, for 10 min.

To investigate the responses of PB^{Pdyn} neurons to hypertonic saline injection, euhydrated mice were placed in a behavior chamber and calcium signals from PB^{Pdyn} neurons were recorded using fiber photometry for 15 min ('Pre'). Mice were then intraperitoneally injected with 150 μl of 3 M NaCl, and were recorded for 45 min

(‘Post’). Therefore, a single recording of 60 min was made for each mouse.

To observe the responses of the PB^{Pdyn} neurons to whisker touch, whiskers of gently handled mice were touched by a plastic rod. The side of the whiskers (left or right) was randomly chosen for each trial. A session contained 5 trials with ~30s inter-trial interval, each of which consisted of 5 whisker stimulations for 5 sec. The data collected from left and right whisker stimulations were pooled as no differences were detected.

To examine the responses of the PB^{Pdyn} neurons to sensory detection of peanut butter, mice were placed in a chamber ($18 \times 20 \times 36$ cm^3) with a metal grid floor. After a baseline recording for 5 min, an empty dish was inserted under the grid floor, and then was withdrawn. This was followed by another baseline recording for 5 min, and a small amount of peanut butter placed in another dish was inserted under the floor so that the mice could see and smell, but could not consume the peanut butter for 5 min.

To test if PB^{Pdyn} neurons respond to sensory cues paired with water delivery, head-fixed mice received 20 presentations of 10-s tone (3 kHz, 80 dB) that co-terminated with 5-s water delivery into the mouth (inter-trial interval: 60 s). Injected at a rate of 200 μl/min for 5 s, the resulting water drop was ~17 μl.

The entire session was repeated daily for 4 days. To maintain the mice in water-depleted condition for four consecutive days, mice were allowed for ad libitum access to water for 2 hrs daily following the experiment.

To examine the responses of PB^{Pdyn} neurons to water depletion and repletion, euhydrated mice were placed in a behavioral chamber and were recorded for >10 min on day 1 ('BA'). Mice were then returned to home cages and water-deprived for 24 hrs. On the next day, the dehydrated mice were placed in the behavioral chamber and calcium signals were recorded again for >10 min on day 2 ('WD'). After *ad libitum* water access for the next 24 hrs, the euhydrated mice were placed in the behavioral chamber and were recorded again for >10 min ('WR'). Fiber photometry settings were identical for all recording sessions, and all the raw data were normalized by the median fluorescence of Day 1 baseline recordings.

To examine the responses of PB^{Pdyn} neurons to systemic cholecystokinin (CCK) injection, CCK dissolved in 0.9 % saline (100 μM, 200 μl/mouse) was injected intraperitoneally to the mice during photometry recordings.

All fiber photometry data were analyzed with custom-written Matlab (Mathworks) code in combination with the behavior

data collected with Med-PC (Med Associates) or Ethovision (Noldus). The photometry signal was analyzed as described previously (*91*). Data were low-pass filtered at 2 kHz and downsampled to 100 Hz. A linear function was used to scale the 405-nm channel signal to the 470-nm channel signal to obtain the fitted 405-nm signal. The resulting ΔF/F was calculated as (raw 470 nm signal - fitted 405 nm signal) / (fitted 405 nm signal) unless otherwise noted. Depending on the experiments, peri-event time plots were created using either the TTL timestamps generated by lickometeres, timestamps marked by manual frame-by-frame video analysis, or timestamps manually marked when infusing fluids directly to the digestive tract. Animal's location, time spent in each chamber, and velocity were scored using Ethovision.

Normalized ΔF/F was calculated by subtracting the average baseline ΔF/F from individual raw values and by dividing the difference by the baseline standard deviation. For peri-event time plots, the baseline was defined as the 3 s preceding event onset (e.g. licking bout, solid contact, passive water delivery to the mouth, tone onset, direct liquid delivery to the digestive tract, etc.) The number of licks were counted in 1-s bins to calculate the lick rate shown in peri-event plots.

The bulk responses of PB^{Pdyn} neurons from each mouse to

the events were characterized using area under the receiver-operating characteristic (auROC) curve analysis. ROC curves were calculated by comparing the distribution of ⊿F/F across trials in 100-ms bins, to the distribution of baseline ⊿F/F (3 s before the onset of the events).

In the bar graphs comparing the responses of PB^{Pdyn} neurons to direct fluid injection into the digestive tract via oral gavage or intragastric catheter, ⊿F/F was averaged over a 5-second time window from the infusion onset, unless otherwise noted. A bout for the licking of liquids was defined as any set more than 5 licks, in which no inter-lick interval was greater than 3 s. A bout for solid intake was defined as any continuous action of active consumption. The duration of most bouts for solid intakes was longer than 5 s.

To examine the correlation between PB^{Pdyn} neuronal activity and velocity of mice, datapoints defined by pairing ⊿F/F with velocity were pooled in 2 cm/s bins for averaging calcium responses, and fitted to a linear curve.

I note that individual variability in the response amplitudes of PB^{Pdyn} neurons within the same experiment is attributable to the exact targeting of the tip of the fiberoptic cannula, since I observed the variability in the response amplitudes even from the same cohort of the animals, which underwent surgery and behavioral

experiments on the same dates by the same experimenters using the same protocols. Despite the efforts to collect the data from mice with correct targeting (Figure 3a), relative positions of the fiberoptic cannula tip to the PBdl could still widely vary within the accepted range, which would cause the variability in response amplitudes (as shown in Figure 7, individual PB^{Pdyn} neurons exhibited varying degrees of response strengths). For example, the intensity of a 532-nm light in the brain tissue could be attenuated to less than 20% of the original intensity after propagating 250 μm (simulated using Monte Carlo method (*97*)), which can directly affect the amplitude of the neural responses to behavioral events.

Two-photon calcium imaging

A two-photon microscope (Olympus FVMPE-RS) equipped with a fast resonant scanner, a high-sensitivity gallium arsenide phosphide (GaAsP) photomultiplier tube (PMT) detector, 20x air objective lens with 8.3 mm working distance (Olympus LCPLN20XIR, 0.45 NA), a tunable Mai-Tai laser (Spectra-Physics, Mai-Tai DeepSee), and quadralign 4 axis laser alignment system was used. For all imaging sessions, images were obtained at 5 Hz, using the fast resonant scanner at 30 Hz and a frame averaging of 6. Software were set as the following: laser power, 350~850mW;

PMT voltage, 650; gain, 1; offset, 0; scan size, 512×512; zoom, 1. For comparing images acquired from different experiments, the same field of view was acquired under the same imaging parameters. For each imaging session, two-photon scanning was triggered by TTL pulses for each trial 30 s before the application of stimuli, and was continuously recorded for the entire session.

Mice were habituated to head fixation and to liquid food, and water-deprived for 1-2 days before imaging under the two-photon microscope. For the intake experiments, 33 μl of water or liquid food was delivered in the mouth at a rate of 200 μl/min for 10 s via a 22-guage blunt needle using a pressure injection system operated by TTL pulses (GenieTouch, Kent Scientific). Each session consisted of 5 trials. The experimenter confirmed if mice consume the fluid well before and after each session. For the gastric balloon experiments, PBS was injected into, or withdrawn from, the balloon via Silastic tubing at different rates (1.2, 2.1, and 3.5 ml/min for 200, 350, and 500 μl inflation, respectively) for 10 s using the same pressure injection system. Each session consisted of 3 trials. Balloons were remained inflated for 30 s after inflation, and then deflated over the next 10 s. For the oral liquid drop delivery experiments, small drops (less than 10 μl) of water or liquid food were delivered to the mouth as described above, at 600

μl/min for 1 s. The data obtained from the delivery of water and liquid food drops were pooled, since the responses of PB^{Pdyn} neurons were indistinguishable. Each session was consisted of 7 trials. Inter-trial intervals were pseudorandomized, with 30 s average intervals for all experiments.

Acquired data were processed by a non-rigid motion correction algorithm (NoRMCorre), and the region of interest (ROIs) for each neuron were defined manually using the standard deviation projection of the movie created by ImageJ. Based on the projection images, each neuron was manually registered across different recording sessions. The average fluorescence signals in the ROI of each neurons were extracted, smoothed with a five-frame running averaging, and analyzed with a custom-written Matlab code. Normalized ΔF/F was calculated as described above, except that the baseline was defined as the 5 s before the event onset (i.e. passive fluid delivery to the mouth and intragastric balloon inflation). The responses of individual PB^{Pdyn} neurons to the events were characterized using area under the receiver-operating characteristic (auROC) curve analysis. auROC curves was calculated by comparing the distribution of trial normalized ΔF/F (0-20 s after the onset of liquid delivery and 0-50 s after the onset of intragastric balloon inflation) to the distribution of baseline

⊿F/F (0–5 s before the onset of the events). Neurons were classified as responsive if trial normalized ⊿F/F exceeded 2 s.d. Maximum values for trial normalized ⊿F/F were used for correlation analysis. A representative water intake session was chosen, and the maximum value for trial normalized ⊿F/F of each neuron in the session was divided by the maximum value of the highest responded neuron to normalize the activities of all neurons in Fig. 2b.

Optogenetic and chemogenetic manipulations

To stimulate ChR2-expressing neurons or terminals, 5–15 mW of blue light (159–477 mW/mm^2 at the tip of the fiberoptic) was generated by 473 nm laser (MBL-III-473; OEM Laser Systems), and delivered to mice through two bilateral fiberoptic patch cords (0.22 NA, 200 μm diameter; Newdoon). Blue laser output was controlled using a pulse generator (Pulse Pal; Sanworks) to deliver 10-ms light pulse trains at 20 Hz. For chemogenetic experiments, CNO (BML-NS105; Enzo), prepared in 0.9% sterile saline, was injected at 0.3–1 or 10 mg/kg of body weight for hM3Dq or hM4Di experiments, respectively, 45 min before initiation of the behavior session.

For food intake assays, food-deprived mice were placed in a

behavior chamber (23×43×22 cm^3) without access to chow food for acclimatization for 10–30 min, then were provided *ad libitum* access to chow food for 30 min or 4 hrs. Food intake was measured by changes in the weight of the food pellet at the indicated timepoints.

For water intake assays, mice were placed in a soundproof chamber with lickometers (Med Associates). After 5 min of acclimatization, mice were provided with *ad libitum* access to water for the duration of each session. For 24–hr chemogenetic stimulation experiments, mice were provided with *ad libitum* access to a low–concentration CNO solution (0.0025% (w/v)). Mice were habituated to the chamber and spouts for at least 2 days prior to the tests. For optogenetic stimulation experiments, mice were given light pulse trains throughout the 25–min session including acclimatization. For pre–stimulation experiments, mice received laser stimulation for 30 min in a cage and transferred to the chamber with lickometers to begin water intake assays.

For two–bottle tests for assaying water and saline intakes, mice were placed in a soundproof chamber with lickometers (Med Associates). After 5 min of acclimatization, mice were provided with *ad libitum* access to water and 2% NaCl for 20 min. The liquid bottles were counterbalanced across the left and right sides of the

chambers. Mice were habituated to the chamber, spout and liquids for at least 2 days before the tests. For optogenetic stimulation experiments, mice were given light pulse trains throughout the session including acclimatization. For lick-paired stimulation experiments, 10-ms light pulses were delivered at 20 Hz for 0.1 s upon individual licks. Salt-depleted condition was induced by subjecting mice to intraperitoneal injections of furosemide (a loop diuretic, 10 mg/25 g body weight) and housing them with salt-depleted food and water for 24 hrs. Water- or food-deprived conditions were induced as described above.

For prandial thirst experiments, food-deprived mice were provided with *ad libitum* access to the standard chow food in a behavioral chamber without access to water. After 30 min of free-access feeding, mice performed two-bottle tests without acclimatization. Laser stimulation was given throughout the session of each two-bottle test.

For real-time place preference test, mice were placed in a box (50 x 25 x 25 cm^3) consisting of two indistinguishable chambers for 15 min. Only one chamber was paired with light stimulation. The choice of paired chamber was counterbalanced across mice. Animals were placed in the unstimulated chamber at the start of the session and received light stimulation initiated upon

every entry into the paired chamber.

For social interaction test, a 5-week-old juvenile stranger mouse was introduced into the home cage of a test mouse. After 1-min baseline interaction, a session began with a 'laser on' epoch or a 'laser off' epoch for 1 min. The beginning epochs were counterbalanced, and the epochs were alternated for five times, such that each session consisted of 10 epochs, with interleaved 5 laser on and off epochs. Social interaction time was measured as the time in which the test mouse actively investigated the intruder. No attack or mounting behavior was observed in our experiments.

Histology and confocal microscopy

Mice were deeply anesthetized and were transcardially perfused with ice-cold 4% paraformaldehyde (PFA) in PBS (pH 7.4). Brains or spinal cords were harvested, fixed overnight in 4% PFA solution, and equilibrated in 30% sucrose in PBS. For harvesting spinal segments, the rib cage, diaphragm, organs were removed. T5-L1 segment was identified by counting ribs, then muscle, fat, C1-T4 and L2-S4 spinal segments were isolated. The dorsal surface of the spinal segment was carefully divided in half down the midline. After the tissues reached equilibrium in 30% sucrose PBS solution, 50 μm-thick coronal slices were cut on a freezing microtome. For

spinal segment sections, samples were embedded in agarose gel and 100 μm-thick coronal sections were collected. Slices were stored in a cryoprotectant solution (a 5:6:9 mixture of glycerol, ethylene glycol and PBS) at 4 °C until further processed. Free-floating sections were then washed in PBS, incubated for >25 min in 1:10,000-50,000 DAPI solution, washed again in PBS and mounted on microscope slides with PVA-DABCO. Confocal images were obtained on a Zeiss LSM 880 laser scanning microscope using 10x/0.45 NA, 20x/1.0 NA or 40x/1.2 NA objective lens. Images were analyzed using IMARIS (Bitplane). For rabies tracing experiments, 300 μm-thick coronal slices were collected, washed in PBS and incubated in 1:5,000 DAPI solution for 24 hrs. Samples were then incubated in Sca*l*eCUBIC-2 solution (A mixture of 25 wt% urea, 50 wt% sucrose, 10 wt% triethanolamine and 15 wt% distilled water) for 24 hrs for enhanced transparency (*98*), followed by mounting with the same solution and imaging.

Abbreviations. 10N, dorsal motor nucleus of the vagus nerve; 12N, hypoglossal nucleus; 3V, third ventricle; 5Tr, trigeminal transition zone; aca, anterior commissure; ad, anterodorsal part of BNST; AMB, nucleus ambiguus; AP, area postrema; aq, aqueduct; arb, arbor vitae; Arc, arcuate nucleus; BLA, basolateral amygdala; BNST, bed nucleus of the stria terminalis; Cb,

Cerebellum; CeA, central amygdala; cl, central lateral PB; CO, cochlear nucleus; CU, cuneate nucleus; DB, diagonal band; dl, dorsal lateral PB; DMX, dorsal motor nucleus of the vagus nerve; DR, dorsal raphe nucleus; el, external lateral PB; f, fornix; ic, internal capsule; icp, inferior cerebellar peduncle; IO, inferior olivary complex; LC, locus coeruleus; LH, lateral hypothalamus; lPAG, lateral PAG; LPO, lateral preoptic area; m, medial PB; MCLH, magnocellular nucleus of LH; Me5, mesencephalic trigeminal nucleus; MeA, medial amygdala; mlf, medial longitudinal fascicle; MnPO, median preoptic nucleus; MPA, median preoptic area; NR, nucleus of roller; ns, nigrostriatal tract; NTSim, intermediate NTS; NTSl, lateral NTS; NTSm, medial NTS; NTSpl, posterior-lateral NTS; NTSpm, posterior-medial NTS; opt, optic tract; ov, oval nucleus of BNST; OVLT, vascular organ of lamina terminalis; PAG, periaqueductal gray; PAS, parasolitary nucleus; PB, parabrachial nucleus; PBdl, dorsal lateral PB; PBm, medial PB; PCG, pontine central gray; PLH, posterior LH; Pr5, principal sensory trigeminal nucleus; PRP, nucleus prepositus; PVH, paraventricular hypothalamus; PVT, paraventricular thalamus; RM, nucleus raphe magnus; RM, raphe magnus nucleus; RN, reticular nucleus; RO, nucleus raphe obscurus; RPA, nucleus raphe pallidus; scp, superior cerebellar peduncle; sctv, ventral spinocerebellar track; sctv,

ventral spinocerebellar tract; SFO, subfornical organ; SI, substantia innominana; sl, superior lateral PB; SON, supraoptic nucleus; sp5, spinal trigeminal tract; Sp5C, spinal trigeminal nucleus, caudal part; Sp5I, spinal trigeminal nucleus, interpolar part; Sp5O, spinal trigeminal nucleus, oral part; TN, trigeminal nucleus; VII, facial motor nucleus; vl, ventral lateral PB; vlPAG, ventrolateral PAG; VLPO, ventrolateral preoptic nucleus; VN, vestibular nucleus; VP, ventral pallidum.

Fos immunohistochemistry

Free-floating 50-μm sections containing the PB (from -5.0 mm to -5.5 mm AP) obtained as described above were washed in PBS and then incubated for 30 min in 0.1% Triton X-100 and 3% normal donkey serum (NDS; Jackson Immunoresearch) to reduce nonspecific binding. Primary antibody incubation was performed overnight or 1-2 days at 4 °C in 3% NDS/PBS (rabbit anti-Fos, 1:300-500, 2250S; Cell Signaling Technology; rabbit anti-2A 1:300-500, ABS31; Merck Millipore), followed by washing and incubation with secondary antibodies (Alexa 488- or 647-conjugated donkey anti-rabbit IgG, 1:500, Thermo Fisher Scientific) for 3 hrs at room temperature. These sections were washed and stained with DAPI, and mounted as described above.

For the water-depletion and repletion experiments, two groups of mice expressing fluorophores in PB^{Pdyn} neurons were each single-housed for more than 3 days, water-deprived for 46 hrs, and water was returned to only one group. After 2 hrs, all mice were perfused and brain sections were prepared.

Fluorescence In situ hybridization

Mice were deeply anesthetized and were transcardially perfused with ice-cold PBS (pH 7.4). Brains were harvested and fresh-frozen on aluminum foil filled with optimal cutting temperature compound (Tissue-Tek) on dry ice. Brains were then stored at -80° C until further processing. Prior to sectioning, brains were equilibrated to -21° C in a cryostat for 60 min. Brains were coronally sectioned at 20 μm and thaw-mounted onto Superfrost Plus slides (25x75x1 mm, Fisherbrand). Brain sections were fixed in 4% PFA for 15 min and then washed in 50%, 70%, 100%, and 100% ethanol for 5 min each. Slide-mounted samples were air-dried for 5 min and treated with protease for 30 min. Slides were washed twice in PBS. Probes were previously heated in a 40° C water bath for 10 min and applied to the slides, which were placed in a 40 ° C humidified oven for 2 h. Slides were washed twice in RNAscope wash buffer for 2 min each, and then underwent the

amplifier hybridization steps according to the user manual (#320293, Advanced Cell Diagnostics). Amplifiers were previously equilibrated at RT. After the final hybridization step, samples were counterstained with DAPI (Advanced Cell Diagnostics) for 30 sec and coverslips were immediately placed over the tissue section using ProLong Gold Antifade mounting medium (Thermo-Fisher) or Vectashield mounting media (Vector Labs). I used probes for *Slc32a1* (cat#319191), *Slc17a6* (cat#319171), *Pdyn* (cat#318771), *Fos* (cat#316921), *Oxtr* (cat#412171), and *Calca* (cat#417961).

To validate PB^{Pdyn}-PVH projection stimulation, mice used for the optogenetic stimulation of PB^{Pdyn}-PVH projections were single housed for a day. Food and water were removed 30 min before the experiment to prevent confounding effects. Mice were photostimulated for 30 min and immediately sacrificed for the FISH assay for Fos expression.

Statistical analysis

Statistical analyses and linear regressions were performed using Matlab (Mathworks) or Prism (GraphPad). I used two-tailed Wilcoxon rank-sum test, Kruskal-Wallis one-way ANOVA, one-way ANOVA, unbalanced two-way ANOVA with subsequent post-

hoc correction (Fischer’ s least significance difference), two-way repeated measures ANOVA with subsequent Bonferroni post-tests, or Pearson correlation depending on the experimental paradigm. *P<0.05, **P<0.01, ***P<0.001, ****P<0.0001. Details of the tests and statistical information are shown in Table 1. No statistics to determine sample size, blinding or randomization methods were used. Viral expression and implant placement was verified by histology before mice were included in the analysis.

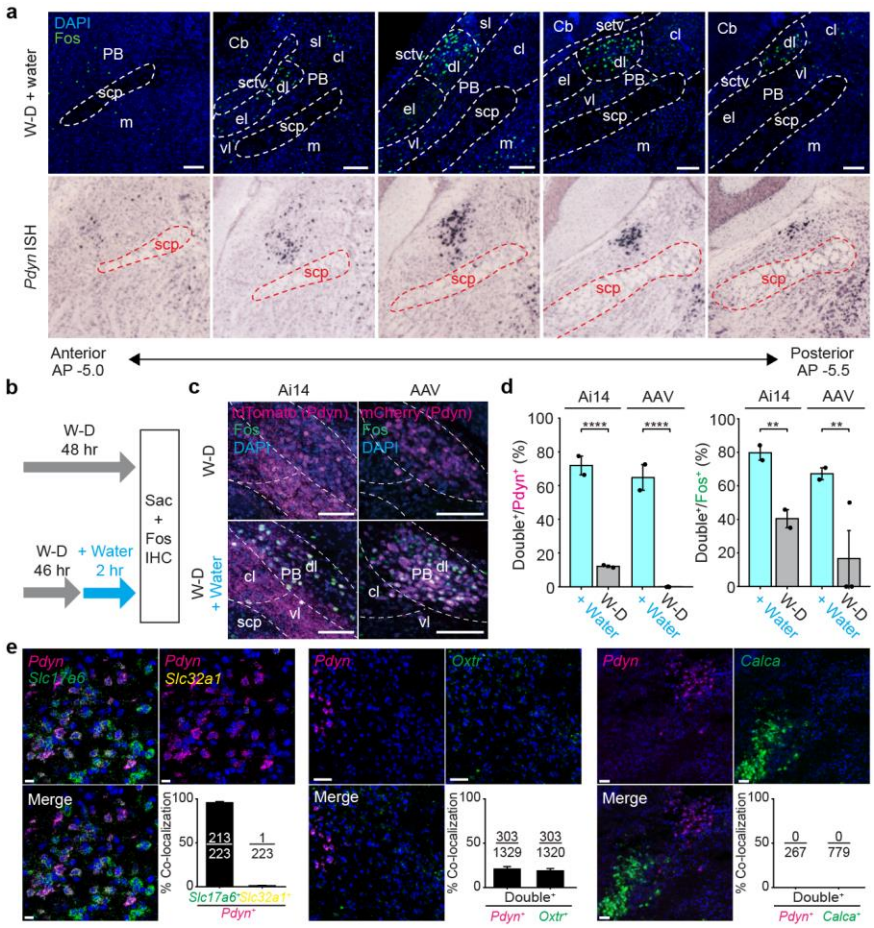

Figure 1. Fos expression in the PB after water intake and overlap of *Pdyn* with other neuronal markers. **a**, Fos immunofluorescence images (top) and the expression pattern of *Pdyn* from Allen Brain Atlas (bottom) along the antero-posterior axis of the PB. Brain slices were obtained after *ad libitum* water access following a 46-hr water restriction. Note the high concentration of Fos-expressing cells in the PBdl, where the expression of *Pdyn* is enriched. **b-d**, Water-deprived $Pdyn^{Cre/+}$::Ai14 mice or $Pdyn^{Cre/+}$ mice injected with Cre-inducible AAV carrying mCherry were given water access ('W-D + Water') or not ('W-D') before the Fos analysis (**b**). Representative confocal images (**c**) and quantification of the overlap between immunolabeled Fos^{+} and genetically labeled $Pdyn^{+}$ neurons in the PBdl (**d**) Note the smaller number of Fos^{+} neurons in the control mice (n = 146 and 7 neurons for experiments using Ai14 and AAV, respectively) than in the experimental group (n = 492 and 1,002 neurons for experiments using Ai14 and AAV, respectively). **e**, Representative images and quantification of multicolor fluorescence *in situ* hybridization experiments. $Pdyn^{+}$ neurons are mostly glutamatergic ($Slc17a6^{+}$) (>99%) (left), weakly overlapping with $Oxtr^{+}$ neurons (~23%) (middle), and non-

overlapping with *Calca*$^{+}$ neurons (0%) (right). Scale bars, 100 μm for (**a**), 10 μm for (**e**), 50 μm for (**g**) and (**i**). Data presented as mean ± s.e.m. Statistics in Table 1. Abbreviations in the Methods.
This figure is reprinted from (*99*).

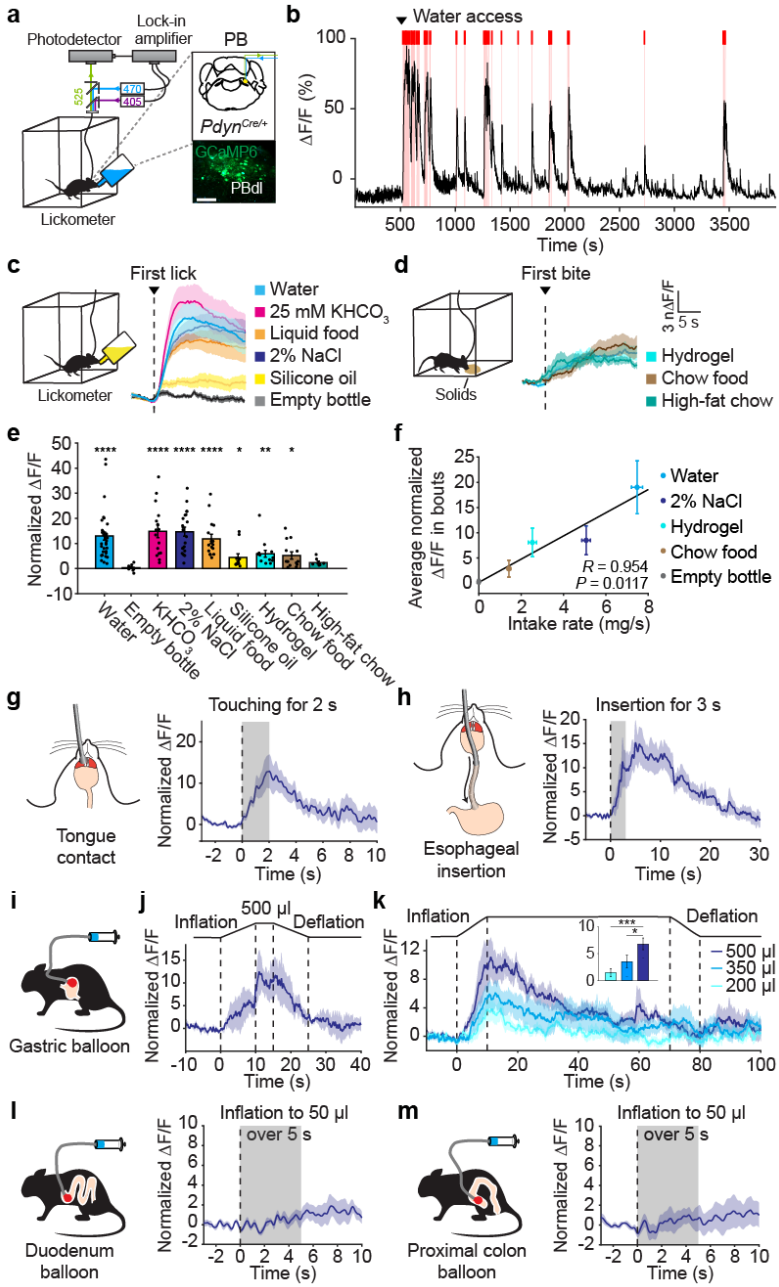

Figure 2. Prodynorphin-expressing PB neurons monitor ingestion using mechanosensory signals from the upper digestive tract. **a**, Fiber photometry recording from PB^{Pdyn} neurons. **b**, Example recording of PB^{Pdyn} neurons during water intake. Red lines, licks; red shaded boxes, bouts. **c**,**d**, Responses of PB^{Pdyn} neurons to the intake of various test liquids (**c**) and solids (**d**). **e**, Average calcium responses during intake bouts. Comparisons against empty bottle are indicated. **f**, Correlation between intake rate and PB^{Pdyn} neuron activity. **g**,**h**, PB^{Pdyn} neurons were robustly activated by touching the tongue (**g**) or inserting gavage needle through the esophagus

(**h**). **i**–**k**, Gastric balloon inflation for mechanical distension of the stomach (**i**). PB^{Pdyn} neurons showed increase and decrease in activity during balloon inflation and deflation, respectively, without any prolonged responses (**j**). The response amplitude scaled with the inflated volume, and adaptation-like changes were revealed by prolonged maintenance of balloon inflation (**k**). Inset, average calcium responses in the first 30 s of inflation. **l**,**m**, PB^{Pdyn} neurons did not significantly respond to the balloon-mediated distension of either the duodenum (**l**) or proximal colon (**m**). Scale bars, 100 μm. Data are mean ± s.e.m. **P*<0.05, ***P*<0.01, *****P*<0.0001. Statistics in Table 1.
This figure is reprinted from (*99*).

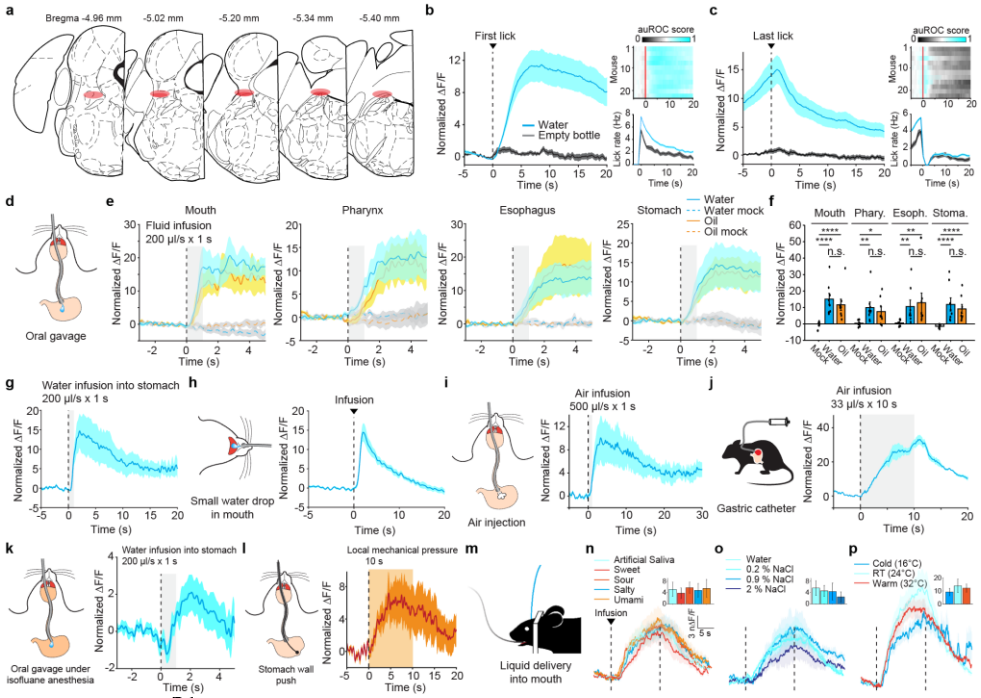

Figure 3. PB^{Pdyn} neurons monitor ingestion using mechanosensory signals arising from the upper digestive tract. **a**, Fiberoptic cannula targeting the PB for fiber photometry were placed inside the red areas. **b**, **c**, Average calcium transients around the first (**b**) or the last lick (**c**) in every bout, showing time-locked responses of PB^{Pdyn} neurons to licking water (blue traces), but no response to empty bottle licking (black). Inset top, average responses of all mice shown as auROC heatmap. Inset bottom, peri-event plot of lick rate. **d**-**g**, Infusion of either water or oil into the mouth, pharynx, esophagus, or stomach via oral gavage (**d**) induced strong activity in PB^{Pdyn} neurons (**e**). Average calcium responses in the first 5 seconds of infusion (**f**). The rate-controlled infusion of either water or silicone oil evoked comparable responses in PB^{Pdyn} neurons, contrary to the uncontrolled voluntary consumption of water and oil (Fig. 1e), in line with the intake rate-dependency of the responses (Fig. 1f). Intragastric water infusion with longer intervals reveals the return of the activity to the baseline (**g**). **h**, PB^{Pdyn} neurons robustly responded to oral delivery of a small water drop (10 μl), which would not immediately flow beyond the mouth. **i**,**j**, Intragastric air infusion via either oral gavage (**i**) or catheter (**j**) strongly activated PB^{Pdyn} neurons. **k**, Intragastric water infusion via oral gavage in anesthetized mice also activated PB^{Pdyn} neurons. **l**, Local distension of the stomach wall using a blunt probe in anesthetized mice robustly activated PB^{Pdyn} neurons. **m**-**p**, Various test solutions were delivered to the mouth of head-fixed mice (**m**). PB^{Pdyn} neurons exhibited comparable responses to the intake of solutions with different taste (**n**),

osmolality (**o**) and temperature (**p**). Insets show average calcium responses in the first 15 seconds of injection. Dotted lines indicate the onset and offset of infusion. Data are mean ± s.e.m. **P*<0.05; ***P*<0.01, *****P*<0.0001. n.s., not significant. Statistics in Table 1.
This figure is reprinted from (*99*).

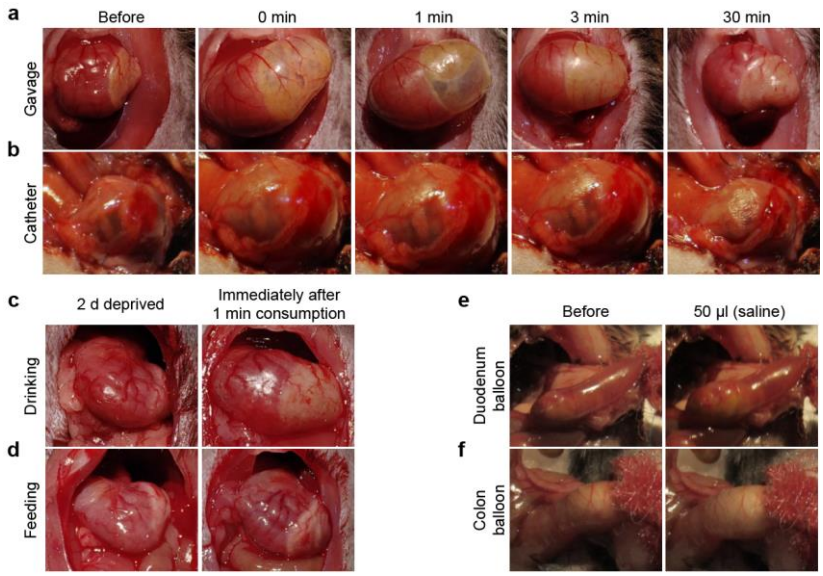

Figure 4. Intragastric air infusion induces stomach distension. a, b, Representative photographs of the stomach of an anesthetized mouse before and after intragastric air infusion via oral gavage (**a**) or gastric catheter (**b**). For oral gavage, 1 ml of air was injected over 1 s, and then after 3 s, the gavage needle was slowly withdrawn. Mice were rapidly euthanized at the indicated timepoints, the stomach was exposed, and the pictures were taken. For the injection via gastric catheter, 1 ml of air was injected over 10 s. Note that the stomach remained visibly distended at least for 3 min in both cases. **c**, **d**, PB^{Pdyn} neurons respond more strongly to drinking than feeding, as the intake rate is higher for fluids than solids. While solids are generally considered to distend the stomach more potently than liquids for the slower emptying into the intestine, gastric emptying occurs on the order of tens of minutes, whereas the activity of PB^{Pdyn} neurons evoked by ingestion is on the order of seconds. In accordance with this view, I found that *ad libitum* intake of water in water-deprived animals for 1 min led to larger distension of the stomach (**c**) than the intake of chow food in food-deprived animals for the same duration (**d**). **e**, **f**, Representative photographs of the balloon-implanted duodenum (**e**) and proximal colon (**f**) before and after the injection of 50 μl saline into the balloon, showing noticeable distension (see Methods).
This figure is reprinted from (*99*).

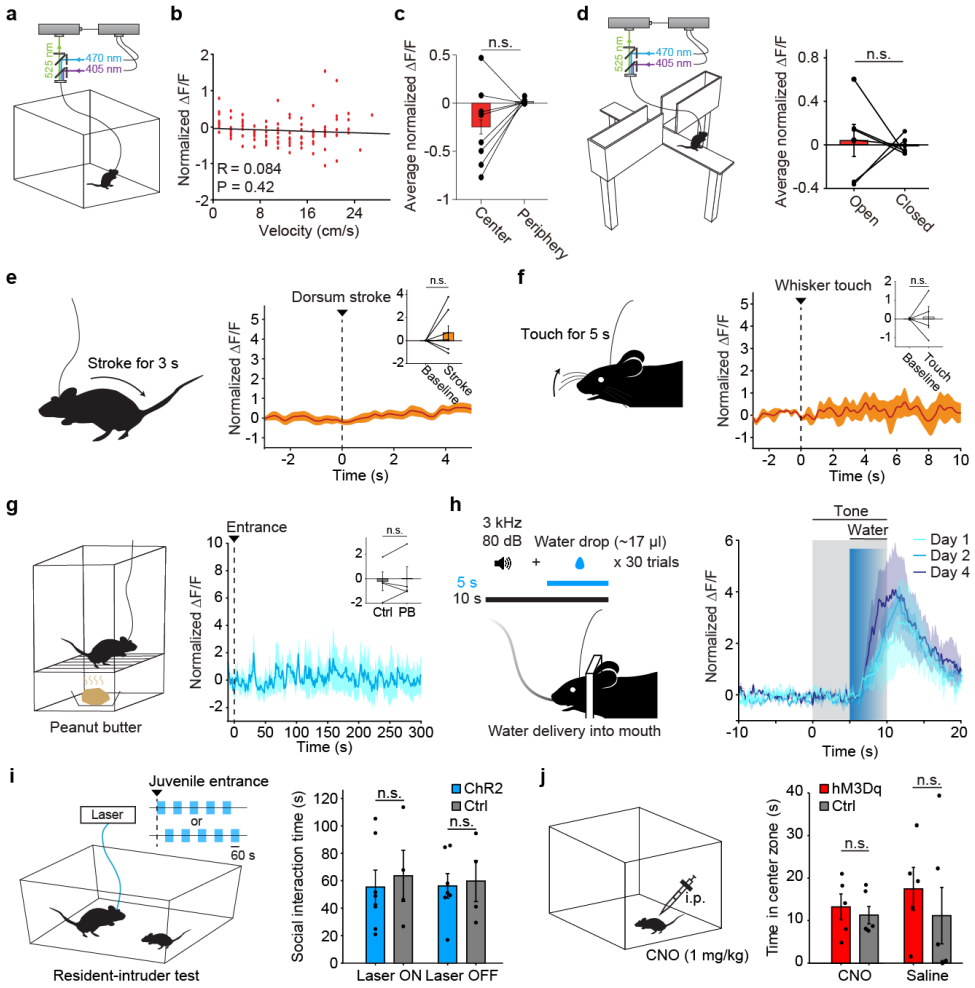

Figure 5. Control recording and manipulation experiments for PB^{Pdyn}. **a**–**c**, Activity of PB^{Pdyn} neurons was recorded during the open field test (**a**). Activities of PB^{Pdyn} neurons did not correlate with velocity (**b**), and were not significantly different regardless of whether mice were in the center zone or in the periphery (**c**). **d**, Mice were placed on an elevated plus maze, in which open arms represent an anxiogenic environment. Activities of PB^{Pdyn} neurons were not significantly different regardless of whether mice were in the open or closed arms. **e**, PB^{Pdyn} neurons were not activated by gentle stroking of the dorsum of mice. Peri–event plot of average calcium transients and bar plot of average normalized ⊿F/F before and during stroking are shown. **f**, PB^{Pdyn} neurons did not respond to touching the whisker. **g**, PB^{Pdyn} neurons were not responsive to sensory detection of peanut butter. **h**, Head–fixed, water–deprived mice received 20 tones that co–terminated with water delivery for 4 days. Average responses of PB^{Pdyn} neurons across training days, showing consistent and robust

responses to water delivery (dark blue shaded box), but no responses to the auditory cue (gray shaded box). **i**, Optogenetic stimulation of PB^{Pdyn} neurons did not affect social interaction time with a juvenile stranger mouse. **j**, Chemogenetic stimulation of PB^{Pdyn} neurons did not alter time spent in the center zone, indicating no change in anxiety-like behaviors. Data presented as mean ± s.e.m. n.s., not significant. Statistics in Table 1. This figure is reprinted from (*99*).

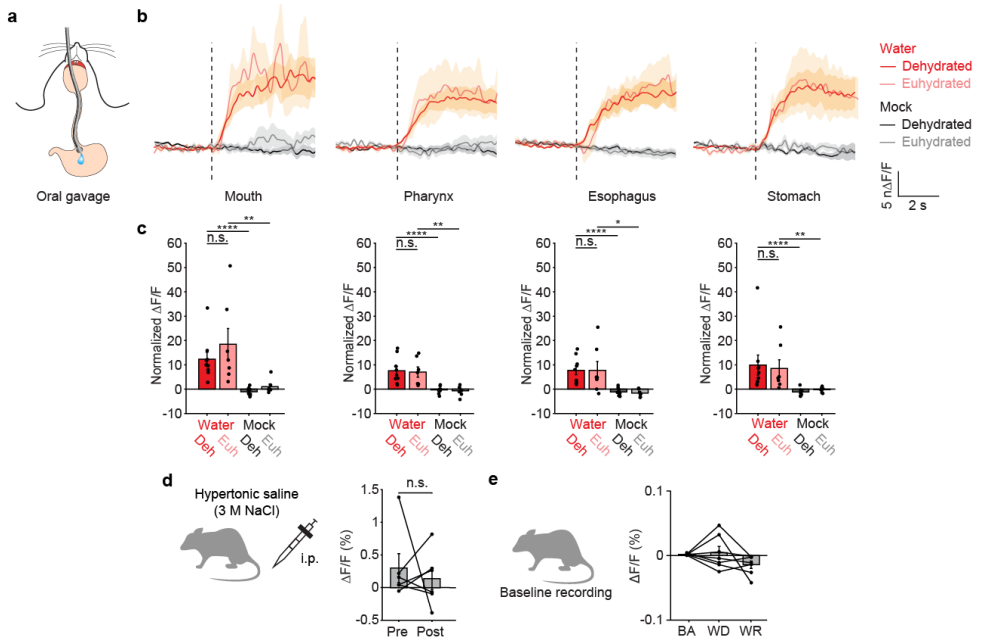

Figure 6. Activity of PB^{Pdyn} neurons is not modulated by the thirst state. a, Water was directly injected into the mouth, pharynx, esophagus, or stomach of dehydrated or euhydrated mice via oral gavage. **b**,**c**, Peri-event plot of average calcium transients (**b**) and average normalized calcium responses in the first 5 seconds of injection (**c**). Regardless of whether animals were dehydrated or euhydrated, PB^{Pdyn} neurons were robustly activated by water infused into any part of the upper digestive tract. **d**,**e**, Average calcium activity of PB^{Pdyn} neurons were not different b efore and after the thirst-inducing hypertonic saline injection (**d**) or 24-hr water deprivation (**e**). Data presented as mean ± s.e.m. *P<0.05; **P<0.01; ****P<0.0001. n.s., not significant. Statistics in Table 1.
This figure is reprinted from (*99*).

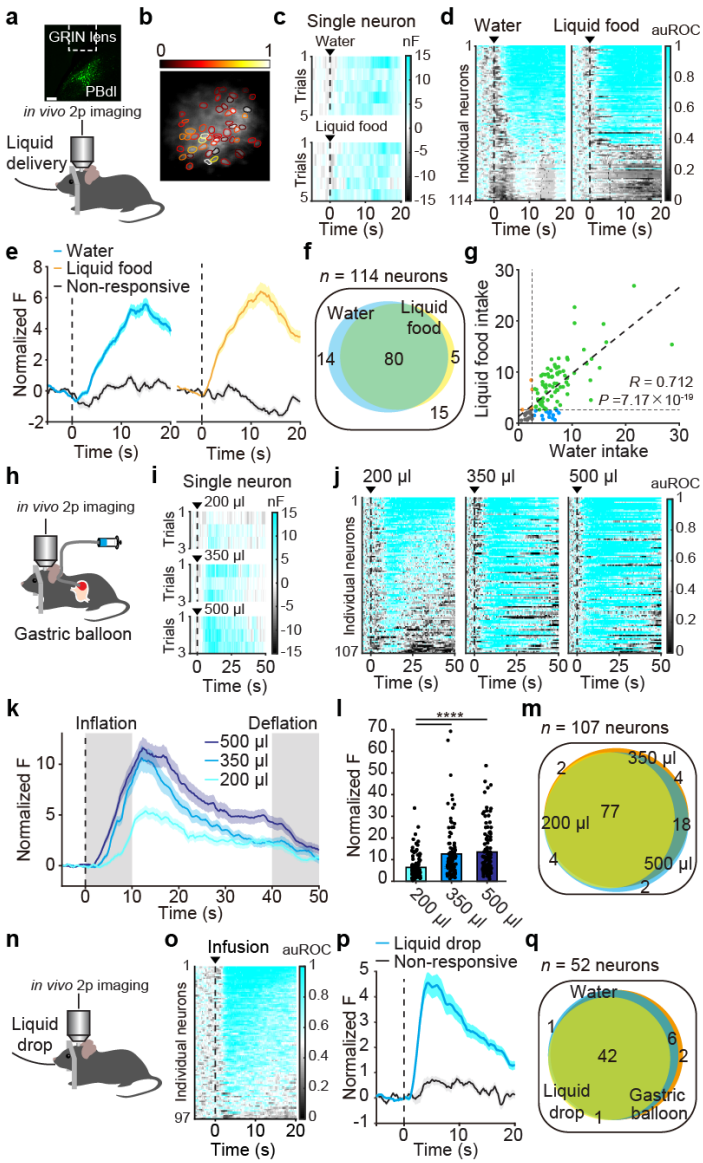

Figure 7. Representation of integrated mechanosensory signals by individual PB^{Pdyn} neurons. **a**, Two-photon calcium imaging of PB^{Pdyn} neurons during oral delivery of water or liquid food. **b**, Representative two-photon image of PB^{Pdyn} neurons. Colors indicate the normalized calcium responses in the first 20 s of water infusion. **c**, Responses of an example neuron. **d**, Responses of all neurons averaged across all trials. **e**, Average calcium traces from significantly activated or non-responsive neurons. **f**, Distribution and overlap of responsive neurons. **g**, Correlation between the response amplitudes for the intake of water or liquid food. **h**, Two-photon imaging of PB^{Pdyn} neurons during intragastric balloon inflation (10-s inflation, 30-s maintenance, 10-s deflation). **i**, Responses of an example neuron. **j**, Trial-averaged responses of all neurons. **k**, Average

calcium traces from significantly activated PB^{Pdyn} neurons. **l**, Average activity in the first 30 s of intragastric balloon inflation. **m**, Distribution and overlap of responsive neurons. **n**, Two-photon imaging of PB^{Pdyn} neurons during oral delivery of small liquid drop (water and liquid food pooled). **o**, Trial-averaged responses of all neurons. **p**, Average calcium traces from significantly activated or non-responsive neurons. **q**, Distribution and overlap of responsive neurons. Dotted lines indicate the stimulus onset. Scale bars, 150 μm. Data are mean ± s.e.m. *P<0.05, ****P<0.0001. Statistics in Table 1.
This figure is reprinted from (*99*).

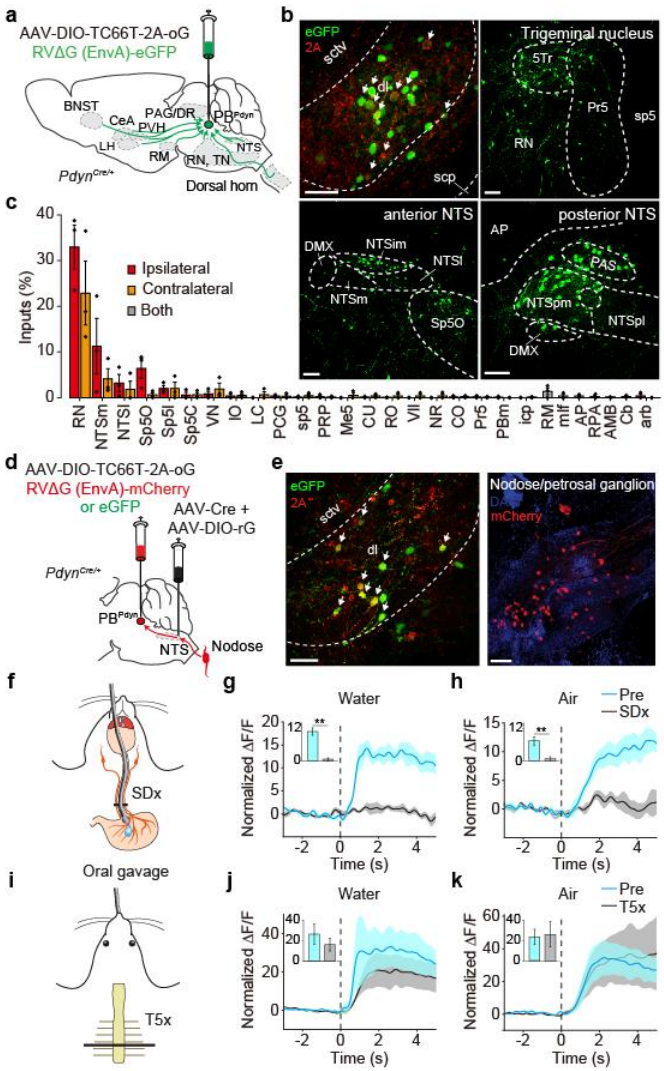

Figure 8. Vagus nerve conveys gastric distension signals to PB^{Pdyn} neurons. **a**, Engineered rabies virus–mediated identification of monosynaptic inputs to PB^{Pdyn} neurons. **b**, Confocal images showing the injection site and labeled neurons in select upstream regions in the hindbrain. **c**, Quantification of monosynaptic inputs in the hindbrain, shown as the percent of labeled neurons from a given brain region relative to the total labeled neurons throughout the hindbrain. **d.** Engineered rabies virus–mediated identification of monosynaptic inputs to PB^{Pdyn}–projecting NTS neurons. **e**. Representative images showing starter cells (left, arrows) and labeled neurons in the nodose/petrosal ganglia projecting to the PB^{Pdyn}–projecting NTS neurons (right). **f**–**h**, Total subdiaphragmatic vagotomy (SDx) (**f**) abolished the response of PB^{Pdyn} neurons to gastric injection of water (**g**) or air (**h**), but thoracic level 5 spinal transection (T5x) (**i**) did not (**j**,**k**). Insets show average responses in the first 5 s of injection. Scale

bars, 100 μm. Data are mean ± s.e.m. **P<0.01. Statistics in Extended Data Table 1. Abbreviations in the Methods.
This figure is reprinted from (*99*).

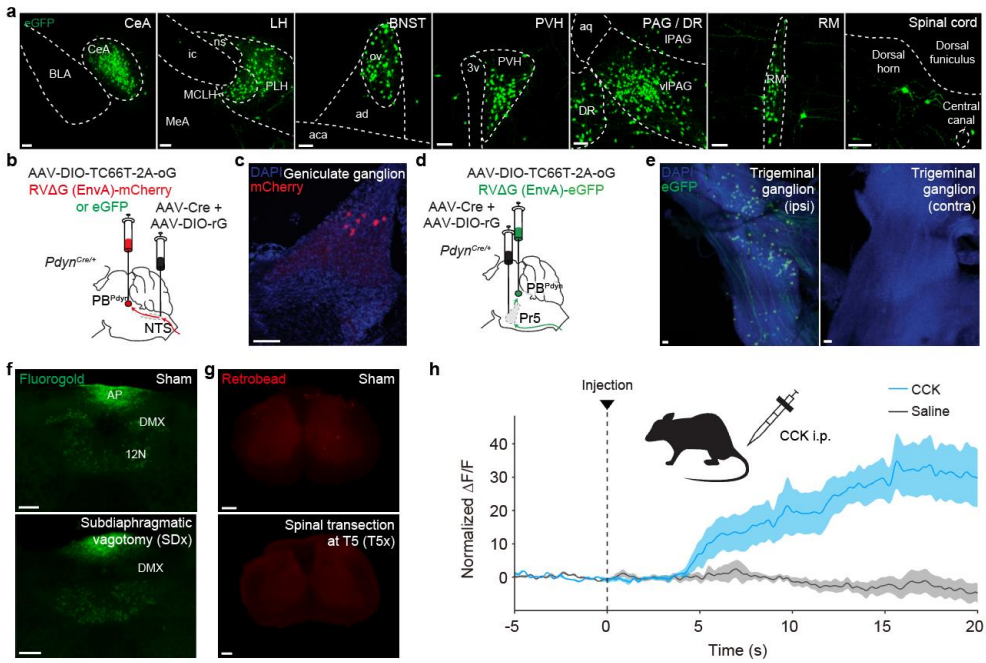

Figure 9. Mapping inputs to PB^{Pdyn} neurons. a, Identification of monosynaptic inputs to PB^{Pdyn} neurons using engineered rabies virus. Representative confocal images showing the input regions. **b–e**, Engineered rabies virus–mediated identification of monosynaptic inputs to PB^{Pdyn}–projecting rostral NTS neurons (**b**) and PB^{Pdyn}–projecting Pr5 neurons (**d**). Representative images showing labeled neurons in the geniculate ganglia projecting to the PB^{Pdyn}–projecting rostral NTS neurons (**c**) and neurons in the ipsilateral trigeminal ganglion projecting to the PB^{Pdyn}–projecting Pr5 neurons (**e**). **f**, Validation of subdiaphragmatic vagotomy. Following the intraperitoneal injection of retrograde neural tracer Fluorogold, many labeled vagal motor neurons were found in the dorsal motor complex of the sham control, but not in the vagotomized mice. **g**, Validation of spinal transection. Following the injection of retrograde neural tracer Retrobeads (Red RetroBeads; Lumafluor) in the PB, many labeled neurons were found in the spinal cord of sham controls, but not in the spinal cord–transected mice. **h**, Both electrophysiological and calcium imaging studies have demonstrated that vagal afferents that respond to gastric distension can be activated by CCK, a gut hormone released after a meal(*62*, *73*). If PB^{Pdyn} neurons receive gastric distension signals via mechanosensory vagal fibers, CCK treatment should also activate the PB^{Pdyn} population. Indeed, intraperitoneal CCK injection strongly activated PB^{Pdyn} neurons. Scale bars, 200 μm for (g), 100 μm for all else. Abbreviations in the Methods.

This figure is reprinted from (*99*).

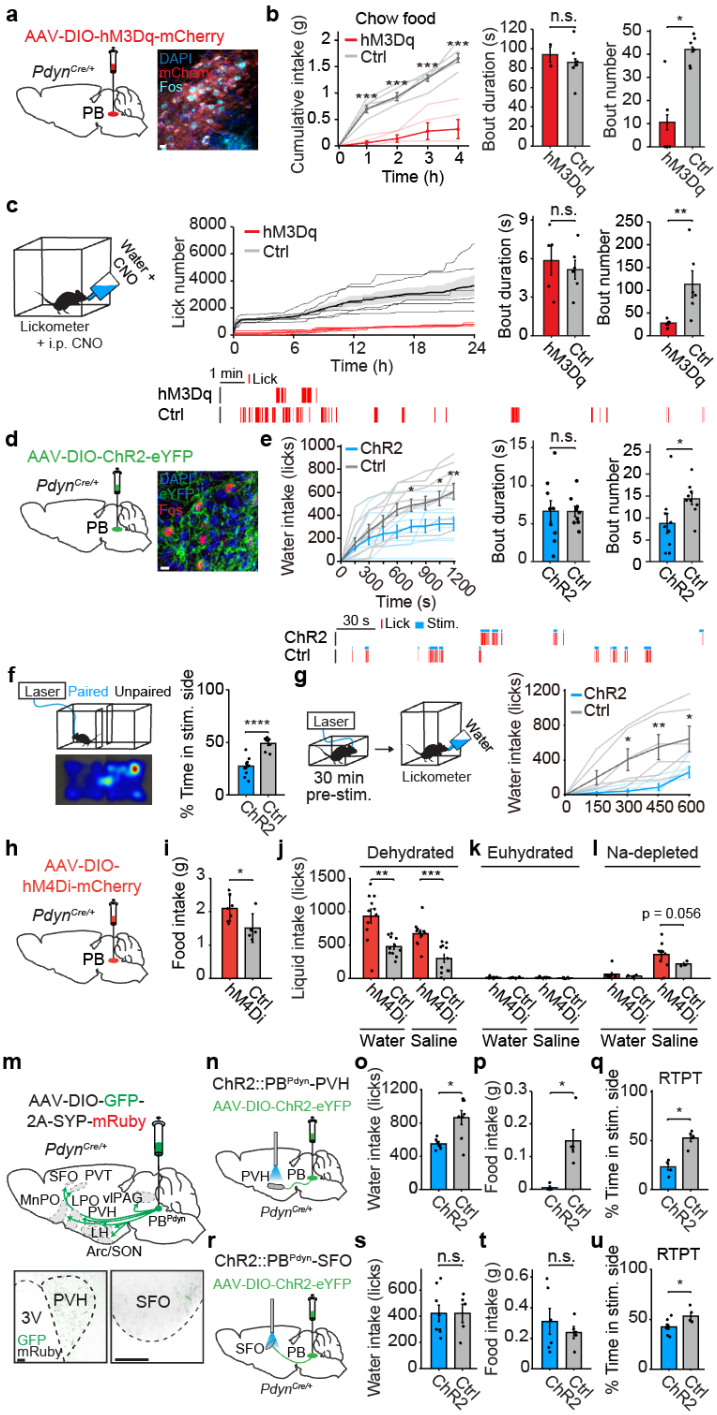

Figure 10. PB^{Pdyn} neurons transmit sustained appetite-suppressing signals to discourage the initiation of ingestion. a-c, Chemogenetic stimulation of PB^{Pdyn} neurons (a) suppressed food intake in food-deprived mice by decreasing bout number, not duration (b). This manipulation also inhibited water intake by decreasing bout number (c). Bottom, representative

example traces. Confocal image shows the high overlap between hM3Dq-expressing and CNO injection-induced Fos-expressing neurons. **d**, **e**, Lick-paired optogenetic stimulation of PB^{Pdyn} neurons (**d**) also did not affect bout duration, but reduced bout number to inhibit water intake (**e**), Bottom, representative example traces. Representative confocal image (**d**) shows the high overlap between ChR2-expressing and photostimulation-induced Fos-expressing neurons. **f**, Optogenetic stimulation of PB^{Pdyn} neurons was avoided in the real-time place preference test (RTPT). **g**, Pre-stimulation of PB^{Pdyn} neurons for 30 min before session produced sustained inhibition of drinking in dehydrated mice. **h-l**, Chemogenetic inhibition of PB^{Pdyn} neurons (**h**) increased the intake of chow food in fasted mice (**i**), and both water and hypertonic saline in dehydrated (**j**), but not in euhydrated mice (**k**). This manipulation tended to increase the intake of hypertonic saline in salt-depleted mice (**l**). **m**, Anterograde tracing for visualizing target structures using synaptophysin-mRuby fusion protein. Major PB^{Pdyn} neuron projection sites are indicated. Insets, Images showing two target structures, PVH and SFO. **n-q**. Optogenetic stimulation of PB^{Pdyn}-PVH projections (**n**) suppressed the intake of both water (**o**) and food (**p**) and induced avoidance in RTPT (**q**). **r-u**. Optogenetic stimulation of PB^{Pdyn}-SFO projections (**r**) did not affect the intake of water (**s**) or food (**t**), but induced avoidance in RTPT (**u**). Scale bars, 10 μm for (**a**) and (**d**), 100 μm for (**m**). Data presented as mean ± s.e.m. $*P<0.05$; $**P<0.01$, $***P<0.001$, $****P<0.0001$. n.s., not significant. Statistics in Table 1. Abbreviations in the Methods.

This figure is reprinted from (*99*).

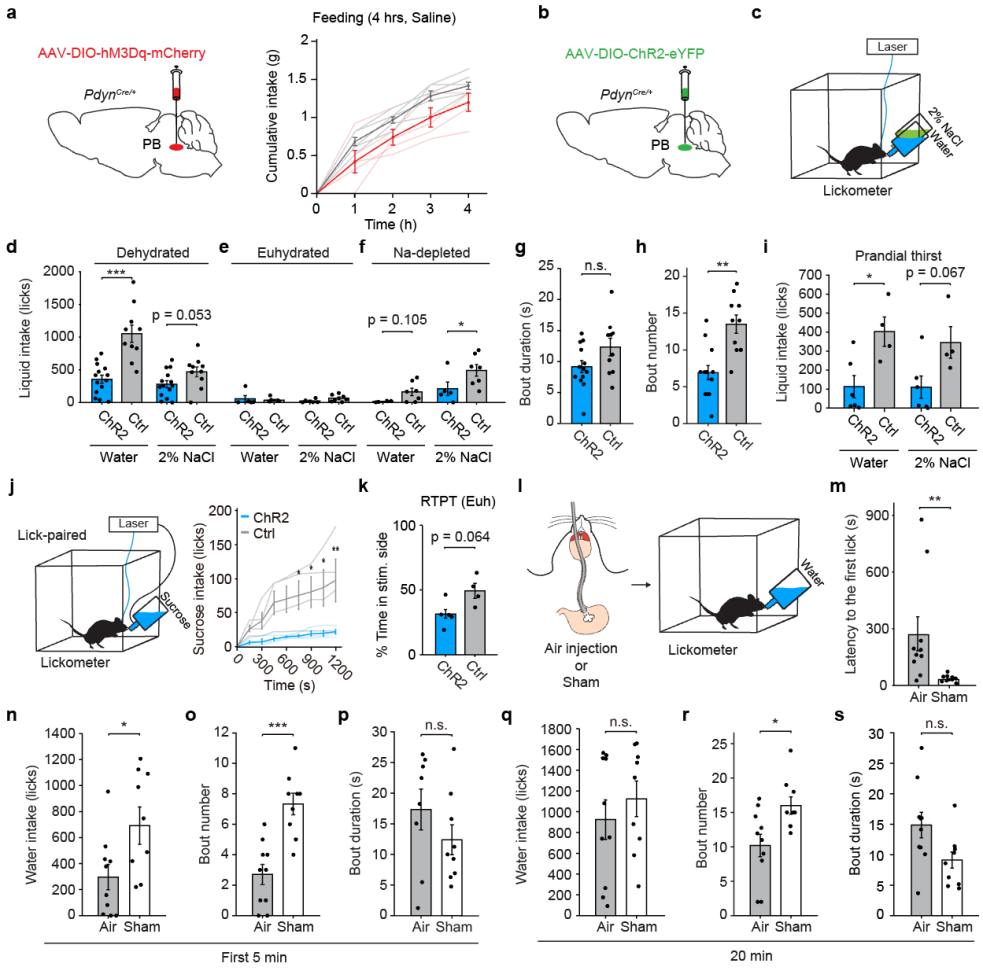

Figure 11. Activating PB^{Pdyn} neurons suppresses ingestion by reducing bout number, not duration, mimicking the symptoms of gastric distension. **a**, Saline control experiment for the experiment shown in Fig. 4b. **b**, Optogenetic stimulation of PB^{Pdyn} neurons. **c**, Mice were subjected to two-bottle test. **d**, In dehydrated mice, optogenetic stimulation of PB^{Pdyn} neurons significantly suppressed water intake and tended to inhibit hypertonic saline intake. **e**, In euhydrated mice, no effect was observed. **f**, In salt-depleted mice, the same manipulation significantly decreased hypertonic saline intake and tended to inhibit water intake. **g**,**h**, The suppression in water intake shown in (**d**) was not driven by reduced bout duration (**g**), but by decreased bout number (**h**). **i**, Food-deprived mice were offered food without water to induce prandial thirst. Stimulating PB^{Pdyn} neurons suppressed water intake and tended to inhibit hypertonic saline intake in mice with prandial thirst. **j**, *Ad libitum* fed, euhydrated mice were offered free access to sucrose solution (10%). Lick-paired optogenetic stimulation of PB^{Pdyn} neurons suppressed the intake of sucrose solution. **k**, Optogenetic stimulation of PB^{Pdyn} neurons in euhydrated mice

elicited a trend for avoidance in real-time place preference test (RTPT). **l**, Water-deprived mice received intragastric infusion of 1 ml of air (Air) or nothing (Sham) via oral gavage, and then were provided with free access to water. **m**, Intragastric air infusion significantly increased the latency to the first lick. **n-p**, In the first 5 min, Air group consumed significantly smaller amount of water compared with Sham group (**n**). This was driven by decreased bout number (**o**), but not bout duration (**p**). **q-s**, By 20 min from the water intake onset, the total amount of consumed water became comparable between the two groups (**q**). Air group exhibited a significantly smaller bout number (**r**) and a trend towards longer bout duration (**s**). Data presented as mean ± s.e.m. $*P<0.05$; $**P<0.01$; $***P<0.001$. n.s., not significant. Statistics in Table 1.
This figure is reprinted from (*99*).

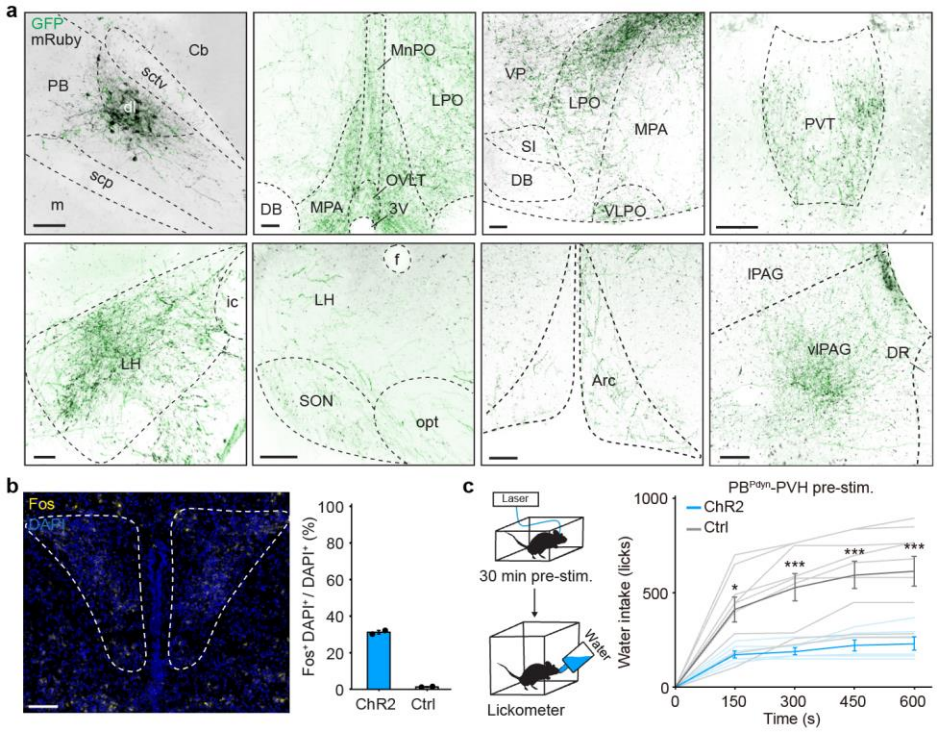

Figure 12. Projections of PB^{Pdyn} neurons and PB^{Pdyn}–PVH terminal optogenetic stimulations. a, Anterograde tracing for visualizing target structures using synaptophysin–mRuby fusion protein. Representative confocal images showing the PB injection site and target structures. Green, GFP; black, synaptophysin–mRuby. **b**, Optogenetic stimulation of PB^{Pdyn}–PVH projections activates postsynaptic PVH neurons, as indicated by increased Fos expression in the PVH, validating the optogenetic stimulation. Yellow, Fos; blue, DAPI. **c**, Optogenetic stimulation of the PB^{Pdyn}–PVH projection for 30 min before providing access to water (pre–stimulation) elicited sustained inhibition in drinking behavior in dehydrated mice for at least 10 min. Data presented as mean ± s.e.m. $*P<0.05$; $***P<0.001$. n.s., not significant. Statistics in Table 1. Scale bars, 100 μm. Abbreviations in the Methods.

This figure is reprinted from (*99*).

Table 1. Statistical analysis

Figure	Sample Size (numbers indicate mice unless otherwise stated)	Statistical Test	Values
1d	2 (Ai14-Water, Ai14-W-D, AAV-Water) 3 (AAV-W-D)	Unbalanced two-way ANOVA factor one: group (Ai14 vs AAV) factor two: condition (W-D vs W-D+Water) post-hoc correction for multiple comparisons (Fisher's least significant difference)	Double$^+$/Pdyn$^+$ Group: P = 0.0336 Condition: P = 3.31 ×10^{-6} F(3,5) = 267.9418 F(3,5) = 7.5280 Double$^+$/Fos$^+$ Group: P = 0.1676 Condition: P = 0.0087 F(3,5) = 14.6579 F(3,5) = 2.4624 P = 3.31 ×10^{-6} (Double$^+$/Pdyn$^+$, both Ai14 and AAV) P = 0.0087 (Double$^+$/Fos$^+$, both Ai14 and AAV)
1e	4 (Slc32a1, Slc17a6, Pdyn) 5 (Oxtr, Pdyn) 2 (Calca, Pdyn)		
2c-e	35 (Water) 11 (Empty bottle) 16 ($KHCO_3$) 21 (2% NaCl) 16 (Liquid food) 11 (Silicone oil) 13 (Hydrogel) 13 (Chow food) 8 (High-fat chow)	Kruskal-Wallis one-way ANOVA post-hoc correction for multiple comparisons (Fisher's least significant difference)	$P = 2.17\times10^{-12}$ $\chi^2(8,135) = 71.7773$ $P = 6.14\times10^{-9}$ (Water) $P = 4.15\times10^{-8}$ ($KHCO_3$) $P = 2.01\times10^{-9}$ (2% NaCl) $P = 4.74\times10^{-7}$ (Liquid food) $P = 0.0435$ (Silicone oil) $P = 0.0037$ (Hydrogel) $P = 0.0131$ (Chow food)
2f	12 (Empty bottle) 8 (Chow food) 6 (other conditions)	Pearson correlation	$R = 0.954$ $P = 0.0117$
2g	8 (average of 2 repeated trials)		
2h	8		
2j	4		
2k	6 (average of 2 repeated	One-way ANOVA post-hoc correction for	$P = 0.0026$ F(2,15) = 9.0764

	trials)	multiple comparisons (Fisher's least significant difference)	P = 0.1766 (200 vs 350) P = 0.0143 (350 vs 500) P = 0.0008 (200 vs 500)
2l	6 (average of 3 repeated trials)		
2m	4 (average of 3 repeated trials)		
3b, c	23 (Water) 12 (Empty bottle)		
3e, f	8	Wilcoxon rank-sum test (two-tailed)	Mouth $P = 1.55\times10^{-4}$ (mock vs water) $P = 1.55\times10^{-4}$ (mock vs oil) P = 0.2786 (water vs oil) Pharynx P = 0.0011 (mock vs water) P = 0.0207 (mock vs oil) P = 0.5737 (water vs oil) Esophagus $P = 6.22\times10^{-4}$ (mock vs water) $P = 1.55\times10^{-4}$ (mock vs oil) P = 0.8785 (water vs oil) Stomach $P = 6.22\times10^{-4}$ (mock vs water) $P = 3.11\times10^{-4}$ (mock vs oil) P = 0.8785(water vs oil)
3g	8		
3h	12		
3i	6 (average of 2 repeated trials)		
3j	3		
3k	10		
3l	5		
3n	4	One-way ANOVA	P = 0.4362 F(4,15) = 0.9904
3o	3 (0.9, 2% NaCl)	One-way ANOVA	P = 0.7273 F(3,10) = 0.4432

	4 (Water, 0.2% NaCl)		
3p	4	One-way ANOVA	*P* = 0.6921 F(2,9) = 0.3836
5b	8	Pearson correlation	*R* = 0.084 *P* = 0.42
5c; Center vs Periphery	8	Wilcoxon rank-sum test (two-tailed)	*P* = 0.104
5d; Open vs Closed	6	Wilcoxon rank-sum test (two-tailed)	*P* = 0.485
5e; Baseline vs Stroke	8 (average of 3 repeated trials)	Wilcoxon rank-sum test (two-tailed)	*P* = 0.2345
5f; Baseline vs Touch	4 (average of 5 repeated trials)	Wilcoxon rank-sum test (two-tailed)	*P* = 1
5g; Peanut butter vs Ctrl	4	Wilcoxon rank-sum test (two-tailed)	*P* = 0.8857
5i; ChR2 vs Ctrl	7, 4	Wilcoxon rank-sum test (two-tailed)	Laser ON *P* = 0.6485 Laser OFF *P* = 1
5j; hM3Dq vs Ctrl	5, 6	Wilcoxon rank-sum test (two-tailed)	CNO *P* = 0.4286 Saline *P* = 0.7922
6b	9 (Dehydrated) 7 (Euhydrated)		
6c	9 (Dehydrated) 7 (Euhydrated)	Wilcoxon rank-sum test (two-tailed)	Mouth *P* = 0.7577 (Water-Dehydrated vs Euhydrated) *P* = 0.000041 (Water-Dehydrated vs Mock) *P* = 0.0023 (Water-Euhydrated vs Mock) Pharynx *P* = 0.7577 (Water-Dehydrated vs Euhydrated) *P* = 0.000082 (Water-Dehydrated vs Mock) *P* = 0.0012 (Water-Euhydrated vs Mock) Esophagus *P* = 0.8371 (Water-Dehydrated vs Euhydrated) *P* = 0.000041 (Water-Dehydrated vs Mock) *P* = 0.0111 (Water-Euhydrated vs Mock)

			Stomach P = 0.6806 (Water-Dehydrated vs Euhydrated) P = 0.000041 (Water-Dehydrated vs Mock) P = 0.0012 (Water-Euhydrated vs Mock)
6d	7	Wilcoxon rank-sum test (two-tailed)	$P > 0.05$
6e	8		
7d, e	114 neurons from 4 mice (average of 5 repeated trials)		
7g	114 neurons from 4 mice (average of 5 repeated trials)	Pearson correlation	$R = 0.712$ $P = 7.17\times10^{-19}$
7j, k	107 neurons from 6 mice (average of 3 repeated trials)		
7l	107 neurons from 6 mice (average of 3 repeated trials)	One-way ANOVA post-hoc correction for multiple comparisons (Fisher's least significant difference)	$P = 1.61\times10^{-7}$ F(2,318) = 16.4373 $P = 5.82\times10^{-6}$ (200 vs 350) $P = 2.69\times10^{-7}$ (200 vs 500)
7o, p	97 neurons from 5 mice (average of 7 repeated trials)		
8c	3		
8g (inset)	5	Wilcoxon rank-sum test (two-tailed)	$P = 0.0079$
8h (inset)	5	Wilcoxon rank-sum test (two-tailed)	$P = 0.0079$
8j (inset)	4	Wilcoxon rank-sum test (two-tailed)	$P = 0.4857$
8k (inset)	4	Wilcoxon rank-sum test (two-tailed)	$P = 1$
9h	5		
10b (left, time-course plot); hM3Dq vs Ctrl	5, 6	Two-way repeated-measures ANOVA factor one: time factor two: group post-hoc correction for multiple comparisons (Bonferroni)	Time course (left) Interaction: $P < 0.0001$ Time: $P < 0.0001$ Group: $P < 0.0001$ F(4,36) = 32.64 F(4,36) = 76.14 F(1,9) = 59.26 1 h: $P < 0.0001$ 2 h: $P < 0.0001$

			3 h: $P < 0.0001$ 4 h: $P < 0.0001$
10b (middle, bout duration); hM3Dq vs Ctrl	2 (after excluding mice that did not show any intake), 6	Wilcoxon rank-sum test (two-tailed)	$P = 0.2571$
10b (right, bout number); hM3Dq vs Ctrl	5, 6	Wilcoxon rank-sum test (two-tailed)	$P = 0.0381$
10c (middle, bout duration); hM3Dq vs Ctrl	5, 6	Wilcoxon rank-sum test (two-tailed)	$P = 0.6623$
10c (right, bout number); hM3Dq vs Ctrl	5, 6	Wilcoxon rank-sum test (two-tailed)	$P = 0.0087$
10e (left, time-course plot); ChR2 vs Ctrl	9, 9	Two-way repeated-measures ANOVA factor one: time factor two: group post-hoc correction for multiple comparisons (Bonferroni)	Interaction: $P < 0.0001$ Time: P < 0.0001 Opsin: p<0.0317 F(8,128) = 5.400 F(8,128) = 54.27 F(1,16) = 5.543 750: $P = 0.0387$ 1050: $P = 0.0268$ 1200 p = 0.0018
10e (middle, bout duration); ChR2 vs Ctrl	9, 9	Wilcoxon rank-sum test (two-tailed)	$P = 0.8633$
10e (right, bout number); ChR2 vs Ctrl	9, 9	Wilcoxon rank-sum test (two-tailed)	$P = 0.0174$
10f; ChR2 vs Ctrl	11, 9	Wilcoxon rank-sum test (two-tailed)	$P < 0.0001$
10g; ChR2 vs Ctrl	6, 6	Two-way repeated-measures ANOVA factor one: time factor two: group post-hoc correction for multiple comparisons (Bonferroni)	Interaction: $P = 0.0081$ Time: $P < 0.0001$ Group: $P = 0.0198$ F(4,40) = 6.379 F(4,40) = 22.43 F(1,10) = 7.665 300: $P = 0.0197$ 450: $P = 0.0016$ 600: $P = 0.0126$
10i; hM3Dq vs Ctrl	7, 5	Wilcoxon rank-sum test (two-tailed)	$P = 0.0480$
10j; dehydrated hM4Di vs Ctrl	11, 11	Wilcoxon rank-sum test (two-tailed)	Water: $P = 0.0031$ 2% NaCl: $P = 0.00081$
10k; euhydrated hM4Di vs Ctrl	11, 6	Wilcoxon rank-sum test (two-tailed)	Water: $P = 0.9804$ 2% NaCl: $P = 0.1017$
10l; Na-depleted hM4Di vs Ctrl	11, 4	Wilcoxon rank-sum test (two-tailed)	Water: $P = 0.4767$ 2% NaCl: $P = 0.0559$
10o; ChR2 vs Ctrl	6, 8	Wilcoxon rank-sum test (two-tailed)	$P = 0.0293$
10p; ChR2 vs Ctrl	4, 5	Wilcoxon rank-sum test (two-tailed)	$P = 0.0159$
10q; ChR2 vs Ctrl	4, 5	Wilcoxon rank-sum test (two-tailed)	$P = 0.0159$
10s; ChR2 vs Ctrl	8, 5	Wilcoxon rank-sum test (two-tailed)	$P = 0.9433$
10t; ChR2 vs Ctrl	6, 5	Wilcoxon rank-sum test	$P = 0.8398$

		(two-tailed)	
10u; ChR2 vs Ctrl	8, 5	Wilcoxon rank-sum test (two-tailed)	$P = 0.0451$
11a; hM3Dq vs Ctrl	5, 6	Two-way repeated-measures ANOVA factor one: time factor two: group post-hoc correction for multiple comparisons (Bonferroni)	Interaction: $P = 0.1268$ Time: $P < 0.0001$ Group: $P = 0.0478$ F(4,36) = 1.928 F(4,36) = 159.8 F(1,9) = 5.245 Post-hoc tests: n.s. for all periods
11d; ChR2 vs Ctrl	14, 10	Wilcoxon rank-sum test (two-tailed)	Water: $P = 0.00025$ 2% NaCl: $P = 0.0532$
11e; ChR2 vs Ctrl	5, 7	Wilcoxon rank-sum test (two-tailed)	Water: $P = 0.2525$ 2% NaCl: $P = 0.4571$
11f; ChR2 vs Ctrl	5, 7	Wilcoxon rank-sum test (two-tailed)	Water: $P = 0.1048$ 2% NaCl: $P = 0.048$
11g; ChR2 vs Ctrl	13, 10	Wilcoxon rank-sum test (two-tailed)	$P = 0.1138$
11h; ChR2 vs Ctrl	13, 10	Wilcoxon rank-sum test (two-tailed)	$P = 0.0014$
11i; ChR2 vs Ctrl	6, 4	Wilcoxon rank-sum test (two-tailed)	Water: $P = 0.0381$ 2% NaCl: $P = 0.0667$
11j; ChR2 vs Ctrl	4, 4	Two-way repeated-measures ANOVA factor one: time factor two: group post-hoc correction for multiple comparisons (Bonferroni)	Interaction: $P = 0.0002$ Time: $P < 0.0001$ Group: $P = 0.0319$ F(8, 48) = 4.902 F(8, 48) = 12.30 F(1, 6) = 7.743 750: $P = 0.0360$ 900: $P = 0.0291$ 1050: $P = 0.0130$ 1200: $P = 0.0033$
11k; ChR2 vs Ctrl	5, 4	Wilcoxon rank-sum test (two-tailed)	$P = 0.0635$
11m; Air vs Sham	10, 9	Wilcoxon rank-sum test (two-tailed)	$P = 0.0021$
11n; Air vs Sham	10, 9	Wilcoxon rank-sum test (two-tailed)	$P = 0.0336$
11o; Air vs Sham	10, 9	Wilcoxon rank-sum test (two-tailed)	$P = 4.33 \times 10^{-4}$
11p; Air vs Sham	8, 9	Wilcoxon rank-sum test (two-tailed)	$P = 0.3704$
11q; Air vs Sham	10, 9	Wilcoxon rank-sum test (two-tailed)	$P = 0.4596$
11r; Air vs Sham	10, 9	Wilcoxon rank-sum test (two-tailed)	$P = 0.0138$
11s; Air vs Sham	10, 9	Wilcoxon rank-sum test (two-tailed)	$P = 0.0535$
11d; ChR2 vs Ctrl	14, 10	Wilcoxon rank-sum test (two-tailed)	Water: $P = 0.00025$ 2% NaCl: $P = 0.0532$
12b	2, 2		
12c; ChR2 vs Ctrl	6, 9	Two-way repeated-measures ANOVA factor one: time factor two: group post-hoc correction for multiple comparisons (Bonferroni)	Interaction: $P < 0.0001$ Time: $P < 0.0001$ Group: $P = 0.0028$ F(4, 52) = 12.66 F(4, 52) = 59.30 F(1, 13) = 13.45 150: $P = 0.0278$

			300: $P = 0.0007$ 450: $P = 0.0001$ 600: $P < 0.0001$

Chapter 3. A forebrain neural substrate for behavioral thermoregulation**

Abstract

Thermoregulatory behavior is a fundamental motivated behavior for maintaining body temperature homeostasis. Despite its critical importance, no forebrain region or defined neural population has been identified as required for this process. Here, I demonstrate that *Vgat*–expressing neurons in the lateral hypothalamus (LH^{Vgat} neurons) are required for a variety of thermoregulatory behaviors in mice. The activity of LH^{Vgat} neurons bidirectionally encodes thermal punishment and reward (P&R) and increases during thermoregulatory behavior. While these neurons regulate feeding and caloric reward as well, inhibiting parabrachial inputs selectively disrupted the encoding of thermal stimulus and thermoregulatory behaviors. Furthermore, a subpopulation of LH^{Vgat} neurons, which bidirectionally encodes thermal P&R, is revealed by using two-photon calcium imaging; this subpopulation is engaged during

** The material in this chapter is reprinted from:

S. Jung*, M. Lee*, D.-Y. Kim*, C. Son, B. H. Ahn, G. Heo, J. Park, M. Kim, H.-E. Park, D.-J. Koo, J. H. Park, J. W. Lee, H. K. Choe, S.-Y. Kim, A forebrain neural substrate for behavioral thermoregulation. *Neuron*. 110, 266-279.e9 (2022). *These authors contributed equally

thermoregulatory behavior, and largely separate from LH^{Vgat} neurons encoding caloric reward. This research establishes LH^{Vgat} neurons as a neural substrate required for behavioral thermoregulation and points to a key role for the thermal P&R–encoding subpopulation in mediating thermoregulatory behavior.

3.1. Introduction

Maintaining the body temperature within a narrow range that is optimal for molecular and cellular functions is vital for animal survival. When confronted with a thermal challenge, the brain initiates a series of behavioral and autonomic responses in order to maintain thermal homeostasis (*100*). In contrast to stereotyped autonomic responses (such as vasoconstriction, shivering and the production of heat in the brown adipose tissue [BAT]), is a motivated, goal–directed behavior that can flexibly manifest in a variety of ways, including moving to a warm place, performing operant behaviors to turn on a heat lamp, or building nests (*101–103*). In animals, such behavioral strategies are a preferred mode of thermoregulation, since these are more energy–efficient than autonomic processes (*103*). Although the neural circuits governing autonomic thermoregulation have received a great deal of attention, their counterparts in behavioral thermoregulation are still poorly

understood (*100*, *103*, *101*).

Several spinal and cranial pathways carry environmental temperature detected in the periphery to the brain (*100*, *104–107*). Among these, the spinoparabrachial pathway, which projects to the lateral parabrachial nucleus (LPB), is important for both autonomic and behavioral thermoregulatory responses (*100*, *108*). The LPB then relays thermosensory information to numerous forebrain areas involved in thermoregulation (*69*); the preoptic area (POA) and the dorsomedial hypothalamus (DMH) are prominent targets because they are closely associated with autonomic thermoregulation (*100*, *103*, *109*, *110*). However, lesion studies have revealed that both the POA and DMH are both unnecessary for most thermoregulatory behaviors (*111*, *112*, *100*, *103*, *101*). Despite numerous attempts over the years, no forebrain region, let alone a defined neural population, has been identified as being generally required for diverse thermoregulatory behaviors (*103*, *101*).

Considering that thermoregulatory behaviors are motivated, the lateral hypothalamus (LH), a key structure for a variety of motivated behaviors (*113–121*), represents a strong candidate for a forebrain area that is required for behavioral thermoregulation. The LH is anatomically well-positioned to mediate thermoregulatory behavior because it receives input from the thermosensory

parabrachial nucleus (PB) (*69*) and then projects to key brain areas that regulate the animal's motivational state, such as the midbrain periventricular thalamus, ventral tegmental area, and periaqueductal gray (PAG) (*116, 122–124*). The role of the LH in mediating thermoregulatory behavior, however, is debatable due to conflicting results from lesion experiments (*101*). LH lesions impaired thermoregulatory behavior in pioneering studies from the 1970s, but these were accompanied by deficits in motor functions, which made the interpretation difficult (*18*, *125*). Furthermore, in later studies, LH lesions were associated with no effects or sometimes even enhanced thermoregulatory behaviors (*126*, *127*). The fact that the LH is a very heterogeneous structure made up of numerous distinct neuronal types engaged in diverse aspects of behavior (*114, 116, 120, 128–130*), which could be indiscriminately damaged by the lesion experiments, may help to explain the inconsistent results of these lesion experiments. So, I reasoned that it might be possible to reveal the neural substrate in the LH that is critical for behavioral thermoregulation using cell-type-specific manipulations, recordings, and single-cell level neural activity imaging.

3.2. LH^{Vgat} neurons are necessary for diverse thermoregulatory behaviors

Previous research has shown that *Vgat*–expressing GABAergic neurons in the LH play an important role in motivated behavior (***114, 131, 122, 124, 132–136***). Thus, using chemogenetic tools, I investigated whether LH^{Vgat} neurons are necessary for the manifestation of diverse thermoregulatory behaviors (Figures 13A and 14A).

I started by testing mice in the self–heating operant task (*137*), where an active nose poke response turned on an infrared (IR) heat lamp for 2 seconds at a cold ambient temperature (Figures 13B, 14B and 14C). Surprisingly, the inhibition of LH^{Vgat} neurons significantly reduced this operant thermoregulatory behavior (Figures 13C and 14D). I then put the mice through the thermal gradient test, which probes instinctive thermoregulatory behavior (Figures 13D and 13G). Inhibiting LH^{Vgat} neurons interfered with mice's ability to choose the optimal–temperature position (Figures 13D–13I). Nest building, which is another innate cold–induced defence behavior in mice (Figures 13J–13L), as well as postural extension, which is a thermoregulatory behavior seen at high ambient temperatures (*138*) (Figures 13M and 13N), were both impaired by chemogenetic inhibition of LH^{Vgat} neurons. Thus, multiple thermoregulatory behaviors at both high and low ambient temperatures are impaired by chemogenetic inhibition of LH^{Vgat} neurons.

Since chemogenetic inhibition and other loss-of-function manipulations of LH^{Vgat} neurons, consistently had no effect on locomotion (*132*, *139*, *140*), these results cannot be attributable to motor impairment. Additionally, suppressing LH^{Vgat} neurons did not affect BAT thermogenesis, maintaining core body or tail temperature both in cold challenges and at baseline (Figures 13O, 14E, and 14F), indicating that these neurons are not necessary for autonomic thermoregulatory responses. Furthermore, behavioral responses to a painful thermal stimulus were unaffected by inhibiting these neurons (Figures 14G), indicating intact thermal nociception. Taken together, these data identify LH^{Vgat} neurons as a critical neural substrate required for behavioral thermoregulation.

3.3. LH^{Vgat} neurons are excited during thermoregulatory behavior and inhibited by thermal reward

The fact that LH^{Vgat} neurons are required for behavioral thermoregulation suggests that these neurons encode key aspects of thermoregulatory behavior, such as the behavioral response itself and the motivational properties of thermal stimuli. To investigate this, I used fiber photometry to record the real-time activity of LH^{Vgat} neurons (Figure 15A). I first recorded the activity of LH^{Vgat}

neurons when the mice were conducting the self-heating operant task (Figure 15B). Interestingly, LH^{Vgat} neurons were activated upon the nose poke responses but significantly inhibited by the heat stimulus that is subsequently delivered (Figure 15C). Because it brings the skin temperature closer to thermoneutrality, the heat stimuli delivered at cold ambient temperatures are rewards; indeed, the heat stimuli used in our experiments could induce approach behavior and serve as a positive reinforcer (Figures 14B and 14C). Thus, LH^{Vgat} neurons are excited during operant thermoregulatory behavior and inhibited by thermal reward.

Given that caloric reward intake has been shown to activate LH^{Vgat} neurons, the inhibitory responses of these neurons to thermal reward were unexpected (*141*); I also found that these neurons were activated by sucrose consumption (Figures 15D and 15E), and sucrose intake in an operant task (Figures 15F and 15G). Because the activity of LH^{Vgat} neurons was not correlated with either the onset of movement in a voluntary wheel running task or the movement velocity in an open-field chamber (Figures 15H–15K), the responses of these neurons are unlikely to be due to altered locomotor activity. These results collectively demonstrate that the LH^{Vgat} population is activated during thermoregulatory behavior and the intake of caloric reward but is inhibited by thermal reward.

Thus, I could conclude that LH^{Vgat} neurons not only play a crucial role in behavioral thermoregulation but these neurons also encode key aspects of thermoregulatory behavior.

3.4. LH^{Vgat} neurons bidirectionally encode thermal punishment and reward

Then, I systematically investigated the responses of LH^{Vgat} neurons to heat delivery at various ambient temperatures, ranging from low (8° C) to high (37° C), to reinforce and expand the finding that the activity of these neurons is inhibited by thermal reward, (Figure 16A). Even though heat stimulus is rewarding at low ambient temperatures, the same stimulus becomes unpleasant at high ambient temperatures because it causes the skin temperature to rise over thermoneutrality (Figures 14B and 14C). Consistent with earlier findings, LH^{Vgat} neurons were inhibited by heat stimuli delivered at low ambient temperatures, but, interestingly, the responses of these neurons were switched to excitation at high ambient temperatures (Figures 16B–16D). Therefore, the overall activity of the LH^{Vgat} population is inhibited by thermal reward but excited by thermal punishment.

I then investigated if similar responses are induced by a cold stimulus using a custom-made apparatus that could quickly and

reversibly supply mice with either ice-cold or ambient air (Figure 16E). Surprisingly, LH^{Vgat} neurons exhibited similarly bidirectional responses to the delivery of the cold stimulus (Figures 16F-16H); their activity was robustly increased upon the delivery of cold air at 8° C, whereas the same stimulus strongly suppressed these neurons at 37° C, and elicited intermediate responses at moderate temperatures. Since the cold stimulus is rewarding and aversive at high and low ambient temperatures, respectively, these data reinforce our previous results obtained using the IR heat stimulus: the activity of LH^{Vgat} population is decreased by thermal reward and increased by thermal punishment.

Collectively, our results demonstrate that LH^{Vgat} neurons bidirectionally encode thermal punishment and reward (P&R), which are key motivational properties of thermal stimuli, independent of the temperature of the thermal stimuli. Since motivated behaviors could be elicited in two forms, avoiding punishments and seeking rewards (*142*, *143*), it is possible that the encoding of thermal P&R by LH^{Vgat} neurons plays a crucial role in mediating behavioral thermoregulation.

3.5. LH^{Vgat} neurons receive direct inputs from the thermosensory LPB

Next, I investigated how LH^{Vgat} neurons get the information required to support behavioral thermoregulation and encode the motivational properties of thermal stimuli. To answer this question, I used an engineered retrograde viral vector to map and quantify the monosynaptic inputs to LH^{Vgat} neurons; which revealed numerous inputs from throughout the brain (Figures 17A–17L, see Methods). Importantly. robust inputs were found in the LPB (Figure 17D), which is thought to relay thermosensory signals from the spinal cord to forebrain regions that enable thermoregulation (*69*, *100*). Therefore, in the following experiments, I focused on examining the LPB input to the LH.

First, I discovered that distinct subpopulations of the LPB represent cold and hot thermal punishments (i.e. two thermal stimuli that are equivalent in valence but distinct in temperature), which probably correspond to warm− and cold−sensitive LPB neurons previously identified (*144–146*). In contrast, almost half of the LH neurons encoding cold thermal punishment were also activated by hot thermal punishment (Figure 18), which may explain the excitatory responses of LH^{Vgat} neurons to thermal punishment independent of the stimulus temperature (Figure 16). *Slc17a6*, but not *Slc32a1*, was expressed by the majority of LPB neurons that projected to LH^{Vgat} neurons, and optogenetic activation

of their terminals in the LH caused strong Fos expression in LH^{Vgat} neurons (Figures 17M–17Q), demonstrating the excitatory nature of the LPB–LH projection.

3.6. Parabrachial inputs are required for thermoregulatory behavior and the neural coding of thermal reward by LH^{Vgat} neurons

I then investigated the requirement of LPB activity in neural coding of thermal reward and behavioral thermoregulation. First, chemogenetic suppression of LPB neurons decreased self–heating behavior, supporting previous studies demonstrating that the LPB is required for cold– and heat–avoidance behaviors (*108*) (Figures 19A, 19B and 20A). Since this manipulation had no effect on equivalent operant tasks for caloric reward (Figure 19C) and even increased *ad libitum* food intake (Figures 19D), the effect of inhibiting the LPB was specific to thermoregulatory behavior at least to some extent. Additionally, this manipulation abolished the responses of the LH^{Vgat} population to thermal reward, but not caloric reward (Figures 19E–19G). Thus, the LPB is only necessary for both the encoding of thermal reward by LH^{Vgat} neurons and thermoregulatory behavior, but not for the neural coding of caloric reward by these neurons and feeding behavior.

Considering that there is a prominent monosynaptic innervation from the thermosensory LPB to LH^{Vgat} neurons (Figure 17D), I tested the role of this projection in mediating behavioral thermoregulation. Surprisingly, chemogenetic inhibition of the projections of LPB neurons in the LH impaired the self-heating behavior, but not *ad libitum* food intake and the sucrose-seeking operant task (Figures 19H-19K and 20B). Since the same manipulation unaffected core body temperature maintenance and BAT thermogenesis in a cold environment, this pathway is not necessary for autonomic thermoregulation (Figures 19L and 20C). Notably, both were compromised when LPB cell bodies were inhibited (Figures 19M and 20D), which is consistent with the LPB's known role in both autonomic and behavioral thermoregulation (*100*, *103*).

3.7. The LH^{Vgat} subpopulation encoding thermal punishment and reward is largely distinct from the caloric reward-encoding subpopulation

As shown by the dissociation of feeding and thermoregulatory behaviors, and of caloric and thermal rewards (Figure 19) our data strongly suggest the existence of two functionally different LH^{Vgat} subpopulations: one that is underlying feeding behavior and caloric

reward, and the other underlying thermoregulatory behavior and thermal reward. So, I used photon calcium imaging to investigate this possibility.

I started by examining how individual LH^{Vgat} neurons represented caloric and thermal stimuli (Figures 21A and 22A). Thermal reward largely caused inhibition, whereas caloric reward and thermal punishment mostly provoked activation among all LH^{Vgat} neurons registered throughout different experiments (260 neurons from 12 mice) (Figure 21B), in accordance with the findings of fiber photometry experiments (Figures 15 and 16). The population activity vector for both thermal punishment and reward were nearly orthogonal to the population vector for the caloric reward (Figure 21C), which implicates distinct representations of caloric and thermal stimuli in the LH^{Vgat} population. Indeed, there were many neurons selectively responsive to caloric or thermal stimuli or nonresponsive (Figure 21D), and a clustering analysis identified three distinct, almost equally divided subpopulations of LH^{Vgat} neurons that exhibit corresponding response profiles (Figures 21E, 21F, and 22B). Overall, cluster 1 neurons did not respond to caloric reward but did bidirectionally encode thermal P&R. In contrast, neurons from cluster 2 responded to caloric reward but were relatively silent to thermal stimuli. Most of the neurons in cluster 3

were unresponsive. According to response profiles to each stimulus, clusters appeared to be distinguishable from one another (Figure 21G).

In line with the findings from the clustering analysis, I discovered that thermal reward-inhibited neurons largely overlapped with thermal punishment-activated neurons (Figures 21H and 22C). In addition, the thermal P&R-encoding subpopulation was significantly separate from the neuron encoding caloric reward (Figure 21I). The responses of caloric reward-encoding neurons and thermal P&R neurons were stronger for caloric and thermal stimuli, respectively, which indicates the preferential neural coding by each subpopulation (Figure 21J). Collectively. these data reveal the existence of two functionally distinct subpopulations in LH^{Vgat} neurons: the caloric reward-encoding subpopulation and the thermal P&R subpopulation.

The response selectivity of thermal P&R neurons was further characterized, and it was found that only a few neurons in this population were activated by oral administration of a bitter tastant and that this small subset did not significantly overlap with those that were inhibited by foot-shock omission (Figure 23). This shows that thermal P&R neurons are at least partially tuned to thermal stimuli. However, given that thermal P&R neurons were

also activated by electric foot shock (Figure 23D), these neurons could encode other aversive somatosensory stimuli as well.

3.8. The LH^{Vgat} subpopulation bidirectionally encoding thermal punishment and reward is engaged during thermoregulatory behavior

Next, by monitoring the calcium dynamics of individual LH^{Vgat} neurons during the self-heating operant task, I examined how these neurons represent thermoregulatory behavior. A lever press in this head-fixed version of the operant task triggered the delivery of an IR heat as a thermal reward (Figure 24A). As a result, 20% of the neurons were responsive to lever press responses among the neurons registered throughout all experimental sessions (112 neurons from 7 mice), and they were mostly excited (Figure 24B), which is consistent with the findings from the fiber photometry recordings (Figure 15C).

Surprisingly, the lever press-excited neurons and the thermal P&R neurons showed significant overlap (Figures 24C-24E). In addition, the LH^{Vgat} neurons activated by a lever press significantly responded to both thermal reward and punishment, and thermal P&R neurons were on average significantly excited by a lever press (Figure 24F and 24G). Within lever press-encoding and

thermal P&R neurons, the response amplitudes to lever press and thermal punishment were not significantly different. Together, during thermoregulatory behavior, the LH^{Vgat} subpopulation encoding thermal P&R is engaged. This suggests that this subpopulation plays a significant role in mediating thermoregulatory behavior.

3.9. Activation of LH^{Vgat} neurons induces unspecific behavioral disturbances

As inhibiting LH^{Vgat} neurons disrupts thermoregulatory behavior, does activating the same population facilitate or trigger thermoregulatory behavior? This does not appear to be the case, as chemogenetic excitation of LH^{Vgat} neurons elicited gnawing behavior (Figures 25A–25D), which is consistent with previous reports (*139*, *147*). These gnawing responses could be a consummatory behavior brought on by activating the LH^{Vgat} subpopulation that encodes consummatory behavior, or it could be an aberrant behavioral disturbance elicited by unspecific and artificial activation of multiple heterogeneous LH^{Vgat} subpopulations, (*132*, *135*, *133*). Thus, these results may emphasize the requirement for more precise targeting and activation of functionally distinct LH^{Vgat} subpopulations to conduct meaningful gain–of–function experiments.

3.10. Discussion

It is well documented that the POA is a forebrain center that coordinates various autonomic thermoregulatory responses. Contrarily, the region required for and serving a comparable central function in multiple thermoregulatory behaviors has not yet been revealed (*103*, *101*). Several hypothalamic areas are shown to be necessary for some types of thermoregulatory behaviors, but it was limited to certain thermoregulatory actions occurring under specific conditions. For instance, the POA is necessary for the postural extension in hot conditions (*148*) but is not required for operant thermoregulatory behavior (*111*, *112*); the DMH is required for the cold-seeking behavior brought on by systemic inflammation, but not for the warmth-seeking behavior at low ambient temperatures nor for the cold-seeking behavior at high ambient temperatures (*149*). Additionally, lesions in these areas severely disrupt autonomic thermoregulation (*150–152*), occasionally leading to an increase in thermoregulatory behaviors as a form of compensation (*153*, *111*, *112*). Here I demonstrated the necessity of LH^{Vgat} neurons for a variety of thermoregulatory behaviors, which are flexibly manifested under various circumstances, such as migration to thermoneutral locations, nest-building, altering body posture,

and executing operant behaviors for thermoregulation without affecting thermal nociception, thermosensation itself, and autonomic thermoregulatory responses (Figures 131 and 14). These are the first identification of a neural substrate in the forebrain, which is generally required for various thermoregulatory behaviors.

According to the prevailing view, the LPB transmits thermosensory information from the periphery to forebrain areas for both autonomic and behavioral thermoregulation (*100*, *108*). There is sufficient evidence to support the necessity of its projections to the POA in autonomic thermoregulation (*154*, *155*, *146*, *100*, *103*). Although it has not been determined, it is unlikely that the LPB–POA pathway is necessary for behavioral thermoregulation, given that the POA is dispensable for the majority of thermoregulatory behaviors (*153*, *111*, *112*). On the other hand, I looked into the function of the LPB–LH pathway and found that this pathway is necessary for behavioral, but not autonomic, thermoregulatory responses (Figures 19H, 19I, 19L, and 20C). Collectively, it is intriguing to hypothesize that the LPB may recruit divergent projection arms to the POA and the LH to coordinately trigger and regulate autonomic and behavioral thermoregulatory responses, respectively. However, additional research has to be done to determine the precise contribution of the projections from

the LPB to the POA and other targets in behavioral thermoregulation.

The LH^{Vgat} subpopulation encoding thermal P&R that is identified in our two-photon studies was largely distinct from the subpopulations encoding caloric reward (Figure 21), showed some response selectivity to thermal stimuli (Figure 23), and was engaged during thermoregulatory behavior (Figure 24). Thus, this thermal P&R-encoding LH^{Vgat} subpopulation may represent a more precise neuronal substrate that mediates behavioral thermoregulation. If so, what precise function would thermal P&R neurons have in mediating behavioral thermoregulation? Even though I were not able to directly assess the sufficiency of this subpopulation in facilitating or triggering thermoregulatory behavior, our imaging data suggest that these neurons play a significant role in motivating thermoregulatory behavior for several reasons. First, thermal punishment, which would raise the animal's motivation to escape from the stimulus, activated thermal P&R neurons (Figure 21). On the other hand, thermal reward, which would lessen the motivation to avoid aversive thermal conditions, suppressed the activity of these neurons. Given that the same neurons were also activated during thermoregulatory behavior (Figure 24), the simplest explanation is that the activity of thermal P&R neurons

represents motivation to avoid thermal punishment. This interpretation fits well with the abundance of research linking the LH to motivating behavior (*113–120*). This view postulates that the loss of motivation to avoid thermal punishment brought on by inhibiting thermal P&R neurons may account for the observed impairment of behavioral thermoregulation by the inhibition of the entire LH^{Vgat} neurons (Figure 13). Notably, while thermal P&R neurons were largely distinct from neurons encoding a variety of aversive and rewarding stimuli, all of the thermal P&R neurons were activated upon delivering electric foot shock (Figure 23), which leaves the possibility that these neurons may also mediate behavioral responses upon other aversive somatosensory stimuli.

Other than behavioral thermoregulation, LH^{Vgat} neurons have been linked to a variety of motivated behaviors, including feeding, predation, social behavior, and object investigation (*114*, *116*, *122*, *124*, *139*). A pioneering study revealed that distinct subsets of LH^{Vgat} neurons represent appetitive and consummatory behaviors by monitoring the activity of individual LH^{Vgat} neurons (*132*). Here, I also discovered two functionally different LH^{Vgat} subpopulations that encode the caloric reward and thermal P&R (Figure 21). Additionally, although it overlapped with foot shock–activated neurons, the thermal P&R–encoding LH^{Vgat} subpopulation was

largely separate from other LH^{Vgat} subpopulations encoding various rewarding (foot shock omission) and aversive (bitter tastant) stimuli (Figure 23). According to these findings, diverse stimuli may recruit different neuronal ensembles within the LH^{Vgat} population to elicit appropriate motivated behaviors. Specific access to these subpopulations to conduct gain-of-function and loss-of-function manipulations would be required for causal testing of the hypothesis.

In light of this, recent research has described the genetic diversity of LH neurons by using single-cell RNA-seq approaches (*129*, *130*) and demonstrated the functional investigation of LH^{Vgat} subpopulations defined by their molecular markers (*156–158*). These suggest that functionally defined LH^{Vgat} subpopulations could be mapped onto molecularly distinct subtypes, but this may require a combinatorial use of several molecular markers (*159*, *23*), and such a mapping could not be feasible for several functionally defined subclusters (*160*, *161*). As a different strategy, a recent study showed that it was possible to dissect the LH^{Vgat} subpopulation according to their projection targets (*124*). Accordingly. to further characterize the responses of some LH^{Vgat} subpopulations, defined by the projection target (PAG) or molecular markers (*Nts* or *Tac2*) to caloric and thermal stimuli; however, these subpopulations did

not show a preferential response to either kind of stimulus (Figures 25E–25M). Additionally, the projection patterns of LH neurons that were activated by caloric reward and thermal punishment were similar, suggesting potential difficulties in the projection–based selective targeting of these subpopulations (Figure 26). Future research may provide a strategy to specifically target caloric reward– or the thermal P&R–encoding neurons. Meanwhile, direct multiphoton stimulation or inhibition of LH^{Vgat} ensembles *in vivo* could be another possible way for determining the causal role of LH^{Vgat} subpopulations independently from projection targets and molecular markers (*162*, *163*).

Furthermore, LH^{Vgat} neurons would work in concert with other circuits that mediate autonomic responses to synergistically regulate the thermal homeostasis of an animal. How the circuits mediating distinct thermoregulatory modalities interact to yield the final behavioral and physiological changes is an unexplored area of study, and our discovery of a forebrain neural substrate for behavioral thermoregulation provides a point of entry for this investigation at the cellular level.

3.11. Methods

Animals

Wild-type or heterozygous C57BL/6J mice (C57BL/6J mice, JAX stock no. 000664; *Vgat*$^{Cre/+}$, JAX stock no. 016962; Fos$^{iCreER/+}$, JAX stock no. 030323; Ai14, JAX stock no. 007914; *Nts*$^{Cre/+}$, JAX stock no. 017525; *Vgat*$^{FlpO/+}$, JAX stock no. 029591) or heterozygous mice from C57BL/6N background (*Tac2*$^{Cre/+}$, a gift from David J. Anderson, Caltech) were used. To label and visualize neurons in an activity-dependent manner, I bred the Fos$^{iCreER/+}$ mouse line crossed with the Ai14 (Cre-dependent tdTomato reporter) mouse line. Mice were housed in a temperature- and humidity-controlled room with a 12-h light/dark cycle. Mice were given *ad libitum* food and water in their home cages unless stated otherwise. Male and female mice of at least eight weeks of age were used for data collection. Mice in each litter were randomly assigned to either the experimental or control group. All behavioral procedures were performed in the dark cycle. For efficient delivery of thermal stimuli, the mice were shaved at their dorsum. All experimental protocols were approved by the Seoul National University Institutional Animal Care and Use Committee.

Abbreviations

The abbreviations used in the figure panels are as follows: aca, anterior commissure; AcbC, nucleus accumbens core; AcbSh,

nucleus accumbens shell; Arc, arcuate hypothalamic nucleus; Cla, claustrum; DMH, dorsomedial hypothalamus; DRN, dorsal raphe nucleus; Ins, insular cortex; LPO, lateral preoptic nucleus; mlf, medial longitudinal fascicle; MPB, medial parabrachial nucleus; MPO, medial preoptic nucleus; MRN, midbrain reticular nucleus; LPB, lateral parabrachial nucleus; LPBc, central LPB; LPBd, dorsal LPB; LPBel, external lateral LPB; LPBs, superior LPB; PAG, periaqueductal grey; PB, parabrachial nucleus; Pe, periventricular hypothalamic nucleus; scp, superior cerebellar peduncles; sctv, ventral spinocerebellar tract; SuM, supramammillary nucleus; VMH, ventromedial hypothalamic nucleus; VMPO, ventromedial preoptic nucleus; VTA, ventral tegmental area.

Viral constructs

The recombinant AAV vectors expressing GCaMP6m (AAV1-hSyn-FLEX-GCaMP6m, 1.2×10^{13} copies/ml; AAV1-Syn-GCaMP6m-WPRE-SV40, 2.02×10^{12} copies/ml), eGFP (AAV1-hSyn-eGFP-WPRE-bGH, 3.86×10^{12} copies/ml), and tdTomato (AAV1-CAG-Flex-tdTomato-WPRE-bGH, 3.86×10^{12} copies/ml) were obtained from the Penn Vector Core. The AAV vectors expressing hM4Di (AAV8-hSyn-DIO-hM4D(Gi)-mCherry, 4.0×10^{12} copies/ml), hM3Dq (AAV8-hSyn-DIO-

hM3D(Gq)-mCherry, 3 × 10^{12} copies/ml), Cre recombinase (AAVretro-EF1α-fDIO-Cre, 9,14 × 10^{12} copies/ml), and mCherry (AAV8-hSyn-mCherry, 1.70 × 10^{13} copies/ml) were obtained from Addgene. The AAV vectors expressing mCherry (AAV5-EF1a-DIO-mCherry, 3.2 × 10^{12} copies/ml), ChR2 (AAV2-hSyn-hChR2(H134R)-eYFP-WPREpA, 3.9 × 10^{12} copies/ml), eYFP (AAV5-hsyn-eYFP, 6.6 × 10^{12} copies/ml), TVA receptor (AAV8-EF1α-Flex-TVAcherry, 5.4 × 10^{12} copies/ml), and rabies virus envelope glycoprotein (AAV8-CA-Flex-RG, 2.5 × 10^{12} copies/ml) were obtained from the UNC vector core. The AAV vectors expressing optimized rabies G protein (*85*) and enhanced-expression TVA receptor (*86*) (AAV8-DIO-TC66T-2A-oG, 1.64 × 10^{13} copies/ml) and the recombinant EnvA-pseudotyped G-deficient rabies virus vector expressing mCherry or eGFP (RV-EnvA-ΔG-mCherry, 3.78 × 10^{7} TU/ml; RV-EnvA-ΔG-EGFP, 2.26 × 10^{8} TU/ml) were obtained from the Salk vector core. The AAV vectors expressing mRuby-tagged synaptophysin (AAV DJ-hSyn-FLEX-mGFP-2A-Synaptophysin-mRuby) were obtained from the Stanford Vector Core.

Surgery

Mice were placed in a stereotaxic apparatus (David Kopf Instruments) while resting on a heating pad under 1.5–3.0% isoflurane anesthesia. Following a scalp incision, small craniotomies were performed in regions of interest using a hand drill (Saeshin, 208B). A given amount of viral vectors was injected at 40–100 nl/min into each target site using a pressure microinjection system (Nanoliter 2000) with a pulled glass capillary. The coordinates for the LH were −1.40 mm anteroposterior (AP), ±1.00 mm mediolateral (ML), and −5.35 mm dorsoventral (DV); in some mice, for bilateral cannula implants, I targeted the same region at a 10-degree angle relative to the sagittal plane (−1.30 mm AP, ±1.91 mm ML, −5.05 mm DV). The coordinates for the LPB were −5.30 mm AP, ±1.35 mm ML, and −3.4 mm DV; for bilateral cannula implants, I targeted the same region at a 10−degree angle relative to the sagittal plane (−5.30 mm AP, ±1.89 mm ML, −2.97 mm DV). The coordinates for the DMH were −2.0 mm AP, ±0.4 mm ML, and −5.1 mm DV; for bilateral cannula implants, I targeted the same region at a 20−degree angle (−2.0 mm AP, ±2.12 mm ML, −4.66 mm DV). The coordinates for the PAG were −4.1 AP, ±1.05 ML, and −2.55 mm DV. For all unilateral injections and implantations, the choice of the left or right hemisphere was counterbalanced. After injection, the capillary was slowly retracted (0.01 mm/s) to

prevent backflow of fluids. The incision was closed by sutures and tissue adhesives (Vetbond), and the mice were provided with analgesics and antibiotics. To recover from anesthesia, the mice were placed in a clean cage on a heating pad and then returned to their home cage. Mice were kept in the cage for 4 weeks for recovery and viral expression before behavioral testing.

For chemogenetic modulation experiments, 200 nl of recombinant AAVs expressing Cre-dependent hM4Di, hM3Dq, or mCherry were bilaterally injected into the LH of *Vgat*$^{Cre/+}$ mice and AAVs expressing hM4Di, eGFP, eYFP, or mCherry were bilaterally injected into the LPB of C57BL/6J mice. In some cases, injection guide cannulas (C315G/SPC; P1 Technologies) were bilaterally implanted 500 μm above the target site for intracranial injection. The cannulas were affixed to the skull using C&B Metabond (Parkell) and dental cement. After surgery, dummy cannulas (C315DC/SPC; P1 Technologies) were inserted to prevent the guide cannula from contamination, and mice were kept in the home cage for 1 week for recovery before behavioral testing. The dummy cannula protruded beyond the guide cannula by ~300 μm to prevent blood clotting at the tip of the guide cannula.

For fiber photometry experiments in the LH, 200 nl of recombinant AAVs expressing Cre-dependent GCaMP6m (1:8-1:11

dilution) were unilaterally injected into the LH of *Vgat*$^{Cre/+}$, *Nts*$^{Cre/+}$, or *Tac2*$^{Cre/+}$ mice. For the expression of GCaMP6m in PAG-projecting LH^{Vgat} neurons, retrograde AAVs expressing Flp-dependent Cre recombinase were injected into the PAG, and AAVs expressing Cre-dependent GCaMP6m were injected into the LH of *Vgat*$^{FlpO/+}$ mice. For fiber photometry experiments in the LPB, 200 nl of recombinant AAVs expressing GCaMP6m (1:16 dilution) were unilaterally injected into the LPB of C57BL/6J mice. A low-autofluorescence fiberoptic cannula (400 μm core, 0.48 NA; Doric lenses or 400 μm core, 0.37 NA; Inper) was implanted 0–50 μm above the virus injection site. The fiberoptic cannula was affixed to the skull, as described above.

For two-photon calcium imaging of LH^{Vgat} neurons, 500 nl of recombinant AAVs expressing Cre-dependent or Flp-dependent GCaMP6m (1:15 or 1:1 dilution, respectively) were unilaterally injected into the LH of *Vgat*$^{Cre/+}$ or *Vgat*$^{FlpO/+}$ mice (−1.20 mm AP, ±1.00 mm ML, −5.30 mm DV), slightly anterior to the imaging site to minimize cell death within the field of view. Two weeks after the virus injection, a GRIN lens (130-000150; 7.3 mm length, 0.6 mm diameter; Inscopix or 1LWN050P146055NN; 7.1 mm length, 0.5 mm diameter; Go!Foton) was implanted above the LH (−1.30 mm AP, ±1.00 mm ML, −5.15 mm DV). After the implantation of the

GRIN lens, a custom-made stainless steel ring for head-fixation (*88*) was attached around the lens, and both ring and lens were affixed to the skull with dental cement.

For rabies tracing experiments, 200 nl of recombinant AAVs expressing Cre-dependent TVA (a modified avian retroviral receptor, TC66T) and an optimized rabies glycoprotein (oG) (*86*) were injected into the LH of $Vgat^{Cre/+}$ mice. Three weeks later, 100 nl of G-deficient EnvA-pseudotyped rabies virus (RV⊿G) was injected into the LH. After 1 week, the mice were sacrificed for histological analyses.

For optogenetic stimulation experiments, 200 nl of recombinant AAVs expressing channelrhodopsin-2 (ChR2) or eYFP were bilaterally injected into the LPB, and 200 nl of recombinant AAVs Cre-dependently expressing tdTomato were bilaterally injected into the LH of $Vgat^{Cre/+}$ mice. Fiberoptic cannulas (200 μm core, 0.22 NA; Newdoon or Inper) were bilaterally implanted 100 μm above the LH. The cannulas were affixed to the skull using C&B Metabond (Parkell) and dental cement.

For labeling the activated neurons and their axon terminals using TRAP mouse line, 200 nl of recombinant AAVs expressing Cre-dependent mRuby-tagged synaptophysin were unilaterally injected into the LH of $Fos^{iCreER/+}$ mice.

Chemogenetic manipulations

To chemogenetically manipulate hM4Di- or hM3Dq-expressing neurons, 200 μl of 0.9% saline or CNO (BML-NS105; Enzo or HB6149; Hellobio) was intraperitoneally injected into mice 45 min before the initiation of the behavioral test session. For chemogenetic inhibition experiments, 10 mg/kg of CNO (4 mM, prepared in 0.9% sterile saline) was injected into mice unless stated otherwise. CNO at 10 mg/kg is commonly used for chemogenetic inhibition experiments (*164–166*). For chemogenetic activation experiments, 1 mg/kg of CNO (0.4 mM, prepared in 0.9% sterile saline) was injected into the mice. For chemogenetic inhibition of LPB terminals in the LH or DMH, 0.9% saline or CNO (200 nl per hemisphere, 1 mM, prepared in 0.9% sterile saline; BML-NS105; Enzo) was injected into the target sites through guide cannulas. Before the intracranial injection, a 10 μl Hamilton syringe filled with distilled water was connected to the internal cannula through PE tubing. Saline or CNO solution was loaded using a microinjection syringe pump (UMP3; WPI) to which the Hamilton syringe was attached. The syringe pump was connected to a microprocessor-based controller (Micro4; WPI). The dummy cannula was removed from the guide cannula 15 min before task

initiation, and the internal cannula was inserted into the guide cannula. Then, 200 nl of saline or CNO solution was bilaterally infused into the target sites at 100 nl/min using a microinjection syringe pump. The internal cannula was removed 1 min after termination of the infusion.

Optogenetic manipulations

To stimulate the axon terminals of ChR2-expressing neurons, 10-15 mW of blue light (318-477 mW/mm^2 at the tip of the patch cords) generated by a 473 nm laser (MGL-III-473; OEM Laser Systems) was delivered to the mice through fiberoptic patch cords (200 μm diameter, 0.22 NA; Newdoon). The laser output was controlled using a pulse generator (Pulse Pal; Sanworks) to deliver 10-ms light pulses at 20 Hz.

For Fos experiments, mice were single-housed at least a week before the experiment. On the day of the experiment, blue light was delivered to the LH to stimulate the LPB terminals in the LH for 2 h. After the experiment, the mice were sacrificed and histologically processed for immunohistochemical labeling of Fos.

Behavioral assays

For the self-heating operant task, mice were placed in an acrylic

chamber (20 × 23.5 × 32.5 cm^3) equipped with an IR lamp (250 W) and two nose-poke ports (Sanworks). A nose poke to one of the two ports resulted in a 2-s IR delivery (active nose poke); a nose poke to the other port had no programmed consequences (inactive nose poke). A Bpod State Machine (Sanworks) recorded nose-poke responses and controlled the IR lamp. The ambient temperature inside the chamber was set to 8° C unless stated otherwise. Mice were trained for 1 h per day until the rate of active nose pokes (number of active nose pokes / number of total nose pokes × 100) was more than 60% for three consecutive days. Mice that did not meet the learning criterion were excluded from the experiment. During post-training test sessions, I calculated the normalized response by dividing the number of nose-poke responses on each day (i.e., day 1, 2, or 3) by the number of nose-poke responses on the first day of the test session (i.e., day 1) of each mouse. For the self-heating operant task with gnawing material, a wooden stick was introduced into the test chamber.

For the thermal gradient test, mice were placed in a linear chamber (90 × 10 × 10 cm^3) with a floor temperature gradient and were allowed to freely explore the chamber to select the optimal-temperature position. Each end of the metal plate was attached to a temperature-controllable liquid circulation system

that established a continuous temperature gradient from 15° C to 50° C or 15° C to 40° C across the floor. The ambient temperature was set to 8° C or 37° C. Experiments were recorded using a video camera, and the location of the mice was automatically detected using video tracking software (EthoVision; Noldus). Data from the last 30 min of the 1-h session were used for analysis.

For the nest-building test, mice were acclimated to nesting materials (cotton nestlets, 5 × 5 cm^2; Ancare) in their home cages for several days. In the home cage or a novel cage, each mouse was provided with nesting material for 90 min at an ambient temperature of 15° C. Each nesting material was photographed before and after each session for normalization. Outlines for the nesting material were traced, and the number of pixels for each area was then counted using ImageJ software (National Institutes of Health).

To examine postural extension, mice were placed in a behavioral chamber (25 × 25 × 25 cm^3) at an ambient temperature of 37° C for 40 min. Behavior during the experimental session was recorded using a video camera outside a transparent wall, and the duration of postural extensions was manually counted afterward. Since postural extension reduces the heat production by muscle activity and increases heat dissipation by increasing body surface area (*167*), it is classified as a thermoregulatory behavior

observed in a hot environment (*101*, *103*). The postural extension was defined as a prone position with a straightened spine, forelegs folded beneath the neck, and hindlegs positioned backward (*138*, *148*, *101*).

For the thermal preference test, mice freely explored two indistinguishable chambers (each 50 × 25 × 25 cm^3) for 15 min. Entry into one of the chambers turned on an IR lamp for 2 s every 4 s to provide sufficient heat without overheating. The choice of the paired chamber was counterbalanced across mice. The time spent in each chamber was measured using EthoVision.

For the *ad libitum* feeding assay, mice food-deprived for 24 h were placed in a chamber (17 × 32 × 13 cm^3) and provided *ad libitum* access to food chow for 20 min. Mice were habituated to the chamber one day in advance with food chow for 30 min. The weight of the food chow was measured before and after each trial to estimate the amount of food consumed.

For the FR1 operant task for caloric reward, mice were placed in a custom-made soundproof chamber (25 × 20 × 15 cm^3) with active and inactive nose ports to undergo training for 1 h per day. An active nose-poke response resulted in the delivery of 10 μl of 10% sucrose solution to the same nose port. Each sucrose delivery was followed by a 10-s timeout. Mice were maintained on

food deprivation by limiting access to food for 2 h per day.

For the hot plate test, mice were placed in an acrylic chamber (10 × 14 × 30 cm^3) floored by a thermoelectric Peltier plate (CP-065; TE Tech) connected to a temperature controller (TE Tech; TC720). The temperature of the plate was set to 52° C during the 150-s experimental session. Behavior was recorded using a video camera. The number of jumps and the latency to first jump were manually counted.

BAT, core body, and tail temperature measurement

To measure BAT or core body temperature upon a cold challenge, a miniature telemetric transponder (IPTT-300; BioMedic Data Systems) was implanted beneath the interscapular BAT or in the abdominal cavity of anesthetized mice. Of note, I implanted only one probe per mouse to avoid signal interference between the probes. After a week of recovery, the mice were placed in an acrylic chamber (10 × 14 × 30 cm^3) floored by a thermoelectric Peltier plate (CP-065; TE Tech) connected to a temperature controller (TE Tech; TC720). The temperature of the plate was set to 32° C during the 30-min baseline recording period. Following this baseline recording, the plate was rapidly cooled to 5° C over 2 min and maintained at this temperature for 35 min. The BAT or core

body temperature was measured using a wireless scanner (DAS-8007; BioMedic Data Systems) every 5 min.

To monitor tail vasoconstriction in response to the cold challenge, thermographic images of the mouse tail were taken with an IR camera (E4; FLIR). The cold challenge was performed as described above. The temperature value was acquired from the thermographic image at 1 cm from the base of the tail. An average of two or more temperature data points was used for each time point.

To monitor the core body temperature at room temperature, a telemetric transponder was implanted as described above. Single-housed mice recovered for at least a week before the measurement. The temperature was measured using a wireless scanner for 2 h every 15 min.

For BAT and tail temperature measurements at room temperature, mice were single-housed for more than a week. On the test day, thermographic images of the shaved mouse dorsum and tail were captured using an IR camera every 15 min to acquire temperature data.

Fiber photometry

Real-time fiber photometry recordings were conducted as

previously described (*168*). Briefly, two excitation lights from LEDs (470 nm and 405 nm; M470F3/M405F1; Thorlabs) were sinusoidally modulated by an RZ5P processor (Tucker Davis Technologies) at 211 Hz and 531 Hz, respectively, and the light pulses were delivered to brain target regions via a low-autofluorescence fiberoptic patch cord (400 μm core, 0.48 NA; Doric Lenses). The light intensity during the recording was below 30 μW for both 470 nm and 405 nm lights (measured at the tip of the patch cord). The emitted fluorescence signal was detected using a femtowatt photoreceiver (2151; Newport). The resulting signal was demodulated, amplified, and collected by the RZ5P processor at a sampling rate of ~1 kHz.

For the self-heating operant task, mice were trained as described above, with the exception that a delay of 1 s was introduced between the active nose poke and the delivery of the 2-s IR heat stimulus to temporally separate the two events, such that the neuronal responses to the nose poke and the IR heat stimulus can be isolated. In addition, an 850-nm long-pass filter (FGL850H; Thorlabs) was added below the IR lamp to completely block visible light. A Bpod State Machine (Sanworks) recorded the nose-poke responses and controlled the IR lamp with TTL pulses. The pulse was split and fed into the RZ5P processor to record the time point

of IR heat delivery. Each IR delivery was followed by a 10-s timeout period.

For the *ad libitum* drinking assay, the mice were food-deprived for 48 h. On the test day, the mice were placed in a soundproof chamber with a lickometer (Med Associates). Following a 5-min acclimatization period to the chamber with the spout blocked, mice were provided with *ad libitum* access to 30% sucrose solution or liquid food for 30 min. Event timestamps marking individual licks were generated and fed into the RZ5P processor.

For the FR1 operant task for sucrose reward, food-deprived mice were placed in a soundproof chamber (Med Associates) with two nose-poke ports. The nose-poke response to the active port turned on a syringe pump to deliver 10 μl of 30% sucrose solution to a spout located between the two ports over 1 s. Each sucrose delivery was followed by a 10-s timeout period. Mice were maintained on food deprivation by limiting access to food for 2 h per day.

For voluntary wheel running, the mice were habituated to a treadmill in their home cages for at least a week before the experiment. On the test day, each mouse was placed in a chamber ($25 \times 25 \times 25$ cm^3) with a treadmill for 10 min. Voluntary running was recorded using a video camera and manually analyzed

to extract the time points for movement onsets.

For the open-field test, mice were placed in an open-field chamber (50 × 50 × 40 cm^3) while recording the activity of the neurons for 15 min.

To deliver heat stimuli, mice were placed in a chamber (20 × 23.5 × 32.5 cm^3) equipped with an IR lamp (250 W). After 5 min of baseline recording, the mice received IR irradiation for 2 s every 1 min for 30 min. The ambient temperature was set to 8° C, 20° C, 32° C, or 37° C. An 850-nm long-pass filter (FGL850H; Thorlabs) was added below the IR lamp to completely block visible light.

To deliver cold air stimuli, mice were placed in a custom-made chamber (17 × 17 × 22 cm^3) to which ambient air was continuously supplied by a fan (140 mm diameter) through a circular opening in a wall. This opening led to another chamber supplied with either cold air or ambient air from separate circular inlets (140 mm diameter) and fans controlling airflow on either side. In this chamber, the delivery of air at different temperatures was achieved by operating only one of the two side fans at any given moment with custom-made circuitry, including solid-state relays linked to a pulse generator. An aluminum block was attached to a temperature-controllable liquid circulation system to cool the

delivered air. The ambient temperature was set to 8° C, 20° C, 32° C, or 37° C. After 5 min of baseline recording, the mice were provided with a 10-s cold air delivery per min for 30 min.

To test the role of the LPB in the encoding of caloric reward by LH^{Vgat} neurons, mice were placed in a custom-made soundproof chamber (25 × 20 × 15 cm^3) with active and inactive nose ports to undergo training for 1 h per day. An active nose-poke response resulted in the delivery of 10 μl of 10% sucrose solution to the same nose port. Each sucrose delivery was followed by a 10-s timeout. Mice were maintained on food deprivation by limiting access to food for 2 h per day.

All data were analyzed using custom-written MATLAB codes. The photometry signal was analyzed as previously described; Ca^{2+}-dependent fluorescence signals normalized to Ca^{2+}-independent fluorescence as a proxy for the overall activity of the GCaMP-expressing neuronal population (*91*). Briefly, data were low-pass-filtered at 2 kHz, downsampled to 100 Hz, and a linear function scaled the 405-nm signal to the 470-nm signal to obtain the fitted 405-nm signal. The ratio ΔF/F was calculated as (raw 470 nm signal - fitted 405 nm signal) / (fitted 405 nm signal). Peri-event time plots were created using the TTL timestamps generated by the Pulse Pal pulse generator, Bpod State Machine,

and lickometer or the timestamps marked in manual video analyses. The animal ' s location and velocity were measured using EthoVision.

The normalized ⊿F/F ratio was calculated as follows: Average baseline ⊿F/F values were subtracted from individual raw ⊿F/F values, and the difference was divided by the standard deviation of the baseline. For peri-event time plots, the baseline was defined as the 5-s (e.g., licking bout, port entry for sucrose reward, or voluntary wheel running in Figure 15) or 10-s (e.g., IR heat or cold air delivery and nose-poke responses for sucrose reward in Figures 2 and 3) time window preceding the event onset. For peri-event time plots of nose-poke responses in the self-heating operant task, the baseline was defined as the time window of 10 to 5 s before the IR heat delivery. Licking bouts were defined as any set of more than three consecutive licks, in which the inter-lick interval was less than 3 s. To determine the significance of the population response, the average calcium activities from the response time window and the baseline (indicated in the legend for each experiment) were compared using the Wilcoxon signed-rank test or Wilcoxon rank-sum test.

Two-photon calcium imaging

Two-photon calcium imaging was performed using a two-photon microscope (Olympus FVMPE-RS) equipped with a fast resonant scanner, GaAsP-PMT detector, 20× air objective lens (Olympus LCPLN20XIR, 0.45 NA, 8.3 mm working distance), and a tunable Mai-Tai DeepSee laser (Spectra-Physics). For all experimental sessions, imaging parameters were as follows: imaging frequency, 5 Hz (images acquired at 30 Hz using the fast resonant scanner were frame-averaged); laser power, 130–540 mW; PMT voltage, 650 V; gain, 1; offset, 3%; scan size, 512 × 512; and zoom, 1.

Mice were habituated to head fixation for five consecutive days. Mice were food-deprived for 24 h before feeding experiments. For feeding experiments, 20 μl of liquid food was delivered to the mouth at 120 μl/min using a blunt 22-gauge needle. For heat stimuli, IR heat was delivered to the dorsum of the mice for 5 s. By circulating ice-cold or 40° C water through a metallic custom-designed thermal box, the ambient temperature was set to approximately 8° C or 37° C. Each session consisted of 10–20 trials, and the intertrial interval was pseudo-randomized between 50 s and 80 s. To deliver general aversive stimuli, mice were placed on the metal grid floor. After 300 s of baseline recording, I orally administered 10 μl of quinine (5 mM) for 0.5 s or delivered electric foot shocks (0.4 mA) for 2 s to the mice. Each session

consisted of 15 trials, and the intertrial intervals were set to 120 s for quinine delivery and 70 s for the delivery of electric foot shock. For the foot-shock omission test, after 300 s of baseline recording, mice received mild electric foot shocks (0.1 mA) during the entire session except for 10 s per trial, with an intertrial interval of 70 s. For the self-heating experiment, mice were trained before the test sessions on a fixed ratio 1 (FR1) schedule for 30-60 min to press a lever to receive a 1-s IR heat stimulus. The ambient temperature was set to 8° C in the custom-designed thermal box, as described above. On the first day of training, IR heat stimuli were delivered immediately after a lever press. As mice learned to press the lever, I delayed the IR heat delivery, gradually increasing the lag to up to 2 s to dissociate the neuronal responses to lever presses and IR heat stimuli. The mice were trained for at least 4 days before imaging. In the imaging session, after 300 s of baseline recording, the lever was presented to the mice, and the FR1 self-heating operant task was conducted for 30 min. During training and test sessions, a Bpod State Machine (Sanworks) recorded the lever press responses and controlled the IR lamp with TTL pulses.

Two-photon calcium imaging analysis

Time-series images from each behavioral session trial were

concatenated using ImageJ, processed by a non-rigid motion correction algorithm (NoRMCorre), and the regions of interest (ROIs) for each neuron across different experimental sessions were tracked and drawn manually on the standard deviation projection or average intensity projection of the movies created by ImageJ. Trials with excessive motion artifacts were excluded before concatenation. The average fluorescence signal in each ROI was extracted using ImageJ and analyzed using custom-written MATLAB code. The ratio $\Delta F/F$ was calculated as $(F-F_0) / F_0$, where F_0 is the median fluorescence of the baseline period for each trial. The baseline was defined as 10 s before the onset of the event. Normalized $\Delta F/F$ values were calculated by subtracting individual raw $\Delta F/F$ values with average baseline $\Delta F/F$ values, and dividing the difference by the standard deviation of the $\Delta F/F$ of the baseline.

Individual neuronal responses to each event were characterized using receiver operating characteristic (ROC) curve analyses. Area under ROC (auROC) curves were calculated by comparing the distribution of baseline $\Delta F/F$ with the distribution of $\Delta F/F$ (0–10 s after the onset of each event). K-means clustering was conducted on the concatenated auROC curves from three events (IR heat delivery at 8° C, 37° C, and liquid food consumption) using the function "kmeans" from the MATLAB

statistics toolbox. The optimal number of clusters, K, was selected as follows: I changed K from 2 to 10, repeated K-means clustering five times for each K, and calculated the maximum Calinski-Harabasz index among the five clustering results. The K with the maximum Calinski-Harabasz index was chosen as the optimal number of clusters. Maximal iteration was set to 1,000, and the clustering was repeated 1,000 times to find the global optimum with the least within-cluster sums of point-to-centroid distances.

To describe the population representations of LH^{Vgat} neurons for thermal and caloric stimuli, I created multidimensional population vectors (each dimension corresponding to the activity of one neuron) for each frame from 0 s to 10 s after the onset of the stimulus. I used the auROC score, which is calculated as 2 × auROC − 1 (to scale the value from −1 to 1), as the elements of the population vectors. Then, I averaged all population vectors representing each stimulus to obtain the mean population vector. To calculate the angles between two population vectors, I divided the dot product of the two population vectors with the product of the norm of the vectors and set the value to the inverse cosine function.

To identify neurons responsive to IR heat stimuli and liquid food deliveries, I binned the $\Delta F/F$ time course for 10 s following the onset of each stimulus by 5 frames (1 s) and performed a

Wilcoxon signed-rank test for each bin (as compared to the baseline) with Bonferroni correction for multiple comparisons (P<0.05). I considered neurons with two consecutive responsive bins (2 s) as responsive. To determine neurons responsive to quinine, foot shocks, and foot-shock omission, I averaged the ⊿F/F time course for 5 s following the onset of each stimulus and compared it to the mean of the baseline using the Wilcoxon signed-rank test. To determine neurons responsive to lever presses, I averaged the ⊿F/F ratio from 5 s before to 2 s after the onset of a lever press and compared them to the mean of the baseline, which was defined as from 10 s to 5 s before the lever press, using the Wilcoxon signed-rank test.

I calculated how unexpected the overlap between two neuronal populations was using a hypergeometric distribution, as described previously by another group (*166*). Briefly, I used a hypergeometric distribution depending on P—the probability of having *E1* success (the number of neurons responsive to event #1) given the total number of imaged neurons—and *E2* (the number of neurons responsive to event #2). The extent to which the amount of overlap was unexpected was calculated using the MATLAB functions "hygecdf" and "hygestat".

TRAP induction

The drug 4-hydroxytamoxifen (4-OHT; HB2508; Hellobio) was prepared as previously described (*169*). In short, 50 mg of 4-OHT was dissolved in 2.5 ml ethanol (at a concentration of 20 mg/ml) at 37° C while shaking, then stored at −20° C for subsequent experiments. Before use, 4-OHT was dissolved by shaking at 37° C for 10 min, and corn oil (C8267; Sigma-Aldrich) was added for a final concentration of 10 mg/ml 4-OHT. After evaporating the ethanol in a vacuum at 37° C, the final 4-OHT solution was injected intraperitoneally at a dose of 50 mg/kg. For labeling activated neurons using the TRAP reporter mouse line ($Fos^{iCreER/+}$ mice crossed with Ai14 tdTomato reporter mice) (*170*, *171*) in Figure S2, mice were injected with 4-OHT and kept 1 week after the injection to allow the expression of tdTomato in TRAPed neurons before sacrificing the mice. For labeling the activated neurons and their axon terminals using the TRAP mouse line ($Fos^{iCreER/+}$ mice) in Figure S7, mice were kept 6 weeks after the injection of 4-OHT to allow the expression of mRuby-tagged synaptophysin in the axon terminals before sacrificing the mice.

To label neurons activated by heat delivery at 37° C using the TRAP reporter system (Figure S2) or to label neurons activated by thermal punishment and their axon terminals (Figure

S7), mice were placed in a chamber (20 × 23.5 × 32.5 cm^3) equipped with an IR lamp and an ambient temperature of 37° C. The mice received IR irradiation for 2 s every 1 min for 2 h, and 4-OHT was injected 1 h after the initiation of the IR delivery.

To label neurons activated by cold air delivery at 8° C using the TRAP reporter system (Figure S2), mice were placed in a custom-made chamber (17 × 17 × 22 cm^3) with a cold ambient temperature of 8° C. The mice received a 10-s cold air stimulus per min for 2 h, and 4-OHT was injected 1 h after the start of the cold air delivery.

To label neurons, and their axon terminals, activated by liquid food intake (Figure S7), single-housed mice were placed in their home cages and allowed to freely consume liquid food following 1-day food deprivation. 4-OHT was injected 1h after the start of the consumption.

Histology and microscopy

Mice were anesthetized and transcardially perfused with ice-cold 1 × phosphate-buffered saline (PBS), then 4% paraformaldehyde (PFA) solution in PBS. Brains were extracted, fixed overnight in 4% PFA solution, and equilibrated in 30% sucrose solution before being cut into 50-μm-thick sections using a freezing microtome

(Leica SM2010R). Slices were stored in a cryoprotectant solution (5:6:9 mixture of glycerol, ethylene glycol, and PBS, respectively) at 4° C. Sections were then washed in PBS, incubated for >30 min in 1:25,000–1:50,000 4′,6-diamidino-2-phenylindole (DAPI) solution, washed again in PBS, and mounted on microscope slides with PVA-DABCO. Confocal images were obtained using a Zeiss LSM 880 laser scanning microscope with a 10×/0.45 NA or 40×/1.2 NA objective lens.

For rabies tracing experiments, 30-μm-thick coronal slices were collected from the whole brain. The sections were washed in PBS and permeabilized with 0.1% Triton X-100 and 3% normal donkey serum (NDS; Jackson ImmunoResearch) for 40 min. Incubation with anti-2A peptide antibody (1:500, ABS31; MERCK) was performed overnight in 3% NDS/PBS solution, followed by washing and incubation with secondary antibodies (Alexa 647-conjugated donkey anti-rabbit IgG, 1:500; Abcam) for 4 h at room temperature. These sections were washed, stained with DAPI (1:25,000), and mounted as described above. Sections were imaged using a Zeiss Axio Scan.Z1 slide scanner (provided by SNU CMCI), and cells were counted semiautomatically using IMARIS software (Bitplane). Representative confocal images were acquired using a Zeiss LSM 880 laser scanning microscope with a 20×/1/.0 NA

objective lens.

Fos immunohistochemistry

Brain slices (100 μm thick) containing the LH or LPB were collected as described above and washed in PBS. The sections were permeabilized with 0.1% Triton X-100 and 3% NDS for 2 h. Incubation with anti-Fos primary antibody (rabbit anti-Fos, 1:1,000, 2250S; Cell Signaling Technology) was performed by shaking at 4° C for 48 h in 3% NDS/PBS solution. After incubation, the sections were washed more than three times in PBS, stained with secondary antibodies (Alexa 647-conjugated donkey anti-rabbit IgG, 1:500; Abcam) for 1 day at 4° C, and incubated at room temperature for 3 more hours. Then, the sections were washed in PBS, stained with DAPI (1:25,000), mounted, and imaged as described above.

Fluorescence in situ hybridization

After transcardial perfusion of mice with ice-cold PBS, the brains were harvested. The brains were immersed in optimal cutting temperature compound (Tissue-Tek), fresh-frozen using dry ice, and stored at −80° C until further processing. Brains were sectioned at 20 μm using a cryostat and mounted onto Superfrost

Plus slides (25 × 75 × 1 mm^3; Fisherbrand), fixed in 4% PFA for 15 min, and washed in 50%, 70%, 100%, and 100% ethanol for 5 min each. After air-drying for 5 min, the samples were treated with protease for 30 min, washed twice in PBS, and again treated with probes that were heated in a 40° C water bath for 10 min prior to use. Then, the slides were placed in a 40° C humidified oven for 2 h, washed in RNAscope wash buffer twice for 2 min each, and subjected to amplifier hybridization according to the user manual (#320293; Advanced Cell Diagnostics). Finally, samples were stained with DAPI (Advanced Cell Diagnostics) for 30 s and immediately covered with ProLong Gold Antifade mounting medium (Thermo-Fisher).

Quantification and statistical analysis

Statistical analyses were performed using MATLAB (MathWorks) or Prism (GraphPad). I used the two-tailed Wilcoxon rank-sum test, two-tailed Wilcoxon signed-rank test, one-way ANOVA with subsequent Dunn's post hoc test, one-way repeated-measures ANOVA with subsequent Dunn's post hoc test, two-way repeated-measures ANOVA with subsequent Bonferroni post hoc test, Friedman's test with subsequent Dunn's post hoc test, Pearson correlation, paired t-test, and hypergeometric distribution

test depending on the experimental paradigm. Significance levels were defined as $*P<0.05$, $**P<0.01$, $***P<0.001$, and $****P<0.0001$. Details of the tests and statistical information are listed in Table S1. Data are presented as the mean ± SEM. No statistical approaches were used to determine the sample size, blinding, or randomization methods. Viral expression and implant placement were verified by histology before the mice were included in the analysis. Quantification of the fluorescence intensities was performed using ImageJ. To normalize fluorescence intensities, the fluorescence intensity of each area was divided by the averaged fluorescence intensity of the LH.

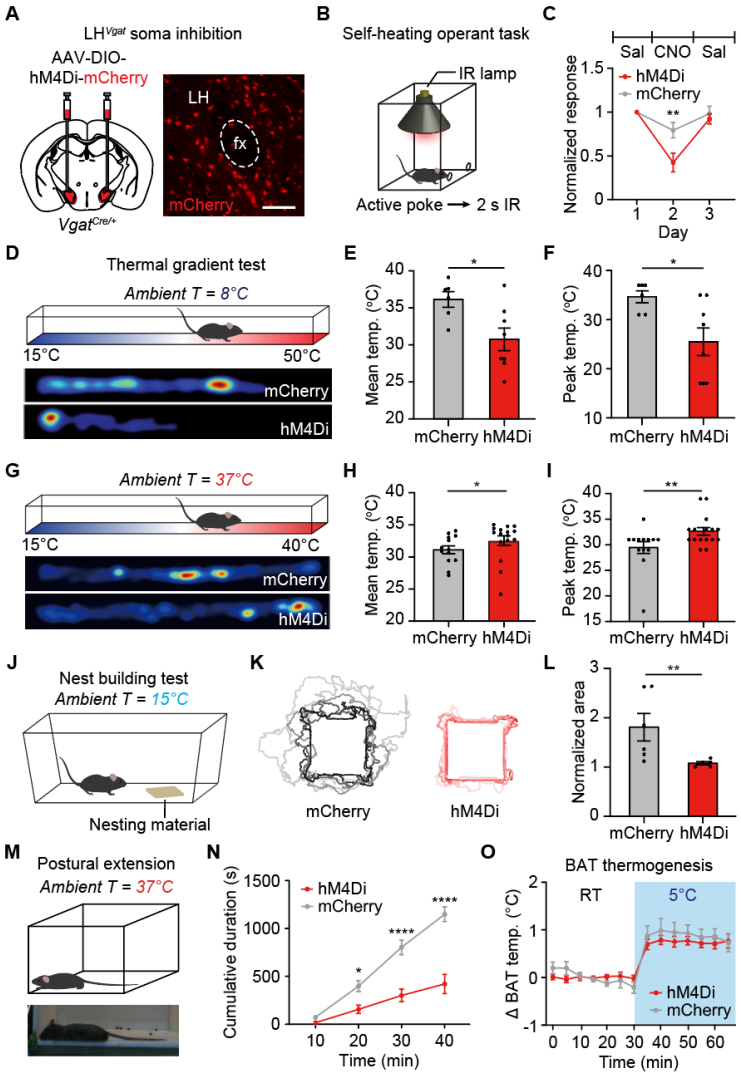

Figure 13. LH^{Vgat} neurons are necessary for diverse thermoregulatory behaviors

(A) Scheme of the chemogenetic inhibition of LH^{Vgat} neurons (left). Representative image showing the expression of mCherry fused to hM4Di (right). fx, fornix. Scale bar, 100 μm.

(B and C) Self-heating operant task (B). Chemogenetic inhibition of LH^{Vgat} neurons impaired self-heating behavior (C).

(D–I) Thermal gradient test. Mice failed to migrate to the thermoneutral position upon the inhibition of LH^{Vgat} neurons at both low (D–F) and high (G–I) ambient temperatures. Representative heat maps showing cumulative positions of example mice (D and G). Mean (E and H) and peak (F and I) positions.

(J–L) Nest-building test. Chemogenetic inhibition of LH^{Vgat} neurons impaired the nest-building behavior. Scheme (J). Traced outlines of nest-

building materials (K). Normalized size of the material after 90 min (1 = size at the session beginning) (L).
(M and N) Assessment of postural extension in a high ambient temperature (M, top). Representative photo of a mouse exhibiting postural extension (M, bottom). Cumulative duration of body extension during the session (N). Chemogenetic inhibition of LH^{Vgat} neurons impaired postural extension.
(O) Chemogenetic inhibition of LH^{Vgat} neurons did not affect BAT thermogenesis induced by environmental cold exposure.
Data are mean ± s.e.m. *P<0.05, **P<0.01, ***P<0.001, ****P<0.0001. Statistics in Table 2.
This figure is reprinted from (*172*).

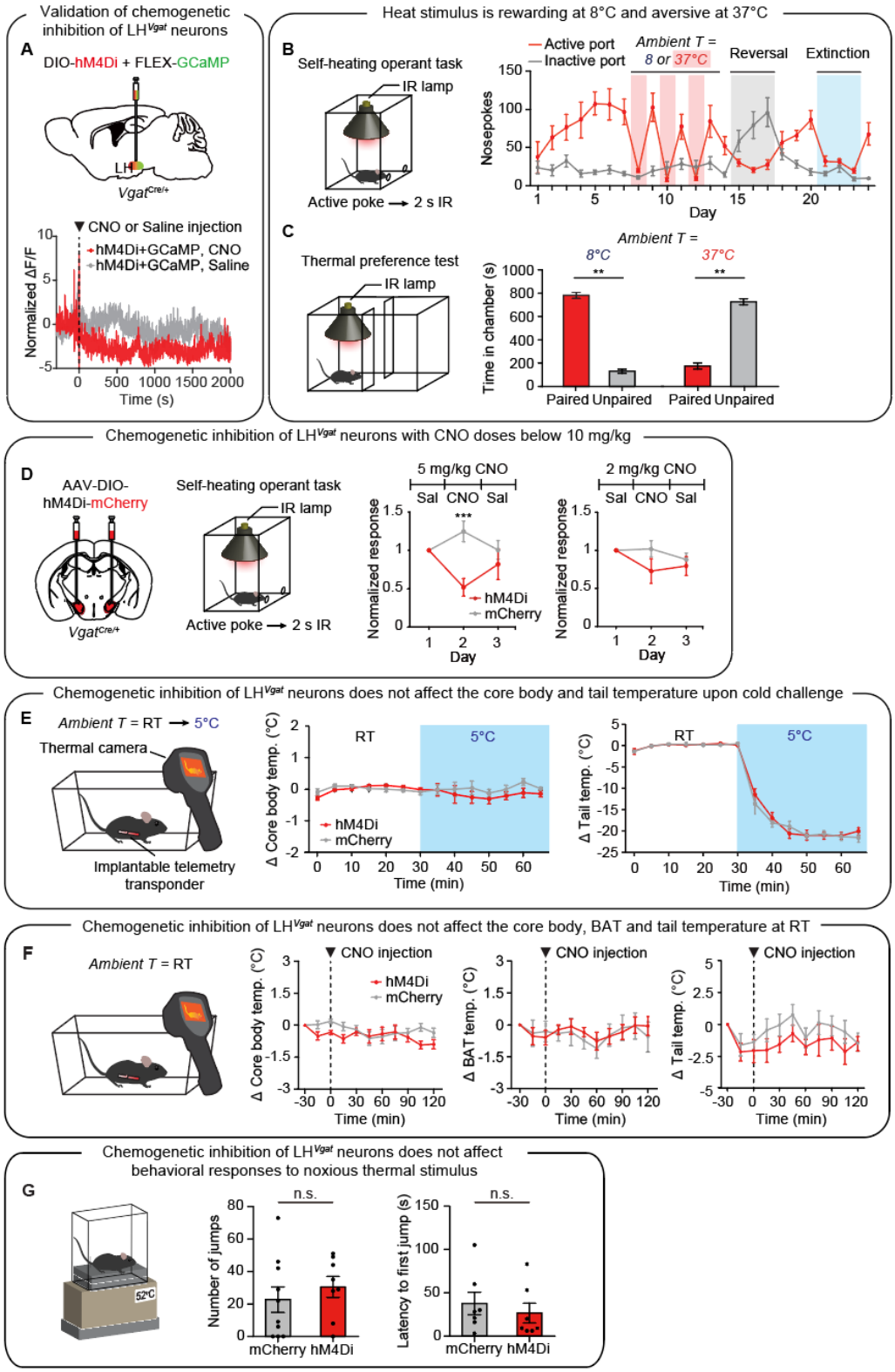

Figure 14. Characterization of behavioral assays, as well as thermal

stimulus and additional inhibition experiments on LH^{Vgat} neurons

(A) Validation of chemogenetic inhibition of LH^{Vgat} neurons. Top, scheme of simultaneous fiber photometry recording from and chemogenetic inhibition of LH^{Vgat} neurons. Bottom, example fiber photometry traces showing the decreased activity of LH^{Vgat} neurons upon the injection of CNO, but not saline, demonstrating the chemogenetic suppression of LH^{Vgat} neurons.

(B) Characterization of the self-heating operant task. Left, scheme. A nose poke in the active, but not the inactive port, turned on an IR heat lamp for 2 s. The duration of each session was 1 h. Right, naïve mice gradually learned to perform nose-poke responses for the heat stimulus at a cold ambient temperature (8° C; days 1-6). Following training, the nose-poke responses could be reversibly suppressed by increasing the ambient temperature to 37° C (days 7-13). Switching the active and inactive port, thereby pairing the heat stimulus with the previously inactive port, reversed the numbers of active and inactive nose pokes (days 15-17). This was reversed again by pairing the original active port again with the heat stimulus (days 18-20). When a nose poke was unpaired with the heat stimulus, mice ceased to perform nose-poke responses (days 21-23), which could be reversed by pairing the nose-poke responses to the heat stimulus again (day 24).

(C) Characterization of the IR thermal stimulus used in this study. Left, scheme of the thermal preference test. Mice freely explored two indistinguishable chambers. Entry into one of the chambers turned on the IR lamp for 2 s, every 4 s, providing enough heat without overheating. Right, mice preferred the heat-paired chamber at 8° C but avoided the heat-paired chamber at 37° C. Together, these results show that the IR heat stimulus is rewarding and reinforcing at a low ambient temperature but aversive at a high ambient temperature.

(D) Chemogenetic inhibition of LH^{Vgat} neurons with CNO doses below 10 mg/kg. A dose of 10 mg/kg was used in all other chemogenetic inhibition experiments throughout the study. Left, scheme of the chemogenetic inhibition of LH^{Vgat} neurons. Right, self-heating behavior was impaired upon the injection of 5 mg/kg, but not 2 mg/kg, CNO suggesting that the minimum dose required for the effect is 5 mg/kg.

(E and F) Chemogenetic inhibition of LH^{Vgat} neurons does not affect core body, BAT, and tail temperatures. Core body, BAT, and tail temperatures were measured using an implantable telemetry transponder and a thermal camera. Chemogenetic inhibition of LH^{Vgat} neurons did not affect the core body or tail temperatures upon exposure to a cold environment (E). This manipulation also did not alter the baseline temperatures of core body,

BAT, or tail at room temperature (F).
(G) Chemogenetic inhibition of LH^{Vgat} neurons does not affect behavioral responses to noxious thermal stimulus, as jumping behavior on a hot plate (52° C) was comparable for experimental and control groups.
Data are mean ± s.e.m. $^{**}P<0.01$, $^{***}P<0.001$; n.s., not significant. Statistics in Table 2.
This figure is reprinted from (*172*).

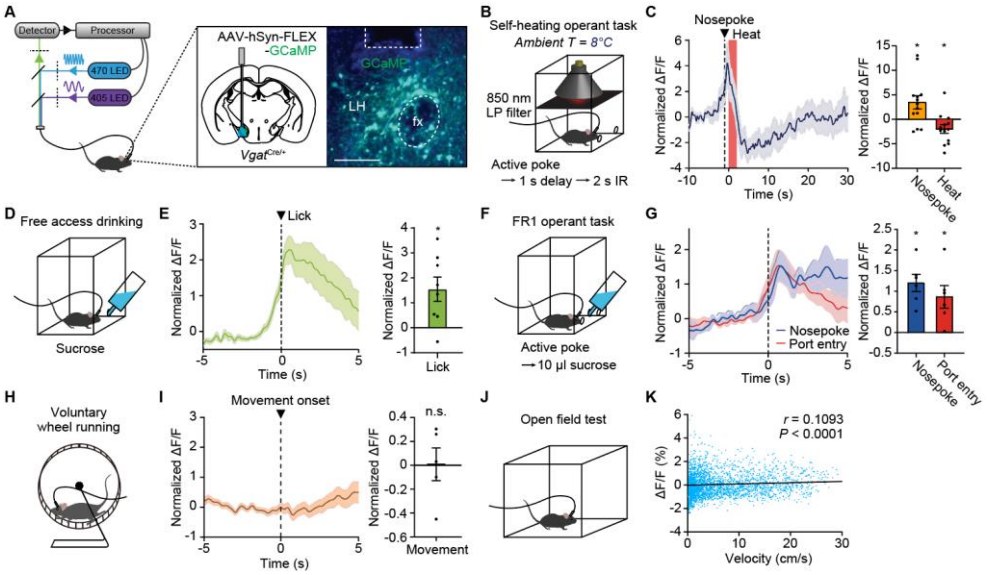

Figure 15. LH^{Vgat} neurons are excited during thermoregulatory behavior and inhibited by thermal reward

(A) Scheme of fiber photometry recordings from LH^{Vgat} neurons. Representative image showing GCaMP-expressing LH^{Vgat} neurons and optic fiber placement. Scale bar, 100 μm.

(B) Self-heating operant task protocol.

(C) Left, peri-event plot of average Ca^{2+} transients around the nose poke and heat delivery. LH^{Vgat} neurons were transiently activated by active nose poke and then inhibited by heat delivery at a cold ambient temperature (thermal reward; see Figures S1B and S1C). Right, average responses in the first 1 s following the active nose poke and the first 5 s following the heat offset.

(D) Food-deprived mice were allowed to freely drink sucrose solution.

(E) Left, LH^{Vgat} neurons were activated by caloric reward intake. Right, average responses in the first 5 s following drinking onset.

(F) Operant task for sucrose reward. Each active nose poke triggered the delivery of 10 μl sucrose solution to the reward port.

(G) Left, LH^{Vgat} neurons were activated by both the active nose poke and the consumption of sucrose reward. Right, average responses in the first 5 s of the responses.

(H) Voluntary wheel running assay.

(I) LH^{Vgat} neurons did not respond to the onset of the wheel movement.

(J) Open-field test.

(K) Ca^{2+} activity of LH^{Vgat} neurons exhibited only a weak correlation with the velocity of mice.

Data are mean ± s.e.m. $*P<0.05$; n.s., not significant. Statistics in Table 1.

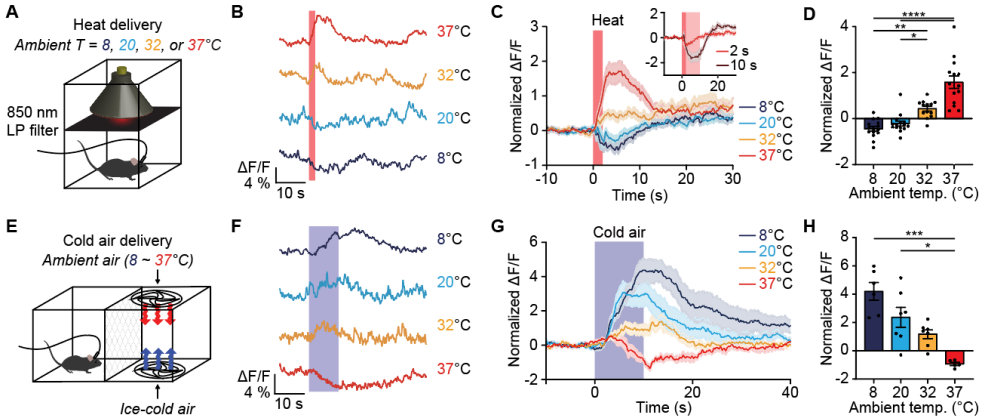

Figure 16. LH^{Vgat} neurons bidirectionally encode thermal punishment and reward

(A) Scheme of the IR heat delivery. Mice received 2-s heat stimuli at several different ambient temperatures, ranging from low (8° C) to high (37° C).

(B and C) Representative single-trial Ca^{2+} traces (B). Average responses (C). Inset, responses to 2-s and 10-s heat stimuli at 8° C. LH^{Vgat} neurons were inhibited or excited by heat delivery at 8° C (thermal reward) or 37° C (thermal punishment), respectively.

(D) Average responses in the first 5 s following IR offset.

(E) Scheme of the delivery of ambient air or ice-cold air. Mice received cold air for 10 s at different ambient temperatures in a custom-designed chamber.

(F and G) Representative single-trial Ca^{2+} traces (F). Average responses (G). LH^{Vgat} neurons were inhibited or excited by cold air at 37° C (thermal reward) or 8° C (thermal punishment), respectively.

(H) Average responses in the first 5 s following cold air offset.

Data are mean ± s.e.m. $*P < 0.05$, $**P < 0.01$, $****P < 0.0001$. Statistics in Table 2.

This figure is reprinted from (*172*).

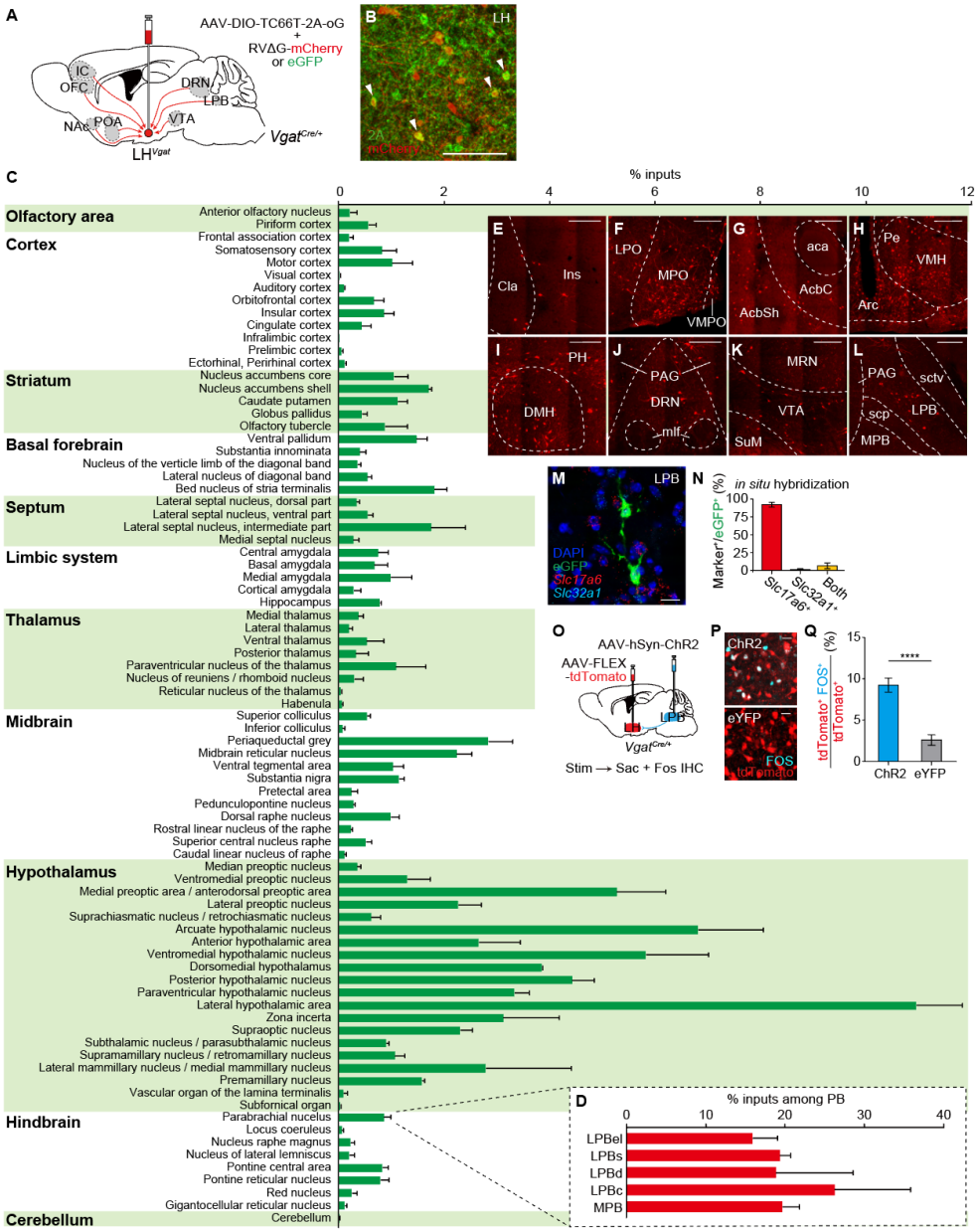

Figure 17. Whole-brain mapping of monosynaptic inputs to LH^{Vgat} neurons

(A) Rabies virus-mediated identification of monosynaptic inputs to LH^{Vgat} neurons.

(B) Representative confocal image of the injection site. Arrowheads indicate starter cells.

(C) Quantification of monosynaptic inputs of LH^{Vgat} neurons throughout the brain, shown as the percent of labeled neurons from a given region relative to total labeled neurons throughout the whole brain.

(D) Quantification of monosynaptic inputs within PB subregions. ~80% of labeled PB neurons were found in lateral subdivisions of the PB (together

referred to as the LPB here).
(E–L) Representative confocal images showing the labeled neurons in selected upstream regions.
(M and N) Representative confocal image of the LPB, showing the expression of eGFP (i.e., LPB neurons projecting to LH^{Vgat} neurons) and the fluorescence *in situ* hybridization detection of *Slc17a6* and *Slc32a1* genes (M). Quantification of the overlap (N). The majority of the LPB neurons projecting to LH^{Vgat} neurons were $Slc17a6^{+}$ (a marker of glutamatergic neurons).
(O–Q) Optogenetic stimulation of LPB–LH projections followed by Fos analysis. LH^{Vgat} neurons were labeled with tdTomato (O). Representative confocal images (P) and quantification (Q) of the overlap between Fos^{+} neurons and $tdTomato^{+}$ LH^{Vgat} neurons.
Scale bars, 100 μm (B and P), 200 μm (E–L), 20 μm (M).
Data are mean ± s.e.m. ****P<0.0001. Statistics in Table 2.
Definitions for the abbreviations are given in ‘Abbreviations’ in Methods.
This figure is reprinted from (*172*).

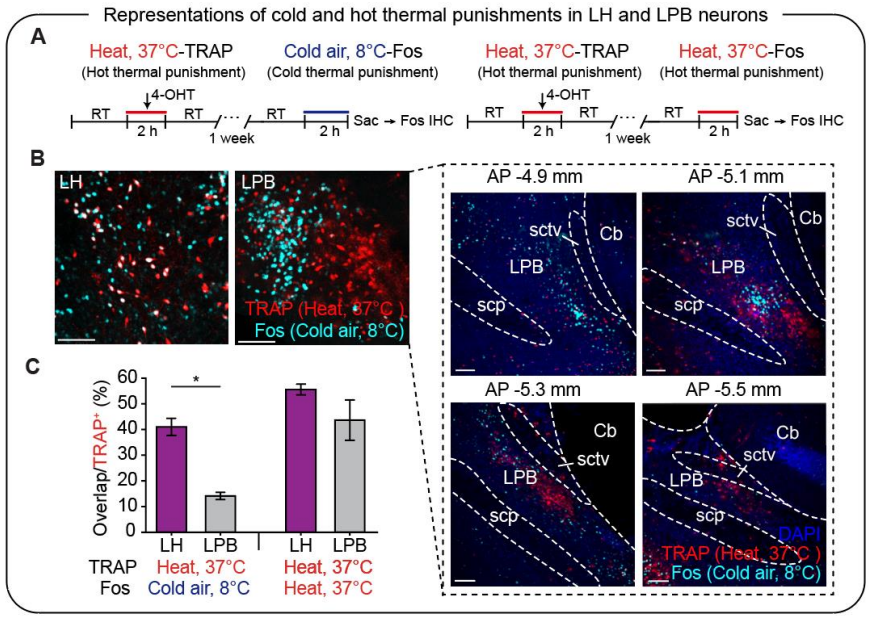

Figure 18. Representations of hot and cold thermal punishment stimuli in LH and LPB neurons

(A) I compared the representations of both hot and cold thermal punishments (i.e., two thermal stimuli that are distinct in temperature, but equivalent in valence) by LPB and LH neurons using a TRAP reporter mouse line (*Fos*$^{iCreER/+}$ mice crossed with Ai14 tdTomato reporter mice) (*170*, *171*) and immunohistochemistry against Fos, a neural activity marker. I used the TRAP reporter system to label neurons activated by IR heat stimuli at an ambient temperature of 37° C (Heat, 37° C–TRAP; hot thermal punishment) and Fos immunohistochemistry in the same mice to additionally visualize the neurons activated by ice–cold air at 8° C (Cold air, 8° C–Fos; cold thermal punishment) (left). For the control experiment, the same hot thermal punishment was used for both TRAP– and Fos–mediated labelings (right).

(B and C) Representative confocal images showing LH and LPB neurons activated by hot (TRAP, red) and cold (Fos, cyan) thermal punishments (B) and Quantification showing the overlap of TRAP– and Fos–labeled neurons in the LH and LPB (C). I found that the amount of overlap between neurons activated by hot and cold thermal punishments was significantly larger in the LH than in the LPB. The overlap of TRAP– and Fos–labeled neurons in the control experiment was comparable between the two regions. This result is in line with several previous studies employing single–unit recordings and Fos immunohistochemistry, which have shown the presence of separate warm– or cold–sensitive neurons in the LPB (*154*, *155*, *144*, *146*). I also observed that the neurons activated by hot and cold thermal punishments showed clear spatial segregation

within the LPB; the neurons labeled by hot thermal punishment were located in the mid-to-posterior and dorsolateral parts of the LPB, whereas those labeled by cold thermal punishment were located in the anterior and external lateral parts of the LPB. These findings match previously reported locations of warm- and cold-sensitive neurons in the LPB (*144–146*). Note that both of these LPB subregions provided direct inputs to LH^{Vgat} neurons (Figure 4D).

Scale bars, 100 μm. Data are mean ± s.e.m. $*P<0.05$. Statistics in Table 2.

This figure is reprinted from (*172*).

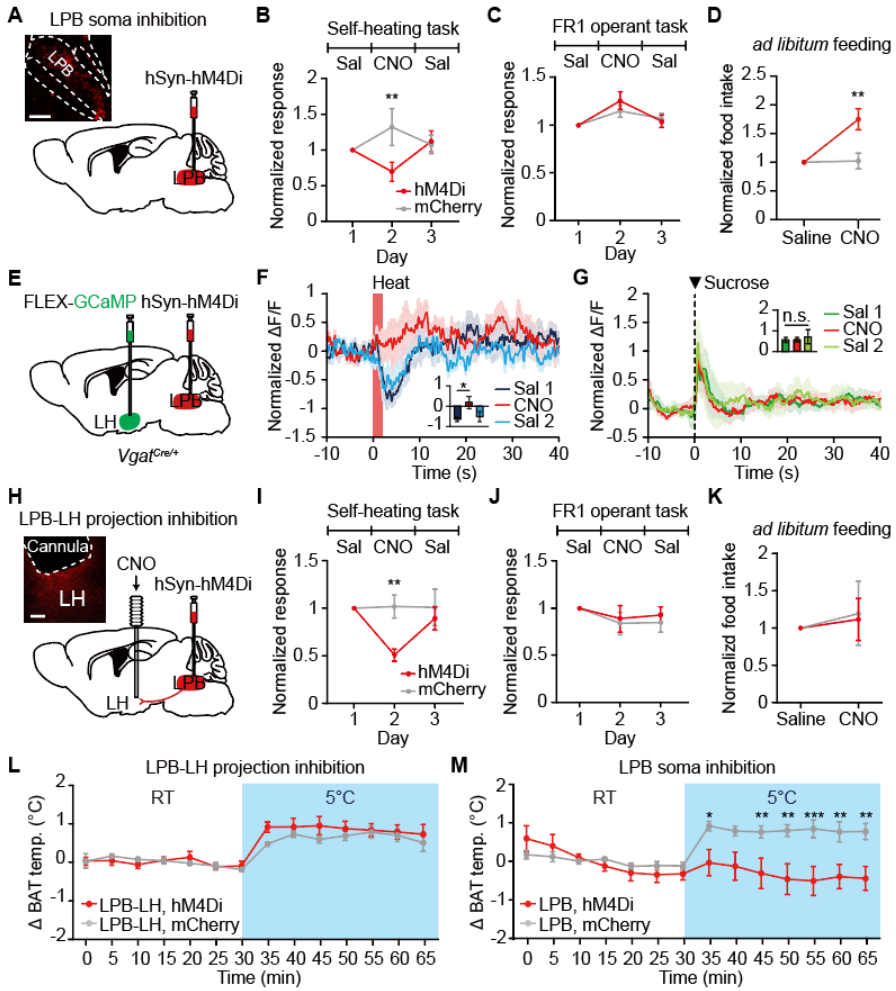

Figure 19. Parabrachial inputs are required for thermoregulatory behavior and the neural coding of thermal reward by LH^{Vgat} neurons

(A–D) Chemogenetic inhibition of LPB neurons (A) selectively impaired the self-heating operant task at a cold ambient temperature (8° C) (B) but did not affect the FR1 operant task for caloric reward (10 μl sucrose solution) in food-deprived mice (C) and increased *ad libitum* food intake in food-deprived mice (D).

(E) Simultaneous fiber photometry recording from LH^{Vgat} neurons and chemogenetic inhibition of LPB neurons.

(F and G) Chemogenetic inhibition of LPB neurons abolished the response of LH^{Vgat} neurons to thermal reward (IR heat stimulus at 8° C) (F) but did not affect the response to caloric reward (G). Insets, average responses in the first 5 s of the event. 'Sal 1' and 'Sal 2' indicate control data obtained from Day 1 and 3, respectively, when saline was administered. CNO was injected on Day 2.

(H–K) Chemogenetic inhibition of axon terminals of LPB neurons in the LH

(H) selectively impaired self-heating (I) without affecting the FR1 operant task for caloric reward (J) or *ad libitum* feeding (K). Scale bars, 200 μm.

(L and M) Chemogenetic inhibition of LPB-LH projections did not affect BAT thermogenesis induced by environmental cold exposure (L), but inhibition of LPB neurons impaired BAT thermogenesis (M).

Data are mean ± s.e.m. *P<0.05; **P<0.01, ***P<0.001. Statistics in Table 2.

This figure is reprinted from (*172*).

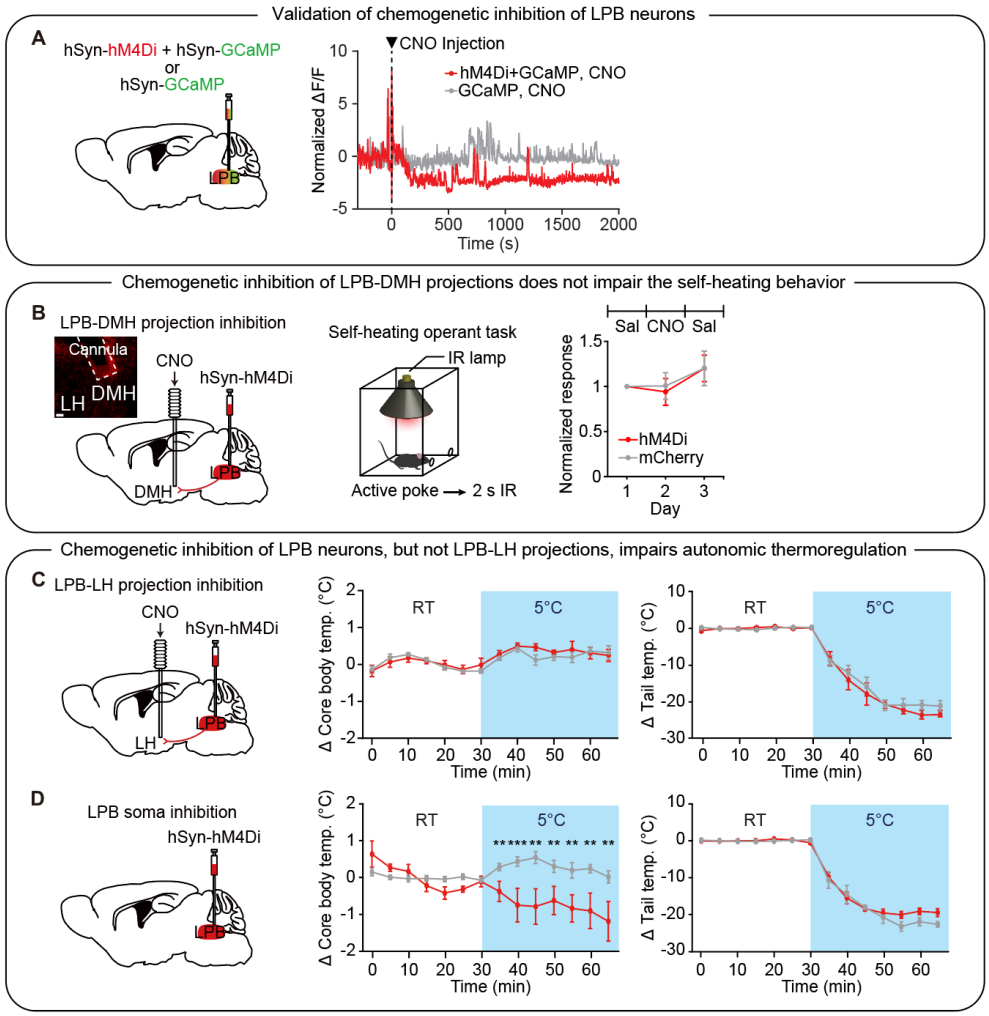

Figure 20. Additional chemogenetic inhibition experiments on parabrachial inputs

(A) Validation of the chemogenetic inhibition of LPB neurons. Left, scheme of simultaneous fiber photometry recording from and chemogenetic inhibition of LPB neurons. Right, example fiber photometry traces showing the decreased activity of an LPB neuron upon the injection of CNO into an hM4Di+GCaMP mouse, but not into a GCaMP-only control animal, demonstrating the chemogenetic suppression of LPB neurons.

(B) The effects of chemogenetic silencing of the axon terminals of LPB neurons in the LH (Figures 5H-5K) cannot be attributed to the silencing of LPB terminals in the adjacent DMH due to potential CNO leakage. Left, to control for the possibility that the observed effects might have been caused by the diffusion of CNO to the DMH, which is adjacent to the LH, I chemogenetically inhibited the axon terminals of LPB neurons in the DMH. Right, chemogenetic inhibition of the LPB-DMH projections did not impair

self-heating at a low ambient temperature (8° C). Scale bar, 100 μm.
(C and D) The LPB, but not the LPB-LH projection, is required for autonomic thermoregulation. Chemogenetic inhibition of axon terminals of LPB neurons in the LH (C, left) or the cell bodies of LPB neurons (D, left). Chemogenetic inhibition of LPB-LH projections did not disrupt mice from maintaining their core body temperature when mice were exposed to a cold environment (C, middle), but inhibition of LPB neurons did (D, middle). Chemogenetic inhibition of either LPB-LH projections (C, right) or LPB neurons (D, right) did not significantly affect the decrease in tail temperature, but upon exposure to a cold environment, a trend toward less decrease was observed when the LPB soma was inhibited (D, right).
Data are mean ± s.e.m. $^{**}P<0.01$, $^{***}P<0.001$. Statistics in Table 2.
This figure is reprinted from (*172*).

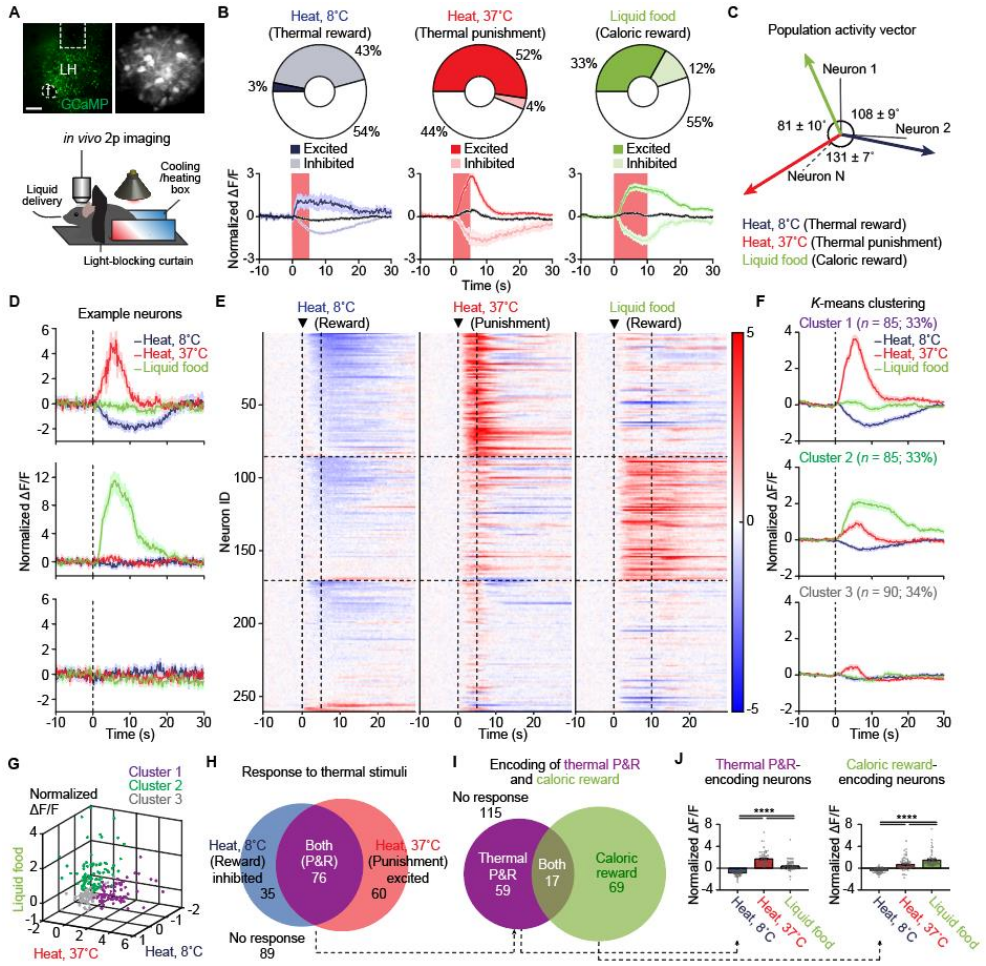

Figure 21. The LH^{Vgat} subpopulation encoding thermal punishment and reward is largely distinct from the caloric reward-encoding subpopulation

(A) Two-photon Ca^{2+} imaging of individual LH^{Vgat} neurons. Representative images of GCaMP-expressing LH^{Vgat} neurons acquired with confocal (top left) and two-photon (top right) microscopy. Mice were placed inside a custom-made thermal box for setting the ambient temperature, and brief heat stimuli could be delivered to mice using an IR heat lamp; liquid food could be delivered to the mouth (bottom). Scale bar, 200 μm.

(B) Top, proportions of neurons responsive to 5-s heat stimuli at 8° C (left, thermal reward), 5-s heat stimuli at 37° C (middle, thermal punishment), or 10-s liquid food delivery (right, caloric reward). Bottom, average Ca^{2+} traces from neurons that were excited, inhibited, or non-responsive to each respective stimulus.

(C) Population vector representations of the responses and their relative angles.

(D) Responses of three example neurons. Dotted lines indicate the stimulus onset.

(E) Responses of all neurons. Distinct activity groups emerged from K-means clustering (see Figure S4B). Dotted horizontal lines separate each cluster; dotted vertical lines indicate the onset and offset of each stimulus. Colors indicate normalized ΔF/F.
(F) Average responses within each cluster.
(G) Scatterplot showing average response amplitudes of all neurons, demonstrating the spatial separation of neural activity patterns.
(H) Distribution and overlap of LH^{Vgat} neurons significantly inhibited by thermal reward and those excited by thermal punishment.
(I) Distribution and overlap of LH^{Vgat} neurons encoding thermal P&R and caloric rewards.
(J) Average responses of the neurons encoding thermal P&R (left) and caloric reward (right) in the first 10 s following the stimulus onset.
Data are mean ± s.e.m. ****P<0.0001. Statistics in Table 2.
This figure is reprinted from (*172*).

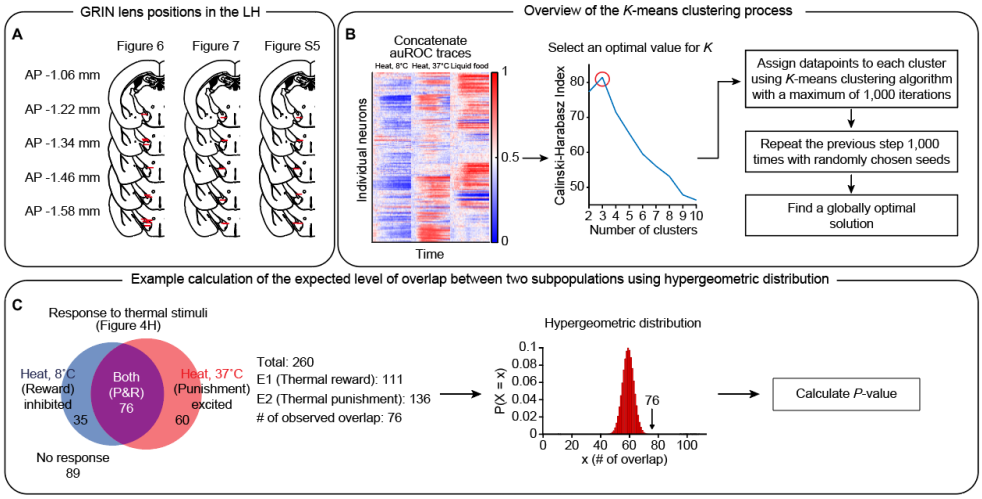

Figure 22. GRIN lens placement targeting the LH and graphical illustrations of clustering analysis and statistical testing of overlaps in neuronal populations

(A) Scheme of the GRIN lens placement targeting the LH. Red lines indicate the tips of the implanted lenses.

(B) To characterize the responses of individual LH^{Vgat} neurons, I used area under the receiver-operating characteristic (auROC) curve analyses followed by *K*-means clustering of neurons with similar activity patterns. This panel describes an overview of the *K*-means clustering process. Left, I calculated and concatenated the auROC values representing the responses of all neurons. Middle, the optimal value for *K* that returns the clustering result with the maximum value of the Calinski-Harabasz (CH) index was selected because a high CH index indicates high density within each cluster, as well as high cluster separability. Right, the final globally optimal solution for *K*-means clustering was found among the results from 1,000 replicates (see Methods).

(C) Example calculation of the expected level of overlap among neurons responsive to two different events using hypergeometric distribution (see Methods). Low *P* values indicate that the amount of overlap is significantly higher or lower than expected by chance.

This figure is reprinted from (*172*).

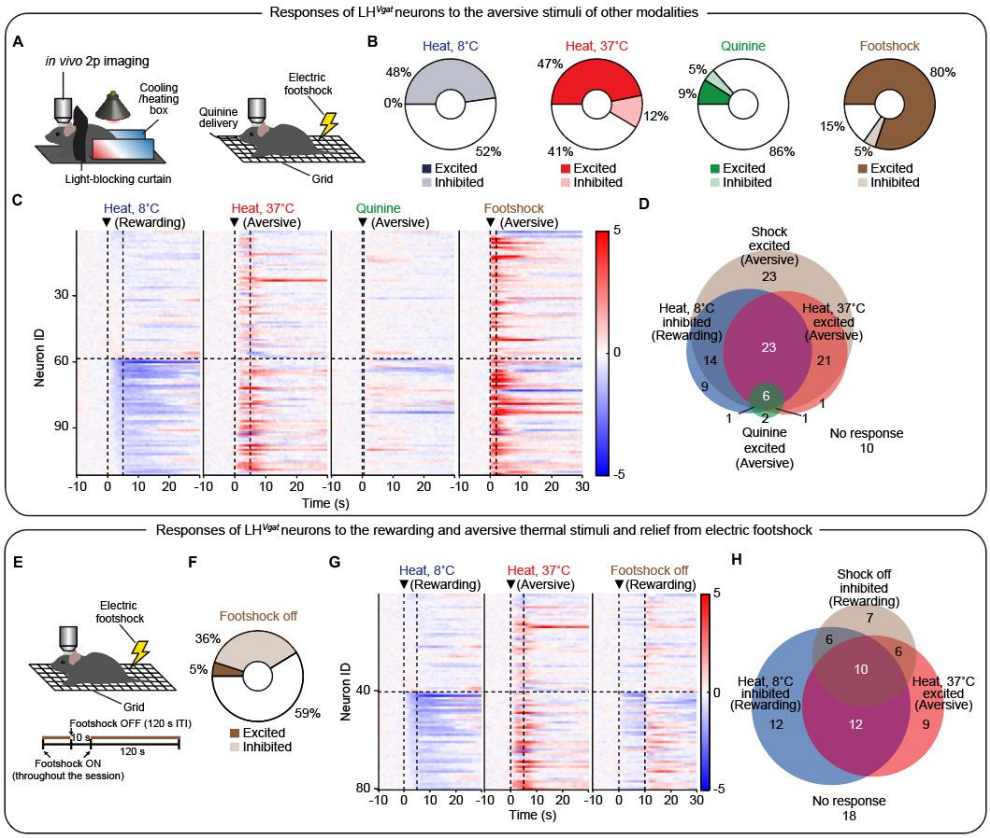

Figure 23. Responses of LH^{Vgat} neurons to various aversive and rewarding stimuli

(A) I additionally investigated the stimulus specificity of thermal P&R neurons by characterizing their responses to other aversive stimuli, including a bitter tastant, and electric foot shock. Scheme of two-photon Ca^{2+} imaging of LH^{Vgat} neurons. Left, to monitor the responses of individual LH^{Vgat} neurons to thermal stimuli, mice were placed inside a custom-made temperature-adjustable thermal box where IR heat could be delivered. Right, to monitor in separate experiments the responses of individual LH^{Vgat} neurons to electric foot shocks and a bitter tastant, mice were placed on a metal grid where electric foot shocks (0.4 mA) could be applied, and quinine solution (5 mM) could be orally delivered.

(B) Proportions of neurons responsive to 5-s heat stimuli at 8° C (thermal reward), 5-s heat stimuli at 37° C (thermal punishment), quinine solution delivery (10 μl over 0.5 s), or 2-s electric foot shocks.

(C) Responses of all neurons (n = 111 neurons from 8 mice) to the four stimuli. Neurons are grouped based on their responses to thermal reward. Dotted horizontal lines separate each group (top, no response; bottom, inhibited); dotted vertical lines indicate the onset and offset of each stimulus. Colors indicate normalized ΔF/F.

(D) Distribution and overlap of LH^{Vgat} neurons significantly inhibited by heat stimuli at 8° C (thermal reward), those excited by heat stimuli at 37° C (thermal punishment), those excited by electric foot shocks, and those excited by quinine solution delivery. Only a small subset of thermal P&R neurons was activated by oral delivery of a bitter tastant, despite its high concentration (5 mM quinine) (*173*). This result indicates that thermal P&R neurons are not generally activated by aversive stimuli. All thermal P&R neurons, however, were excited by electric foot shocks, which reflects that most of the imaged LH^{Vgat} neurons (80%) were activated by foot shocks.
(E) I additionally characterized the responses of thermal P&R neurons to a rewarding stimulus, i.e. relief from foot shock. Mice were placed on a metal grid that delivered continuously a mild electric foot shock (0.1 mA), ceasing for 10 s every trial (intertrial interval 120 s). I used weaker shock here since the shock intensity in the above experiment (0.4 mA) might have been overly strong.
(F) Proportions of the neurons responsive to the offsets of electric foot shocks.
(G) Responses of all neurons (n = 80 neurons from 6 mice) to aversive and rewarding thermal stimuli and to the offsets of electric foot shocks. Neurons are grouped based on their responses to rewarding thermal stimuli. Dotted horizontal lines separate each group (top, no response; bottom, inhibited). Dotted vertical lines indicate the onset and offset of each stimulus. Colors indicate normalized $\Delta F/F$.
(H) Distribution and overlap of LH^{Vgat} neurons significantly inhibited by heat stimuli at 8° C (rewarding thermal stimuli), those excited by heat stimuli at 37° C (aversive thermal stimuli), and those inhibited by the offsets of electric foot shocks. The amount of overlap between neurons inhibited by the offsets of electric foot shocks (brown) and neurons encoding thermal P&R (purple) did not significantly differ from that expected by chance.
Statistics in Table 2.
This figure is reprinted from (*172*).

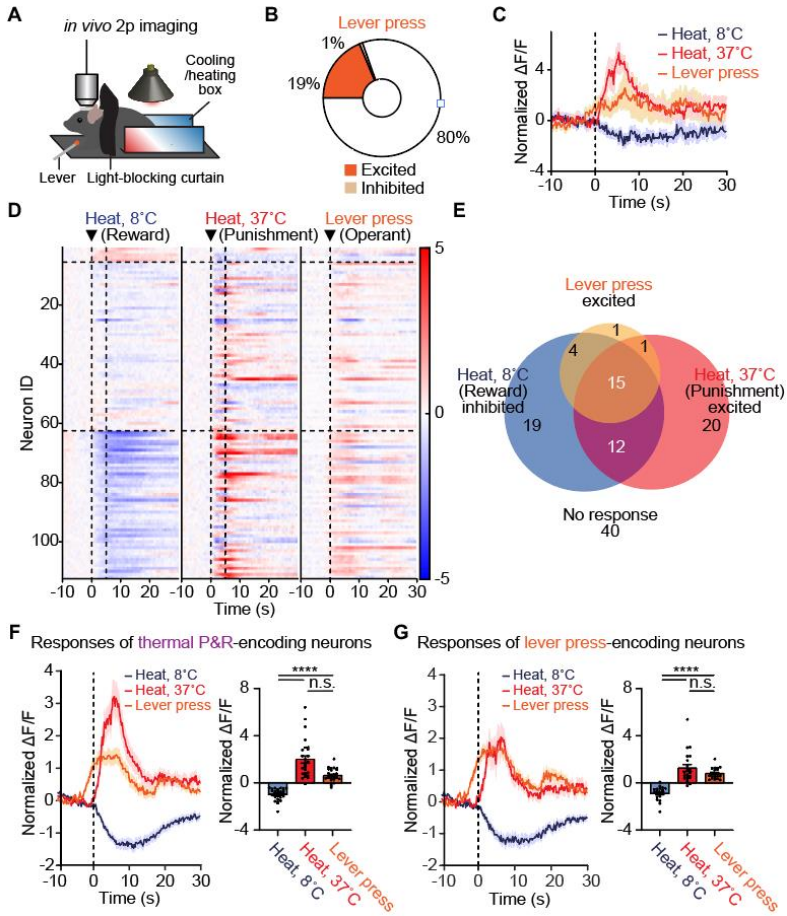

Figure 24. The LH^{Vgat} subpopulation bidirectionally encoding thermal punishment and reward is engaged during thermoregulatory behavior

(A) Two-photon Ca^{2+} imaging of individual LH^{Vgat} neurons. Mice were trained to press a lever for the 1-s heat delivery at 8° C following a 2-s delay.

(B) Proportions of neurons responsive to lever presses.

(C) Responses of an example neuron to a 5-s heat stimulus at 8° C (thermal reward), a 5-s heat stimulus at 37° C (thermal punishment), or a lever press (operant responding for thermal reward). The dotted line indicates the onset of events.

(D) Responses of all neurons. Neurons are grouped based on their responses to heat stimuli at 8° C. Dotted horizontal lines separate each group (top, activated; middle, no response; bottom, inhibited); dotted vertical lines indicate the onset and offset of the events. Colors indicate normalized ⊿F/F.

(E) Distribution and overlap of LH^{Vgat} neurons significantly inhibited by thermal reward, those excited by thermal punishment, and those excited by lever presses.

(F and G) Peri-event plot of average responses of thermal P&R-encoding neurons (F) and lever press-encoding neurons (G) upon heat stimuli and lever presses (left) and average responses of the neurons in the first 10 s following the onset of these events (right). Dotted lines indicate the onset of the events.
Data are mean ± s.e.m. ****P<0.0001; n.s., not significant. Statistics in Table 2.
This figure is reprinted from (*172*).

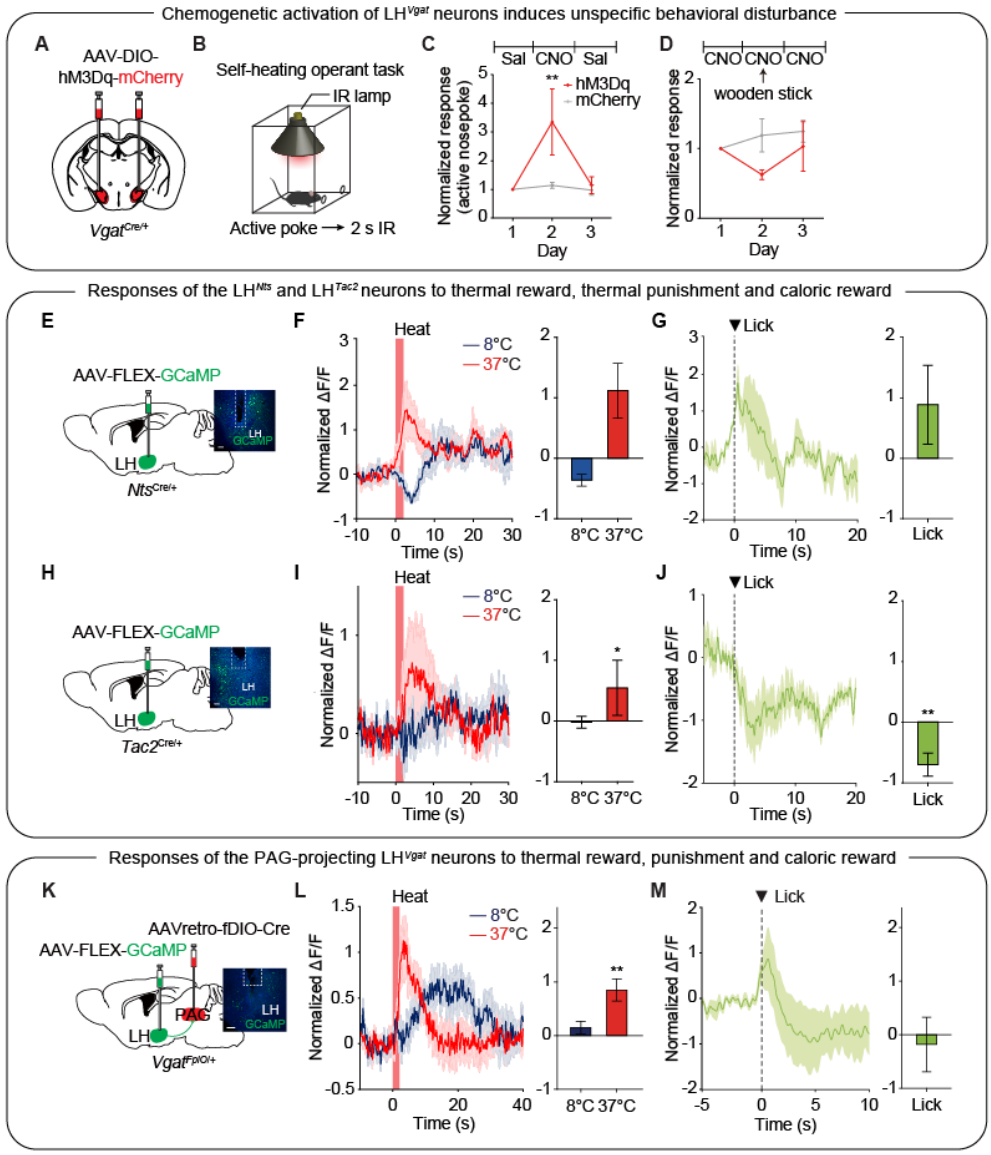

Figure 25. Chemogenetic activation of LH^{Vgat} neurons and fiber photometry recordings from subpopulations of LH^{Vgat} neurons

(A–D) Chemogenetic activation of LH^{Vgat} neurons induces gnawing behavior. Scheme of the chemogenetic activation (A). Scheme of the self–heating operant task (B). Chemogenetic activation of LH^{Vgat} neurons increased active nose–poke responses due to gnawing on the nose–poke port in most animals (C), indicating a nonspecific increase in nose–poke responses rather than facilitation of thermoregulatory behavior. This was further confirmed by the experiment in (D), in which introducing a wooden stick as gnawing material during chemogenetic stimulation elicited a trend toward decreased normalized responses. Previous studies have also reported that the activation of LH^{Vgat} neurons elicits gnawing behavior

(*139*, *147*).
(E) Fiber photometry recordings from LH^{Nts} neurons, a known subpopulation of LH^{Vgat} neurons (*117*, *129*).
(F and G) LH^{Nts} neurons were inhibited or excited by heat delivery at 8 or 37° C, respectively (F), as well as excited by liquid food intake (G). The response profile appears to be similar to that of LH^{Vgat} neurons. The responses of LH^{Nts} neurons were not selective to either the thermal or caloric stimulus.
(H) Fiber photometry recordings from LH^{Tac2} neurons, another known subpopulation of LH^{Vgat} neurons (*129*).
(I and J) LH^{Tac2} neurons were excited by heat delivery at 37° C, not responsive to heat delivery at 8° C (E), and inhibited by liquid food intake (I). The response profile is distinct from that of LH^{Vgat} neurons. The responses of LH^{Tac2} neurons were not selective to either the thermal or caloric stimulus.
(K) Based on the previous finding that the activation of PAG-projecting LH^{Vgat} neurons does not increase feeding behavior (*124*) (contrary to the activation of the entire LH^{Vgat} population), I considered that PAG-projecting LH^{Vgat} neurons may selectively encode thermal, but not caloric, stimuli. To test this possibility, I expressed GCaMP in PAG-projecting LH^{Vgat} neurons and recorded the Ca^{2+} dynamics of this subpopulation using fiber photometry.
(L and M) PAG-projecting LH^{Vgat} neurons were excited by thermal punishment but the responses to thermal (L) and caloric (M) rewards were not significant, which implies that these neurons do not represent the thermal P&R subpopulation that bidirectionally encodes thermal punishment and reward. Scale bars, 200 μm.
Data are mean ± s.e.m. *P<0.05, **P<0.01. Statistics in Table 2.
This figure is reprinted from (*172*).

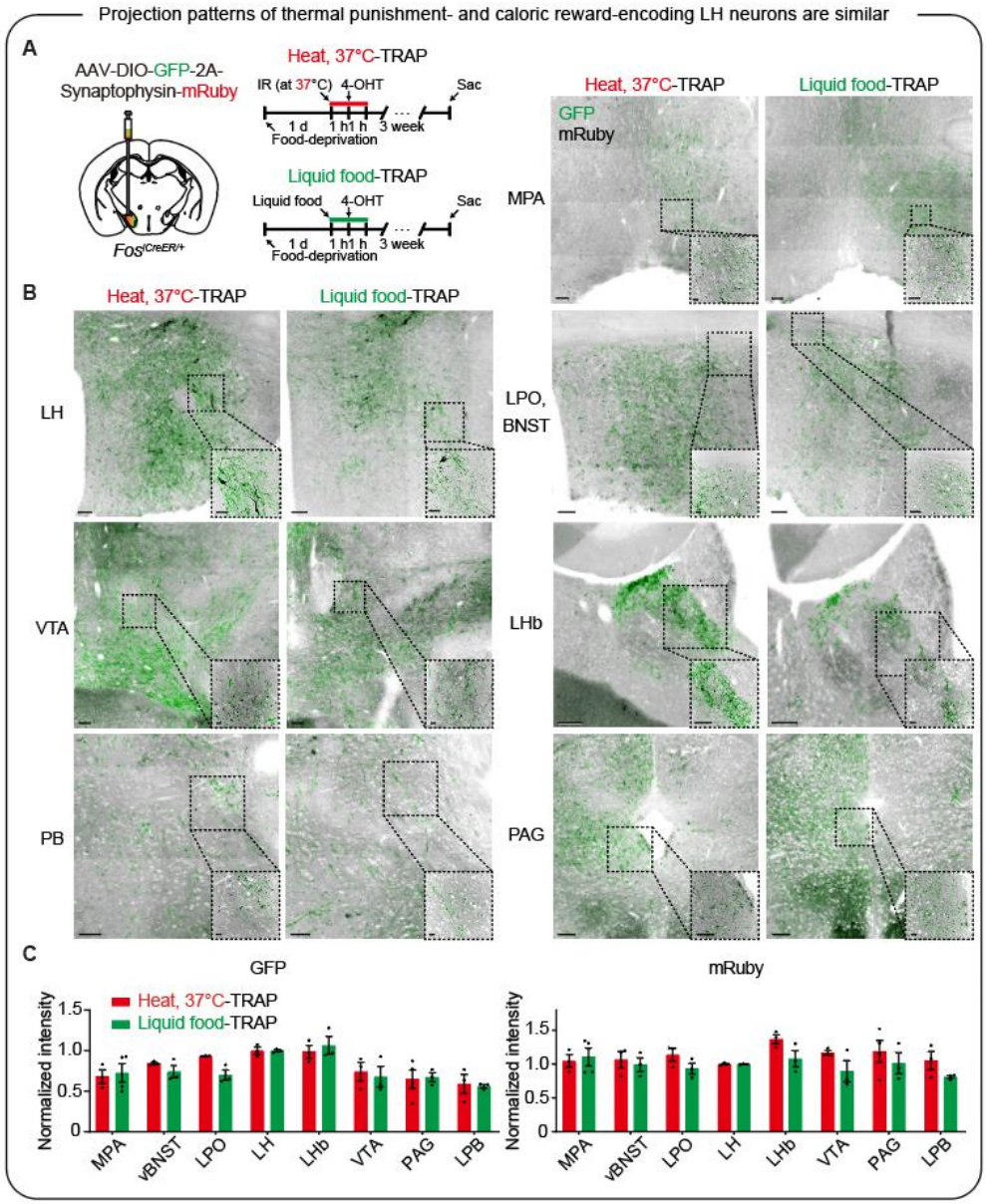

Figure 26. Projection patterns of thermal punishment− and caloric reward−encoding LH neurons are similar

(A) I sought to identify a downstream that is selectively innervated by thermal P&R−encoding neurons, but not by caloric reward−activated neurons, using a TRAP mouse line (*Fos*$^{iCreER/+}$ mice). If successfully identified, this would allow us to specifically target and manipulate the thermal P&R−encoding LH^{Vgat} subpopulation by injecting retrograde AAV viral vectors to the downstream area (*174*). However, while thermal P&R neurons cannot be defined by a simple excitatory response to a single stimulus, the TRAP technique allows the targeting of only those neurons that are activated upon a single stimulus. As such, I targeted the LH

neurons that are activated upon thermal punishment as a proxy for thermal P&R neurons—it is important to note that the targeted neurons may also include non-*Vgat*-expressing neurons, and that the thermal P&R neurons belong to, but cannot be equated to, the subset of LH^{Vgat} neurons excited by thermal punishment (Figure 6H). To TRAP-label the LH neurons that are activated by thermal punishment or caloric reward and visualize their axon terminals, I injected Cre-inducible AAVs carrying mRuby-tagged synaptophysin into the LH of $Fos^{iCreER/+}$ mice (left). The mice were then divided into two groups (n = 3 mice per group) and exposed to thermal punishment (2-s IR heat delivery at 37° C ambient temperature every 1 min for 2 hrs) or allowed to consume liquid food for 2 hrs following one-day food deprivation.

(B and C) Representative confocal images (B) and quantifications (C) of the axon terminals of the LH neurons activated by thermal punishment or caloric reward. Note that the projection targets of thermal punishment- and caloric reward-activated LH neurons are comparable to each other. Despite the aforementioned limitations of the experimental design, this result suggest that other strategies might be required to gain specific access to thermal P&R-encoding LH^{Vgat} neurons. Scale bars, 100 μm (B), 20 μm (B, insets).

Data are mean ± s.e.m. Statistics in Table 2.

This figure is reprinted from (*172*).

Table 2. Statistical analysis

Figure	Sample Size (numbers indicate mice unless otherwise stated)	Statistical Test	Values
13C	5 (hM4Di) 7 (mCherry)	Two-way repeated-measures ANOVA factor one: drug factor two: group post-hoc correction for multiple comparisons (Bonferroni)	Interaction: P = 0.0209 Drug: P < 0.0001 Group: P = 0.0642 F (2, 18) = 4.832 F (2, 18) = 22.66 F (1, 9) = 4.445 Day 1: P > 0.9999 Day 2: P = 0.0030 Day 3: P > 0.9999
13E	8 (hM4Di) 6 (mCherry)	Wilcoxon rank-sum test (two-tailed)	P = 0.0426
13F	8 (hM4Di) 6 (mCherry)	Wilcoxon rank-sum test (two-tailed)	P = 0.0216
13H	16 (hM4Di) 13 (mCherry)	Wilcoxon rank-sum test (two-tailed)	P = 0.0334
13I	16 (hM4Di) 13 (mCherry)	Wilcoxon rank-sum test (two-tailed)	P = 0.0162
13L	5 (hM4Di) 6 (mCherry)	Wilcoxon rank-sum test (two-tailed)	P = 0.0087
13N	6 (hM4Di) 7 (mCherry)	Two-way repeated-measures ANOVA factor one: group factor two: time post-hoc correction for multiple comparisons (Bonferroni)	Interaction: P < 0.0001 Time: P < 0.0001 Group: P = 0.0002 F (3, 33) = 23.45 F (3, 33) = 112.52 F (1, 33) = 28.21 10 min: P > 0.9999 20 min: P = 0.0375 30 min: P < 0.0001 40 min: P < 0.0001
13O	7 (hM4Di) 5 (mCherry)	Two-way repeated-measures ANOVA factor one: group factor two: time	Interaction: P = 0.5350 Time: P < 0.0001 Group: P = 0.4783
14C	5 (8˚C) 5 (37˚C)	Paired t-test	8˚C: P < 0.0001 37˚C: P = 0.0004
14D (5 mg/kg)	9 (hM4Di) 7 (mCherry)	Two-way repeated-measures ANOVA factor one: drug factor two: group post-hoc correction for multiple comparisons (Bonferroni)	Interaction: P = 0.1342 Drug: P = 0.0562 Group: P = 0.0694 F (2, 28) = 0.1342 F (2, 28) = 0.0562 F (1, 14) = 0.0694 Day 1: P > 0.9999 Day 2: P = 0.0282 Day 3: P = 0.8230
14D (2 mg/kg)	10 (hM4Di) 8 (mCherry)	Two-way repeated-measures ANOVA factor one: drug factor two: group post-hoc correction for multiple comparisons (Bonferroni)	Interaction: P = 0.0139 Drug: P = 0.5991 Group: P = 0.0044 F (2, 32) = 4.898 F (2, 32) = 0.5207 F (1, 16) = 10.97 Day 1: P > 0.9999 Day 2: P = 0.0002

			Day 3: P = 0.6161
14E (Core body temperature)	8 (hM4Di) 7 (mCherry)	Two-way repeated-measures ANOVA factor one: drug factor two: group	Interaction: P = 0.5465 Time: P = 0.2556 Group: P = 0.3298 Interaction: F (13,169) = 0.9076 Drug: F (2.675,34.77) = 1.417 Group: F (13,169) = 1.025
14E (Tail temperature)	6 (hM4Di) 5 (mCherry)	Two-way repeated-measures ANOVA factor one: drug factor two: group	Interaction: P = 0.6083 Time: P < 0.0001 Group: P = 0.1805 Interaction: F (13,143) = 0.8436 Drug: F (13,143) = 221.9 Group: F (1,11) = 2.044
14F (Core body temperature)	8 (hM4Di) 10 (mCherry)	Two-way repeated-measures ANOVA Factor one: Time Factor two: Group post-hoc correction for multiple comparisons (Bonferroni)	Interaction: P = 0.1070 Time: P = 0.0175 Group: P = 0.2815 Interaction: F (10, 160) = 1.614 Time: F (10, 160) = 2.249 Group: F (1, 16) = 1.242 -30 min: P > 0.9999 -15 min: P > 0.9999 0 min: P > 0.9999 15 min: P > 0.9999 30 min: P > 0.9999 45 min: P > 0.9999 60 min: P > 0.9999 75 min: P > 0.9999 90 min: P > 0.9999 105 min: P = 0.2128 120 min: P > 0.9999
14F (BAT temeprature)	8 (hM4Di) 11 (mCherry)	Two-way repeated-measures ANOVA Factor one: Time Factor two: Group post-hoc correction for multiple comparisons (Bonferroni)	Interaction: P = 0.9997 Time: P = 0.0579 Group: P = 0.7927 Interaction: F (10, 170) = 0.1081 Time: F (10, 170) = 1.835 Group: F (1, 17) = 0.07127 -30 min: P > 0.9999 -15 min: P > 0.9999 0 min: P > 0.9999 15 min: P > 0.9999 30 min: P > 0.9999 45 min: P > 0.9999 60 min: P > 0.9999 75 min: P > 0.9999 90 min: P > 0.9999 105 min: P > 0.9999 120 min: P > 0.9999
14F (Tail temperature)	8 (hM4Di) 11 (mCherry)	Two-way repeated-measures ANOVA Factor one: Time Factor two: Group post-hoc correction for multiple comparisons	Interaction: P = 0.7313 Time: P = 0.0009 Group: P = 0.3118 Interaction: F (10, 170) = 0.6919 Time: F (10, 170) = 3.185 Group: F (1, 17) = 1.087

		(Bonferroni)	-30 min: P > 0.9999 -15 min: P > 0.9999 0 min: P > 0.9999 15 min: P > 0.9999 30 min: P > 0.9999 45 min: P > 0.9999 60 min: P > 0.9999 75 min: P > 0.9999 90 min: P > 0.9999 105 min: P > 0.9999 120 min: P > 0.9999
14G (left)	8 (hM4Di) 10 (mCherry)	Wilcoxon rank-sum test (two-tailed)	P = 0.3449
14G (right)	7 (hM4Di) 7 (mCherry)	Wilcoxon rank-sum test (two-tailed)	P = 0.3660
15C	13 (Nosepoke) 13 (Heat)	Wilcoxon rank-sum test (two-tailed)	P = 0.0215 (Nosepoke) P = 0.0327 (Heat)
15E	8	Wilcoxon signed rank test (two-tailed)	P = 0.0391
15G	6 (Nosepoke) 6 (Port entry)	Wilcoxon signed rank test (two-tailed)	P = 0.0313 (Nosepoke) P = 0.0313 (Port entry)
15I	5	Wilcoxon signed rank test (two-tailed)	P = 1
15K	6	Pearson correlation	r = 0.1093 P < 0.0001
16D	15 (8˚C) 15 (20˚C) 13 (32˚C) 14 (37˚C)	Kruskal-Wallis test post-hoc correction for multiple comparisons (Dunn's)	P < 0.0001 8˚C vs. 20˚C: P > 0.9999 8˚C vs. 32˚C: P = 0.0018 8˚C vs. 37˚C: P < 0.0001 20˚C vs. 32˚C: P = 0.0441 20˚C vs. 37˚C: P < 0.0001 32˚C vs. 37˚C: P = 0.3582
16D; Baseline vs. Response time window	15 (8˚C) 15 (20˚C) 13 (32˚C) 14 (37˚C)	Wilcoxon signed rank test (two-tailed)	8˚C: P < 0.0001 20˚C: P < 0.0001 32˚C: P < 0.0001 37˚C: P < 0.0001
16H	6 (8˚C) 7 (20˚C) 7 (32˚C) 5 (37˚C)	Kruskal-Wallis test post-hoc correction for multiple comparisons (Dunn's)	P = 0.0008 8˚C vs. 20˚C: P > 0.9999 8˚C vs. 32˚C: P = 0.1444 8˚C vs. 37˚C: P = 0.0004 20˚C vs. 32˚C: P > 0.9999 20˚C vs. 37˚C: P = 0.0290 32˚C vs. 37˚C: P = 0.3027
16H; Baseline vs. Response time window	6 (8˚C) 7 (20˚C) 7 (32˚C) 5 (37˚C)	Wilcoxon signed rank test (two-tailed)	8˚C: P = 0.0022 20˚C: P = 0.0169 32˚C: P = 0.0169 37˚C: P = 0.0079
17C	3		
17D	3	Kruskal-Wallis test	P = 0.8526
17N	3	Kruskal-Wallis test	P = 0.0464
17N	Slc17a6 (92.10%) Slc32a1 (1.28%) Both (6.62%)		
17Q	25 sections (ChR2) 24 sections (eYFP)	Wilcoxon rank-sum test (two-tailed)	P < 0.0001
18C (left)	4 (LPB) 3 (LH)	Wilcoxon rank-sum test (two-tailed)	P = 0.0286

18C (right)	3 (LPB) 3 (LH)	Wilcoxon rank-sum test (two-tailed)	P = 0.0700
19B	11 (hM4Di) 9 (mCherry)	Two-way repeated-measures ANOVA factor one: drug factor two: group post-hoc correction for multiple comparisons (Bonferroni)	Interaction: P = 0.0199 Drug: P = 0.6881 Group: P = 0.1860 F (2, 32) = 4.438 F (2, 32) = 0.3782 F (1, 16) = 1.909 Day 1: P > 0.9999 Day 2: P = 0.0097 Day 3: P > 0.9999
19C	6 (hM4Di) 7 (mCherry)	Two-way repeated-measures ANOVA factor one: drug factor two: group post-hoc correction for multiple comparisons (Bonferroni)	Interaction: P = 0.2821 Drug: P = 0.0006 Group: P = 0.6535 F (2, 22) = 1.341 F (2, 22) = 10.51 F (1, 22) = 0.2129 Day 1: P > 0.9999 Day 2: P = 0.5050 Day 3: P > 0.9999
19D	26 (hM4Di) 10 (mCherry)	Two-way repeated-measures ANOVA factor one: drug factor two: group post-hoc correction for multiple comparisons (Bonferroni)	Interaction: P = 0.0242 Drug: P = 0.0171 Group: P = 0.0242 Interaction: F (1,34) = 5.568 Drug: F (1,34) = 6.293 Group: F (1,34) = 5.568 Saline: P > 0.9999 CNO: P = 0.0028
19F (inset)	5	Friedman test post-hoc correction for multiple comparisons (Dunn)	P = 0.0239 X2(2) = 7.600 Day 1 vs. Day 2: P = 0.0342 Day 1 vs. Day 3: P > 0.9999 Day 2 vs. Day 3: P = 0.0806
19G (inset)	4	Friedman test post-hoc correction for multiple comparisons (Dunn)	P = 0.9306 X2(2) = 0.500 Day 1 vs. Day 2: P > 0.9999 Day 1 vs. Day 3: P > 0.9999 Day 2 vs. Day 3: P > 0.9999
19I	13 (hM4Di) 10 (mCherry)	Two-way repeated-measures ANOVA factor one: time factor two: group post-hoc correction for multiple comparisons (Bonferroni)	Interaction: P = 0.0327 Drug: P = 0.0495 Group: P = 0.0390 Interaction: F (2,36) = 3.768 Drug: F (2,36) = 3.271 Group: F (1,18) = 4.959 Day 1: P > 0.9999 Day 2: P = 0.0030 Day 3: P > 0.9999
19J	6 (hM4Di) 7 (mCherry)	Two-way repeated-measures ANOVA factor one: time factor two: group post-hoc correction for multiple comparisons (Bonferroni)	Interaction: P = 0.8733 Drug: P = 0.2298 Group: P = 0.6207 F (2, 22) = 0.1363 F (2, 22) = 1.573 F (1, 22) = 0.2592 Day 1: P > 0.9999 Day 2: P > 0.9999 Day 3: P > 0.9999
19K	6 (hM4Di) 6 (mCherry)	Two-way repeated-measures ANOVA factor one: drug	Interaction: P = 0.8737 Drug: P = 0.5622 Group: P = 0.8737

		factor two: group post-hoc correction for multiple comparisons (Bonferroni)	Interaction: F (1,10) = 0.0266 Drug: F (1,10) = 0.3593 Group: F (1,10) = 0.0266 Saline: P > 0.9999 CNO: P > 0.9999
19L	6 (hM4Di) 6 (mCherry)	Two-way repeated-measures ANOVA Factor one: Time Factor two: Group post-hoc correction for multiple comparisons (Bonferroni)	Interaction: P = 0.6226 Time: P < 0.0001 Group: P = 0.3084 Interaction: F (13, 130) = 0.8349 Time: F (3.456, 34.56) = 19.58 Group: F (1, 10) = 1.152 0 min: P > 0.9999 5 min: P = 0.9996 10 min: P = 9794 15 min: P > 0.9999 20 min: P = 0.9983 25 min: P > 0.9999 30 min: P > 0.9999 35 min: P = 0.2370 40 min: P = 0.9998 45 min: P = 0.9559 50 min: P = 0.9998 55 min: P > 0.9999 60 min: P > 0.9999 65 min: P > 0.9999
19M	6 (hM4Di) 6 (mCherry)	Two-way repeated-measures ANOVA Factor one: Time Factor two: Group post-hoc correction for multiple comparisons (Bonferroni)	Interaction: P < 0.0001 Time: P = 0.0012 Group: P = 0.0102 Interaction: F (13, 130) = 5.717 Time: F (13, 130) = 2.856 Group: F (1, 10) = 9.971 0 min: P = 0.9347 5 min: P = 0.9984 10 min: P > 0.9999 15 min: P > 0.9999 20 min: P > 0.9999 25 min: P = 0.9998 30 min: P > 0.9999 35 min: P = 0.0345 40 min: P = 0.0502 45 min: P = 0.0099 50 min: P = 0.0011 55 min: P = 0.0003 60 min: P = 0.0034 65 min: P = 0.0017
20B	8 (hM4Di) 9 (mCherry)	Two-way repeated-measures ANOVA factor one: drug factor two: group post-hoc correction for multiple comparisons (Bonferroni)	Interaction: P = 0.9506 Drug: P = 0.1296 Group: P = 0.8601 F (2, 30) = 0.0508 F (2, 30) = 2.189 F (1, 15) = 0.0321 Day 1: P > 0.9999 Day 2: P > 0.9999 Day 3: P > 0.9999
20C (Core body	5 (hM4Di) 6 (mCherry)	Two-way repeated-measures ANOVA	Interaction: P = 0.7544 Time: P < 0.0005

temperature)		Factor one: Time Factor two: Group post-hoc correction for multiple comparisons (Bonferroni)	Group: P = 0.4616 Interaction: F (13, 117) = 0.7058 Time: F (4.140,37.26) = 6.324 Group: F (1, 9) = 0.5914 0 min: P > 0.9999 5 min: P > 0.9999 10 min: P > 0.9999 15 min: P > 0.9999 20 min: P > 0.9999 25 min: P > 0.9999 30 min: P > 0.9999 35 min: P > 0.9999 40 min: P > 0.9999 45 min: P = 0.9793 50 min: P > 0.9999 55 min: P > 0.9999 60 min: P > 0.9999 65 min: P > 0.9999
20C (Tail temperature)	6 (hM4Di) 6 (mCherry)	Two-way repeated-measures ANOVA Factor one: Time Factor two: Group post-hoc correction for multiple comparisons (Bonferroni)	Interaction: P = 0.3779 Time: P < 0.0001 Group: P = 0.2228 Interaction: F (13, 130) = 1.085 Time: F (13, 130) = 215.1 Group: F (1, 10) = 1.690 0 min: P > 0.9999 5 min: P > 0.9999 10 min: P > 0.9999 15 min: P > 0.9999 20 min: P > 0.9999 25 min: P > 0.9999 30 min: P > 0.9999 35 min: P > 0.9999 40 min: P > 0.9999 45 min: P > 0.9999 50 min: P > 0.9999 55 min: P > 0.9999 60 min: P > 0.9999 65 min: P = 0.5434
20D (Core body temperature)	6 (hM4Di) 6 (mCherry)	Two-way repeated-measures ANOVA Factor one: Time Factor two: Group post-hoc correction for multiple comparisons (Bonferroni)	Interaction: P < 0.0001 Time: P < 0.0001 Group: P = 0.0058 Interaction: F (13, 130) = 5.972 Time: F (13, 130) = 3.644 Group: F (1, 10) = 12.22 0 min: P = 0.8556 5 min: P = 0.9980 10 min: P = 0.9832 15 min: P > 0.9999 20 min: P = 0.9015 25 min: P = 0.9686 30 min: P > 0.9999 35 min: P = 0.5105 40 min: P = 0.0018 45 min: P < 0.0001 50 min: P = 0.0064

			55 min: P = 0.0035 60 min: P = 0.0012 65 min: P = 0.0023
20D (Tail temperature)	6 (hM4Di) 6 (mCherry)	Two-way repeated-measures ANOVA Factor one: Time Factor two: Group post-hoc correction for multiple comparisons (Bonferroni)	Interaction: P = 0.3779 Time: P < 0.0001 Group: P = 0.2228 Interaction: F (13, 130) = 1.085 Time: F (13, 130) = 215.1 Group: F (1, 10) = 1.690 0 min: P > 0.9999 5 min: P > 0.9999 10 min: P > 0.9999 15 min: P > 0.9999 20 min: P > 0.9999 25 min: P > 0.9999 30 min: P > 0.9999 35 min: P > 0.9999 40 min: P > 0.9999 45 min: P > 0.9999 50 min: P = 0.9994 55 min: P = 0.2976 60 min: P = 0.4932 65 min: P = 0.2939
21B	260 neurons from 12 mice	Wilcoxon signed rank test (two-tailed) Bonferroni correction for multiple comparison	
21H	111 neurons (Heat, 8˚C inhibited) 136 neurons (Heat, 37˚C excited)	Hypergeometric test	P < 0.0001
21I	76 neurons (Thermal P&R) 86 neurons (Caloric reward)	Hypergeometric test	P = 0.024
21J (left)	76 neurons	Friedmann test Post-hoc correction for multiple comparison (Dunn's)	P < 0.0001 8˚C vs. 37˚C : P < 0.0001 8˚C vs. Liquid food : P < 0.0001 37˚C vs. Liquid food: P < 0.0001
21J (left) ; Baseline vs. Response time window	76 neurons	Wilcoxon signed rank test (two-tailed)	8˚C: P < 0.0001 37˚C: P < 0.0001 Liquid food: P < 0.0001
21J (right)	86 neurons	Friedmann test Post-hoc correction for multiple comparison (Dunn's)	P < 0.0001 8˚C vs. 37˚C : P < 0.0001 8˚C vs. Liquid food : P < 0.0001 37˚C vs. Liquid food: P < 0.0001
21J (right) ; Baseline vs. Response time window	86 neurons	Wilcoxon signed rank test (two-tailed)	8˚C: P < 0.0001 37˚C: P < 0.0001 Liquid food: P < 0.0001

23B	111 neurons from 8 mice	Wilcoxon signed rank test (two-tailed) Bonferroni correction for multiple comparison	
23D	10 neurons (quinine excited) 29 neurons (Thermal P&R)	Hypergeometric test	P = 0
23D	89 neurons (Shock excited) 29 neurons (Thermal P&R)	Hypergeometric test	P = 0
23F	80 neurons from 6 mice	Wilcoxon signed rank test (two-tailed)	
23H	29 neurons (Shock off inhibited) 22 neurons (Thermal P&R)	Hypergeometric test	P = 0.18
24B	112 neurons from 7 mice	Wilcoxon signed rank test (two-tailed)	
24E	27 neurons (Thermal P&R) 21 neurons (Lever press excited)	Hypergeometric test	P < 0.0001
24F (right)	27 neurons	Friedmann test Post-hoc correction for multiple comparison (Dunn's)	P < 0.0001 8˚C vs. 37˚C : P < 0.0001 8˚C vs. Lever press: P < 0.0001 37˚C vs. Lever press: P = 0.3515
24F (right) ; Baseline vs. Response time window	27 neurons	Wilcoxon signed rank test (two-tailed)	8˚C: P < 0.0001 37˚C: P < 0.0001 Lever: P < 0.0001
24G (right)	21 neurons	Friedmann test Post-hoc correction for multiple comparison (Dunn's)	P < 0.0001 8˚C vs. 37˚C : P < 0.0001 8˚C vs. Lever press : P < 0.0001 37˚C vs. Lever press: P = 0.9982
24G (right) ; Baseline vs. Response time window	21 neurons	Wilcoxon signed rank test (two-tailed)	8˚C: P < 0.0001 37˚C: P < 0.001 Lever: P < 0.0001
25C	10 (hM3Dq) 10 (mCherry)	Two-way repeated-measures ANOVA factor one: drug factor two: group post-hoc correction for multiple comparisons (Bonferroni)	Interaction: P = 0.0499 Drug: P = 0.0217 Group: P = 0.0763 F (2, 36) = 3.262 F (2, 36) = 4.271 F (1, 18) = 3.536 Day 1: P > 0.9999 Day 2: P = 0.0076 Day 3: P > 0.9999
25D	10 (hM3Dq) 8 (mCherry)	Two-way repeated-measures ANOVA	Interaction: P = 0.2945 Day: P = 0.4034

		factor one: day factor two: group	Group: P = 0.1766 F (2, 32) = 1.270 F (2, 32) = 0.8590 F (1, 16) = 1999
25F	3 (8˚C) 3 (37˚C)	Wilcoxon rank-sum test (two-tailed)	8˚C: P = 0.1 37˚C: P = 0.1
25G	3	Wilcoxon rank-sum test (two-tailed)	P = 0.7
25I	5 (8˚C) 4 (37˚C)	Wilcoxon rank-sum test (two-tailed)	8˚C: P = 0.6825 37˚C: P = 0.0286
25J	5	Wilcoxon rank-sum test (two-tailed)	P = 0.0079
25L	5 (8˚C) 6 (37˚C)	Wilcoxon rank-sum test (two-tailed)	8˚C: P = 0.18 37˚C: P = 0.18
25M	6	Wilcoxon rank-sum test (two-tailed)	P = 0.18
26C	3-4 sections from 2 mice		

Chapter 4. Conclusion

This dissertation presents findings on neural circuit mechanisms underlying two basic homeostatic behaviors: ingestive and thermoregulatory behaviors.

Chapter 2 demonstrates the evidence that PB^{Pdyn} neurons monitor the ingestion of both fluids and solids by using mechanosensory signals from the digestive tract organs, which are transmitted via the cranial nerve pathways (with the vagal pathway conveying the stomach-distension signals) (Figure 27). The mechanosensory signals from different digestive tract parts are likely to be integrated on the PB, such that individual PB^{Pdyn} neurons represent integrated mechanosensory signals from the mouth and the stomach. In turn, PB^{Pdyn} neurons transmit sustained appetite-suppressing signals that deter the initiation (but not maintenance) of ingestive behaviors to the downstream areas including the PVH, to limit excessive feeding and drinking as negative feedback.

This research points to a mechanism by which upper digestive tract mechanosensation is integrated and converted to a sensory feedback signal that suppresses appetite. This would cooperate with additional feedback mechanisms based on various qualities of ingesta, including nutrition (*55*, *58*, *60*), osmolality,

temperature, and taste (*40*, *41*). Different feedback mechanisms use neuronal and hormonal signals that originate from various parts of the digestive system, which may cooperatively alter ingestive behaviors (*45*, *47*, *75*, *34*, *49*, *4*, *52*, *77*, *55*, *40*, *41*, *70*, *58*, *60*, *63*, *175*). Further insights into the neural principles underlying ingestive behaviors will be gained by identifying circuit mechanisms for the integration of these inputs, as well as the internal needs, such as hunger and thirst, for determining the behavioral output (*34*, *40*, *41*, *45*, *47*, *49*, *75*). In the clinical perspective, our findings also provide insight into the mechanisms underlying gastric bypass surgery (which can cause the remaining stomach to distend when food is consumed), vagus nerve stimulation, and gastric balloon therapy for treating obesity and diabetes (*176*). The function of circuits revealed in this study may serve as a possible target for a novel therapeutic approach to treat metabolic disorders and obesity.

Chapter 3 presents the studies on the role of a group of neurons within the hypothalamus, one of the oldest brain regions (*177*), and for a parabrachial-to-hypothalamic neural circuit in mediating thermoregulatory behavior (Figure 28). I specifically investigated the correlative and causal functions that LH^{Vgat} neurons serve in behavioral thermoregulation and discovered that these neurons are necessary for a variety of thermoregulatory behaviors.

Regardless of the stimulus temperature, the overall activity of LH^{Vgat} neurons encodes thermal P&R as well as thermoregulatory behavior, representing motivational properties of thermal stimulus in addition to the thermoregulatory behavior itself. Multiple brain regions, including the LPB, provide direct inputs to LH^{Vgat} neurons, and the inputs from the LPB are selectively required for the encoding of thermal reward by LH^{Vgat} neurons and thermoregulatory behavior. The two-photon imaging experiments showed two functionally different subpopulations of LH^{Vgat} neurons, one encoding caloric reward stimuli and the other encoding thermal P&R. In addition, thermal P&R-encoding LH^{Vgat} neurons are engaged in thermoregulatory behavior, suggesting a critical role of this LH^{Vgat} subpopulation in guiding thermoregulatory behavior.

Our research collectively suggests that LH^{Vgat} neurons and the parabrachial-to-hypothalamic neural pathway serve as neural underpinnings for behavioral thermoregulation. I believe that this research will pave a new way in revealing a more comprehensive understanding of neural mechanisms on how the brain behaviorally regulates thermal homeostasis. In addition to external thermosensory signals, a variety of other physiological factors influence thermoregulatory behavior, such as brain and core body temperatures, fluid and energy balance, inflammatory state,

menstrual stage, and circadian rhythm, (*178–184*). This could be accomplished by the extensive brain-wide inputs to LH^{Vgat} neurons, particularly the POA (*183*, *185*, *186*), DMH (*110*), arcuate hypothalamic nucleus (*187*), insular cortex (*104*, *188*), and dorsal raphe nucleus (*189*), all of which exhibit thermosensation-related activities and are crucial regions for regulating diverse homeostatic states. Furthermore, because thermal reward serves as a primary reward and thermoregulatory behavior is a fundamental motivated behavior, these findings also shed a new light on the mechanisms underpinning reward processing and motivated behavior. Investigating the neural principles underlying the representation of thermal stimuli and their motivational properties, and the translation of this information into proper behavior responses has the potential to provide a complete explanation of how a stimulus is transformed into behavioral actions, which is a central question of behavioral neuroscience.

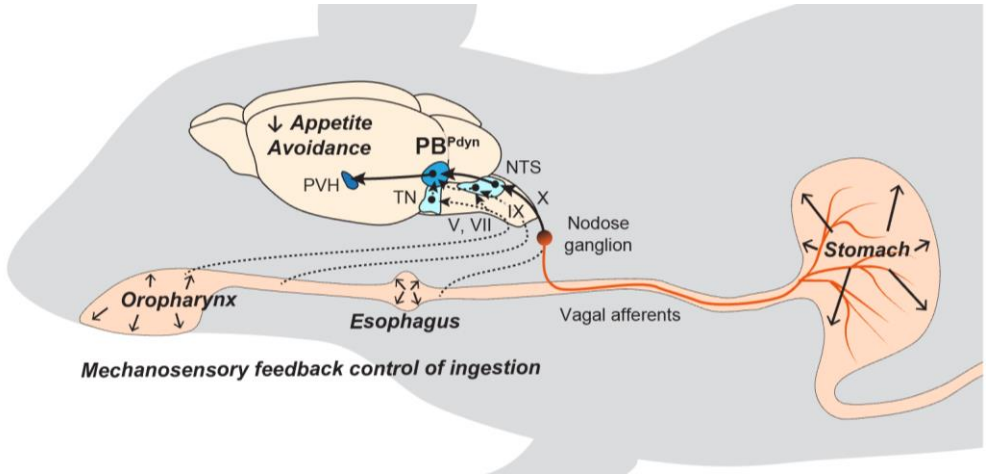

Figure 27. Summary model for a neural circuit mechanism underlying mechanosensory signals arising from the upper digestive tract organs for appetite regulation.

This figure is reprinted from (*99*).

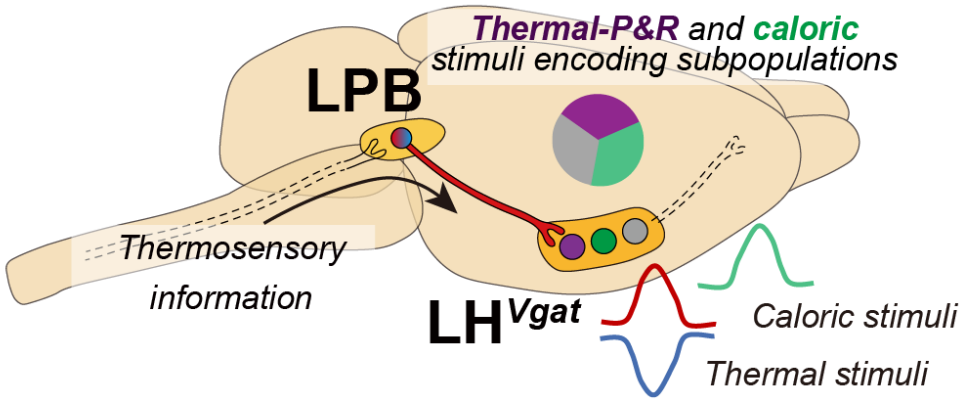

Figure 28. Summary model for a parabrachial-to-hypothalamic neural circuit underlying behavioral thermoregulation.

Bibliography

1. W. B. Cannon, Organization for physiological homeostasis. *Physiological Reviews*. 9, 399–431 (1929).
2. E. C. Tolman, *Purposive behavior in animals and men* (Century/Random House UK, London, England, 1932), *Purposive behavior in animals and men*.
3. A. H. Maslow, A theory of human motivation. *Psychological Review*. 50, 370–396 (1943).
4. N. E. Miller, Experiments on Motivation. *Science*. 126, 1271–1278 (1957).
5. D. J. McFarland, "Behavioral Aspects of Homeostasis11This paper was written as part of a project on behavioral systems analysis financed by the Science Research Council. The author is grateful to Dr. James Dewson III and to Professor L. W. Weiskrantz for their helpful criticism of the manuscript." in *Advances in the Study of Behavior*, D. S. Lehrman, R. A. Hinde, E. Shaw, Eds. (Academic Press, 1971; https://www.sciencedirect.com/science/article/pii/S0065345408601539), vol. 3, pp. 1–26.
6. S. M. Sternson, Hypothalamic survival circuits: blueprints for purposive behaviors. *Neuron*. 77, 810–824 (2013).
7. S. Sm, A. D, B. Jn, H. Fe, X. S, An Emerging Technology Framework for the Neurobiology of Appetite. *Cell metabolism*. 23 (2016), doi:10.1016/j.cmet.2015.12.002.
8. B. G. Hoebel, P. Teitelbaum, Hypothalamic control of feeding and self-stimulation. *Science*. 135, 375–377 (1962).
9. B. G. Stanley, S. F. Leibowitz, Neuropeptide Y: stimulation of feeding and drinking by injection into the paraventricular nucleus. *Life Sci*. 35, 2635–2642 (1984).
10. M. A. Greer, Suggestive evidence of a primary drinking center in hypothalamus of the rat. *Proc Soc Exp Biol Med*. 89, 59–62 (1955).
11. S. P. Grossman, Eating or drinking elicited by direct adrenergic or cholinergic stimulation of hypothalamus. *Science*. 132, 301–302 (1960).
12. B. Ja, D. Jb, Temperature receptors in the central nervous system. *Annual review of physiology*. 48 (1986), doi:10.1146/annurev.ph.48.030186.003231.
13. E. Vaughan, A. E. Fisher, Male sexual behavior induced by intracranial electrical stimulation. *Science*. 137, 758–760 (1962).
14. B. K. Anand, J. R. Brobeck, Localization of a “feeding center” in the hypothalamus of the rat. *Proc Soc Exp Biol Med*. 77, 323–324 (1951).
15. D. G. Montemurro, J. A. Stevenson, Adipsia produced by hypothalamic lesions in the rat. *Can J Biochem Physiol*. 35, 31–37 (1957).
16. S. P. Grossman, L. Grossman, FOOD AND WATER INTAKE FOLLOWING LESIONS OR ELECTRICAL STIMULATION OF THE AMYGDALA. *Am J Physiol*. 205, 761–765 (1963).

17. A. Sclafani, J. D. Belluzzi, S. P. Grossman, Effects of lesions in the hypothalamus and amygdala on feeding behavior in the rat. *Journal of Comparative and Physiological Psychology*. 72, 394–403 (1970).
18. E. Satinoff, S. Y. Shan, Loss of behavioral thermoregulation after lateral hypothalamic lesions in rats. *J Comp Physiol Psychol*. 77, 302–312 (1971).
19. J. M. R. Delgado, B. K. Anand, Increase of food intake induced by electrical stimulation of the lateral hypothalamus. *Am J Physiol*. 172, 162–168 (1953).
20. G. J. Mogenson, J. A. Stevenson, Drinking induced by electrical stimulation of the lateral hypothalamus. *Exp Neurol*. 17, 119–127 (1967).
21. L. L, C. Em, S. K, Genetic dissection of neural circuits. *Neuron*. 57 (2008), doi:10.1016/j.neuron.2008.01.002.
22. C. K. Kim, A. Adhikari, K. Deisseroth, Integration of optogenetics with complementary methodologies in systems neuroscience. *Nat Rev Neurosci*. 18, 222–235 (2017).
23. L. Luo, E. M. Callaway, K. Svoboda, Genetic Dissection of Neural Circuits: A Decade of Progress. *Neuron*. 98, 256–281 (2018).
24. A. Vázquez-Guardado, Y. Yang, A. J. Bandodkar, J. A. Rogers, Recent advances in neurotechnologies with broad potential for neuroscience research. *Nat Neurosci*. 23, 1522–1536 (2020).
25. K. M. Tye, K. Deisseroth, Optogenetic investigation of neural circuits underlying brain disease in animal models. *Nat Rev Neurosci*. 13, 251–266 (2012).
26. J. S. Wiegert, M. Mahn, M. Prigge, Y. Printz, O. Yizhar, Silencing Neurons: Tools, Applications, and Experimental Constraints. *Neuron*. 95, 504–529 (2017).
27. B. L. Roth, DREADDs for Neuroscientists. *Neuron*. 89, 683–694 (2016).
28. M. Z. Lin, M. J. Schnitzer, Genetically encoded indicators of neuronal activity. *Nat Neurosci*. 19, 1142–1153 (2016).
29. A. Andreoni, C. M. O. Davis, L. Tian, Measuring brain chemistry using genetically encoded fluorescent sensors. *Current Opinion in Biomedical Engineering*. 12, 59–67 (2019).
30. E. M. Callaway, Transneuronal circuit tracing with neurotropic viruses. *Curr Opin Neurobiol*. 18, 617–623 (2008).
31. J. J. Nassi, C. L. Cepko, R. T. Born, K. T. Beier, Neuroanatomy goes viral! *Front Neuroanat*. 9, 80 (2015).
32. A. R. Nectow, E. J. Nestler, Viral tools for neuroscience. *Nat Rev Neurosci*. 21, 669–681 (2020).
33. X. X, H. Tc, L. Mh, B. Kt, H. Gd, Z. F, Z. W, H. M, S. Bl, S.-G. Rm, Viral Vectors for Neural Circuit Mapping and Recent Advances in Trans-synaptic Anterograde Tracers. *Neuron*. 107 (2020), doi:10.1016/j.neuron.2020.07.010.
34. M. L. Andermann, B. B. Lowell, Toward a Wiring Diagram Understanding of Appetite Control. *Neuron*. 95, 757–778 (2017).
35. K. Timper, J. C. Brüning, Hypothalamic circuits regulating appetite

and energy homeostasis: pathways to obesity. *Dis Model Mech*. 10, 679–689 (2017).
36. S. M. Sternson, A.-K. Eiselt, Three Pillars for the Neural Control of Appetite. *Annu Rev Physiol*. 79, 401–423 (2017).
37. M. A. Rossi, G. D. Stuber, Overlapping Brain Circuits for Homeostatic and Hedonic Feeding. *Cell Metab*. 27, 42–56 (2018).
38. A. G. Watts, S. E. Kanoski, G. Sanchez-Watts, W. Langhans, The physiological control of eating: signals, neurons, and networks. *Physiol Rev*. 102, 689–813 (2022).
39. B. H. Ahn, M. Kim, S.-Y. Kim, Brain circuits for promoting homeostatic and non-homeostatic appetites. *Exp Mol Med*. 54, 349–357 (2022).
40. C. A. Zimmerman, D. E. Leib, Z. A. Knight, Neural circuits underlying thirst and fluid homeostasis. *Nat. Rev. Neurosci.* 18, 459–469 (2017).
41. V. Augustine, S. Lee, Y. Oka, Neural Control and Modulation of Thirst, Sodium Appetite, and Hunger. *Cell*. 180, 25–32 (2020).
42. J. J. Walsh, D. J. Christoffel, X. Wu, M. B. Pomrenze, R. C. Malenka, Dissecting neural mechanisms of prosocial behaviors. *Curr Opin Neurobiol*. 68, 9–14 (2021).
43. C. R. Lee, A. Chen, K. M. Tye, The neural circuitry of social homeostasis: Consequences of acute versus chronic social isolation. *Cell*. 184, 1500–1516 (2021).
44. D. Wei, V. Talwar, D. Lin, Neural circuits of social behaviors: Innate yet flexible. *Neuron*. 109, 1600–1620 (2021).
45. G. J. Schwartz, The role of gastrointestinal vagal afferents in the control of food intake: current prospects. *Nutrition*. 16, 866–873 (2000).
46. R. C. Ritter, Gastrointestinal mechanisms of satiation for food. *Physiology & Behavior*. 81, 249–273 (2004).
47. D. E. Cummings, J. Overduin, Gastrointestinal regulation of food intake. *J Clin Invest*. 117, 13–23 (2007).
48. E. M. Stricker, M. L. Hoffmann, Presystemic signals in the control of thirst, salt appetite, and vasopressin secretion. *Physiol. Behav.* 91, 404–412 (2007).
49. C. Gizowski, C. W. Bourque, The neural basis of homeostatic and anticipatory thirst. *Nat Rev Nephrol*. 14, 11–25 (2018).
50. P. J. Ryan, The Neurocircuitry of fluid satiation. *Physiol Rep*. 6, e13744 (2018).
51. B. J. Rolls, E. T. Rolls, *Thirst* (Cambridge University Press, Cambridge ; New York, 1982).
52. T. L. Powley, R. J. Phillips, Gastric satiation is volumetric, intestinal satiation is nutritive. *Physiology & Behavior*. 82, 69–74 (2004).
53. G. Bardos, Behavioral consequences of intestinal distention: Aversivity and discomfort. *Physiology & Behavior*. 45, 79–85 (1989).
54. C. A. Campos, A. J. Bowen, M. W. Schwartz, R. D. Palmiter, Parabrachial CGRP Neurons Control Meal Termination. *Cell Metabolism*. 23, 811–820 (2016).
55. H.-R. Berthoud, Vagal and hormonal gut–brain communication: from

satiation to satisfaction. *Neurogastroenterology & Motility*. 20, 64–72 (2008).
56. C. A. Zimmerman, Y.-C. Lin, D. E. Leib, L. Guo, E. L. Huey, G. E. Daly, Y. Chen, Z. A. Knight, Thirst neurons anticipate the homeostatic consequences of eating and drinking. *Nature*. 537, 680–684 (2016).
57. S. Lee, V. Augustine, Y. Zhao, H. Ebisu, B. Ho, D. Kong, Y. Oka, Chemosensory modulation of neural circuits for sodium appetite. *Nature*. 568, 93–97 (2019).
58. L. R. Beutler, Y. Chen, J. S. Ahn, Y.-C. Lin, R. A. Essner, Z. A. Knight, Dynamics of Gut-Brain Communication Underlying Hunger. *Neuron*. 96, 461-475.e5 (2017).
59. C. A. Zimmerman, E. L. Huey, J. S. Ahn, L. R. Beutler, C. L. Tan, S. Kosar, L. Bai, Y. Chen, T. V. Corpuz, L. Madisen, H. Zeng, Z. A. Knight, A gut-to-brain signal of fluid osmolarity controls thirst satiation. *Nature*. 568, 98–102 (2019).
60. Z. Su, A. L. Alhadeff, J. N. Betley, Nutritive, Post-ingestive Signals Are the Primary Regulators of AgRP Neuron Activity. *Cell Reports*. 21, 2724–2736 (2017).
61. V. Augustine, S. K. Gokce, S. Lee, B. Wang, T. J. Davidson, F. Reimann, F. Gribble, K. Deisseroth, C. Lois, Y. Oka, Hierarchical neural architecture underlying thirst regulation. *Nature*. 555, 204–209 (2018).
62. E. K. Williams, R. B. Chang, D. E. Strochlic, B. D. Umans, B. B. Lowell, S. D. Liberles, Sensory Neurons that Detect Stretch and Nutrients in the Digestive System. *Cell*. 166, 209–221 (2016).
63. L. Bai, S. Mesgarzadeh, K. S. Ramesh, E. L. Huey, Y. Liu, L. A. Gray, T. J. Aitken, Y. Chen, L. R. Beutler, J. S. Ahn, L. Madisen, H. Zeng, M. A. Krasnow, Z. A. Knight, Genetic Identification of Vagal Sensory Neurons That Control Feeding. *Cell*. 179, 1129-1143.e23 (2019).
64. C. B. Saper, The central autonomic nervous system: conscious visceral perception and autonomic pattern generation. *Annu. Rev. Neurosci.* 25, 433–469 (2002).
65. R. J. Contreras, R. M. Beckstead, R. Norgren, The central projections of the trigeminal, facial, glossopharyngeal and vagus nerves: an autoradiographic study in the rat. *J. Auton. Nerv. Syst.* 6, 303–322 (1982).
66. S. M. Altschuler, X. Bao, D. Bieger, D. A. Hopkins, R. R. Miselis, Viscerotopic representation of the upper alimentary tract in the rat: Sensory ganglia and nuclei of the solitary and spinal trigeminal tracts. *Journal of Comparative Neurology*. 283, 248–268 (1989).
67. H. Herbert, M. M. Moga, C. B. Saper, Connections of the parabrachial nucleus with the nucleus of the solitary tract and the medullary reticular formation in the rat. *J. Comp. Neurol.* 293, 540–580 (1990).
68. R. D. Palmiter, The Parabrachial Nucleus: CGRP Neurons Function as a General Alarm. *Trends in Neurosciences*. 41, 280–293 (2018).
69. C. B. Saper, A. D. Loewy, Efferent connections of the parabrachial nucleus in the rat. *Brain Res.* 197, 291–317 (1980).
70. M. J. McKinley, A. K. Johnson, The Physiological Regulation of Thirst

and Fluid Intake. *Physiology*. 19, 1–6 (2004).
71. P. J. Ryan, S. I. Ross, C. A. Campos, V. A. Derkach, R. D. Palmiter, Oxytocin-receptor-expressing neurons in the parabrachial nucleus regulate fluid intake. *Nat. Neurosci.* 20, 1722–1733 (2017).
72. M. E. Carter, M. E. Soden, L. S. Zweifel, R. D. Palmiter, Genetic identification of a neural circuit that suppresses appetite. *Nature*. 503, 111–114 (2013).
73. G. J. Schwartz, P. R. McHugh, T. H. Moran, Integration of vagal afferent responses to gastric loads and cholecystokinin in rats. *American Journal of Physiology-Regulatory, Integrative and Comparative Physiology*. 261, R64–R69 (1991).
74. H. Karimnamazi, S. P. Travers, J. B. Travers, Oral and gastric input to the parabrachial nucleus of the rat. *Brain Research*. 957, 193–206 (2002).
75. B. D. Umans, S. D. Liberles, Neural Sensing of Organ Volume. *Trends in Neurosciences*. 41, 911–924 (2018).
76. D. Grundy, T. Scratcherd, Sensory afferents from the gastrointestinal tract. *Comprehensive Physiology* (2011), doi:10.1002/cphy.cp060116.
77. S. Eisen, J. D. Davis, E. Rauhofer, G. P. Smith, Gastric negative feedback produced by volume and nutrient during a meal in rats. *American Journal of Physiology-Regulatory, Integrative and Comparative Physiology*. 281, R1201–R1214 (2001).
78. A. S. Garfield, C. Li, J. C. Madara, B. P. Shah, E. Webber, J. S. Steger, J. N. Campbell, O. Gavrilova, C. E. Lee, D. P. Olson, J. K. Elmquist, B. A. Tannous, M. J. Krashes, B. B. Lowell, A neural basis for melanocortin-4 receptor–regulated appetite. *Nature Neuroscience*. 18, 863–871 (2015).
79. C. Li, J. Navarrete, J. Liang-Guallpa, C. Lu, S. C. Funderburk, R. B. Chang, S. D. Liberles, D. P. Olson, M. J. Krashes, Defined Paraventricular Hypothalamic Populations Exhibit Differential Responses to Food Contingent on Caloric State. *Cell Metab.* 29, 681-694.e5 (2019).
80. M. M. Li, J. C. Madara, J. S. Steger, M. J. Krashes, N. Balthasar, J. N. Campbell, J. M. Resch, N. J. Conley, A. S. Garfield, B. B. Lowell, The Paraventricular Hypothalamus Regulates Satiety and Prevents Obesity via Two Genetically Distinct Circuits. *Neuron*. 102, 653-667.e6 (2019).
81. J. Kim, S. Lee, Y.-Y. Fang, A. Shin, S. Park, K. Hashikawa, S. Bhat, D. Kim, J.-W. Sohn, D. Lin, G. S. B. Suh, Rapid, biphasic CRF neuronal responses encode positive and negative valence. *Nat Neurosci*. 22, 576–585 (2019).
82. A. Barik, J. H. Thompson, M. Seltzer, N. Ghitani, A. T. Chesler, A Brainstem-Spinal Circuit Controlling Nocifensive Behavior. *Neuron*. 100, 1491-1503.e3 (2018).
83. C. J. Burnett, C. Li, E. Webber, E. Tsaousidou, S. Y. Xue, J. C. Brüning, M. J. Krashes, Hunger-Driven Motivational State Competition. *Neuron*. 92, 187–201 (2016).
84. H. Cai, W. Haubensak, T. E. Anthony, D. J. Anderson, Central

amygdala PKC-δ^+ neurons mediate the influence of multiple anorexigenic signals. *Nature Neuroscience*. 17, 1240–1248 (2014).
85. E. J. Kim, M. W. Jacobs, T. Ito-Cole, E. M. Callaway, Improved Monosynaptic Neural Circuit Tracing Using Engineered Rabies Virus Glycoproteins. *Cell Reports*. 15, 692–699 (2016).
86. K. Miyamichi, Y. Shlomai-Fuchs, M. Shu, B. C. Weissbourd, L. Luo, A. Mizrahi, Dissecting Local Circuits: Parvalbumin Interneurons Underlie Broad Feedback Control of Olfactory Bulb Output. *Neuron*. 80, 1232–1245 (2013).
87. Z. V. Guo, S. A. Hires, N. Li, D. H. O'Connor, T. Komiyama, E. Ophir, D. Huber, C. Bonardi, K. Morandell, D. Gutnisky, S. Peron, N. Xu, J. Cox, K. Svoboda, Procedures for Behavioral Experiments in Head-Fixed Mice. *PLOS ONE*. 9, e88678 (2014).
88. V. M. K. Namboodiri, J. M. Otis, K. van Heeswijk, E. S. Voets, R. A. Alghorazi, J. Rodriguez-Romaguera, S. Mihalas, G. D. Stuber, Single-cell activity tracking reveals that orbitofrontal neurons acquire and maintain a long-term memory to guide behavioral adaptation. *Nat Neurosci*. 22, 1110–1121 (2019).
89. I. R. Wickersham, S. Finke, K.-K. Conzelmann, E. M. Callaway, Retrograde neuronal tracing with a deletion-mutant rabies virus. *Nat. Methods*. 4, 47–49 (2007).
90. M. Loukas, Z. Klaassen, W. Merbs, R. S. Tubbs, J. Gielecki, A. Zurada, A review of the thoracic splanchnic nerves and celiac ganglia. *Clinical Anatomy*. 23, 512–522 (2010).
91. T. N. Lerner, C. Shilyansky, T. J. Davidson, K. E. Evans, K. T. Beier, K. A. Zalocusky, A. K. Crow, R. C. Malenka, L. Luo, R. Tomer, K. Deisseroth, Intact-Brain Analyses Reveal Distinct Information Carried by SNc Dopamine Subcircuits. *Cell*. 162, 635–647 (2015).
92. G. Wang, S. C. Fowler, Effects of haloperidol and clozapine on tongue dynamics during licking in CD-1, BALB/c and C57BL/6 mice. *Psychopharmacology*. 147, 38–45 (1999).
93. L. A. Marowitz, B. P. Halpern, The effects of environmental constraints upon licking patterns. *Physiology & Behavior*. 11, 259–263 (1973).
94. M. A. Rossi, H. H. Yin, Elevated dopamine alters consummatory pattern generation and increases behavioral variability during learning. *Front. Integr. Neurosci.* 9 (2015), doi:10.3389/fnint.2015.00037.
95. E. L. McConnell, A. W. Basit, S. Murdan, Measurements of rat and mouse gastrointestinal pH, fluid and lymphoid tissue, and implications for in-vivo experiments. *J. Pharm. Pharmacol.* 60, 63–70 (2008).
96. C. Casteleyn, A. Rekecki, A. Van Der Aa, P. Simoens, W. Van Den Broeck, Surface area assessment of the murine intestinal tract as a prerequisite for oral dose translation from mouse to man. *Lab Anim*. 44, 176–183 (2010).
97. J. M. Stujenske, T. Spellman, J. A. Gordon, Modeling the Spatiotemporal Dynamics of Light and Heat Propagation for In Vivo Optogenetics. *Cell Rep*. 12, 525–534 (2015).

98. E. A. Susaki, K. Tainaka, D. Perrin, H. Yukinaga, A. Kuno, H. R. Ueda, Advanced CUBIC protocols for whole-brain and whole-body clearing and imaging. *Nature Protocols*. 10, 1709–1727 (2015).
99. D.-Y. Kim, G. Heo, M. Kim, H. Kim, J. A. Jin, H.-K. Kim, S. Jung, M. An, B. H. Ahn, J. H. Park, H.-E. Park, M. Lee, J. W. Lee, G. J. Schwartz, S.-Y. Kim, A neural circuit mechanism for mechanosensory feedback control of ingestion. *Nature*. 580, 376–380 (2020).
100. S. F. Morrison, K. Nakamura, Central neural pathways for thermoregulation. *Front Biosci (Landmark Ed)*. 16, 74–104 (2011).
101. M. C. Almeida, R. C. L. Vizin, D. C. Carrettiero, Current understanding on the neurophysiology of behavioral thermoregulation. *Temperature (Austin)*. 2, 483–490 (2015).
102. A. A. Romanovsky, The thermoregulation system and how it works. *Handb Clin Neurol*. 156, 3–43 (2018).
103. C. L. Tan, Z. A. Knight, Regulation of Body Temperature by the Nervous System. *Neuron*. 98, 31–48 (2018).
104. A. D. Craig, How do you feel? Interoception: the sense of the physiological condition of the body. *Nature Reviews Neuroscience*. 3, 655–666 (2002).
105. N. Milenkovic, W.-J. Zhao, J. Walcher, T. Albert, J. Siemens, G. R. Lewin, J. F. A. Poulet, A somatosensory circuit for cooling perception in mice. *Nat Neurosci*. 17, 1560–1566 (2014).
106. C. Ran, M. A. Hoon, X. Chen, The coding of cutaneous temperature in the spinal cord. *Nat Neurosci*. 19, 1201–1209 (2016).
107. R. Paricio-Montesinos, F. Schwaller, A. Udhayachandran, F. Rau, J. Walcher, R. Evangelista, J. Vriens, T. Voets, J. F. A. Poulet, G. R. Lewin, The Sensory Coding of Warm Perception. *Neuron*. 106, 830–841.e3 (2020).
108. T. Yahiro, N. Kataoka, Y. Nakamura, K. Nakamura, The lateral parabrachial nucleus, but not the thalamus, mediates thermosensory pathways for behavioural thermoregulation. *Scientific Reports*. 7, 1–10 (2017).
109. J. Siemens, G. B. Kamm, Cellular populations and thermosensing mechanisms of the hypothalamic thermoregulatory center. *Pflugers Arch - Eur J Physiol*. 470, 809–822 (2018).
110. Z.-D. Zhao, W. Z. Yang, C. Gao, X. Fu, W. Zhang, Q. Zhou, W. Chen, X. Ni, J.-K. Lin, J. Yang, X.-H. Xu, W. L. Shen, A hypothalamic circuit that controls body temperature. *Proc. Natl. Acad. Sci. U.S.A.* 114, 2042–2047 (2017).
111. H. J. Carlisle, Effect of preoptic and anterior hypothalamic lesions on behavioral thermoregulation in the cold. *J Comp Physiol Psychol*. 69, 391–402 (1969).
112. E. Satinoff, J. Rutstein, Behavioral thermoregulation in rats with anterior hypothalamic lesions. *J Comp Physiol Psychol*. 71, 77–82 (1970).
113. C. B. Saper, T. C. Chou, J. K. Elmquist, The Need to Feed: Homeostatic and Hedonic Control of Eating. *Neuron*. 36, 199–211 (2002).

114. G. D. Stuber, R. A. Wise, Lateral hypothalamic circuits for feeding and reward. *Nat. Neurosci.* 19, 198–205 (2016).
115. H.-R. Berthoud, H. Münzberg, The lateral hypothalamus as integrator of metabolic and environmental needs: from electrical self-stimulation to opto-genetics. *Physiol. Behav.* 104, 29–39 (2011).
116. P. Bonnavion, L. E. Mickelsen, A. Fujita, L. de Lecea, A. C. Jackson, Hubs and spokes of the lateral hypothalamus: cell types, circuits and behaviour. *J. Physiol. (Lond.)*. 594, 6443–6462 (2016).
117. J. A. Brown, H. L. Woodworth, G. M. Leinninger, To ingest or rest? Specialized roles of lateral hypothalamic area neurons in coordinating energy balance. *Front Syst Neurosci*. 9, 9 (2015).
118. D. Burdakov, Reactive and predictive homeostasis: Roles of orexin/hypocretin neurons. *Neuropharmacology*. 154, 61–67 (2019).
119. S. W. Hurley, A. K. Johnson, The role of the lateral hypothalamus and orexin in ingestive behavior: a model for the translation of past experience and sensed deficits into motivated behaviors. *Front Syst Neurosci*. 8, 216 (2014).
120. G. D. Petrovich, Lateral Hypothalamus as a Motivation–Cognition Interface in the Control of Feeding Behavior. *Front. Syst. Neurosci.* 12 (2018), doi:10.3389/fnsys.2018.00014.
121. P. Dilsiz, I. Aklan, N. Sayar Atasoy, Y. Yavuz, G. Filiz, F. Koksalar, T. Ates, M. Oncul, I. Coban, E. Ates Oz, U. Cebecioglu, M. I. Alp, B. Yilmaz, D. Atasoy, MCH Neuron Activity Is Sufficient for Reward and Reinforces Feeding. *Neuroendocrinology*. 110, 258–270 (2020).
122. E. H. Nieh, C. M. Vander Weele, G. A. Matthews, K. N. Presbrey, R. Wichmann, C. A. Leppla, E. M. Izadmehr, K. M. Tye, Inhibitory Input from the Lateral Hypothalamus to the Ventral Tegmental Area Disinhibits Dopamine Neurons and Promotes Behavioral Activation. *Neuron*. 90, 1286–1298 (2016).
123. J. M. Otis, M. Zhu, V. M. K. Namboodiri, C. A. Cook, O. Kosyk, A. M. Matan, R. Ying, Y. Hashikawa, K. Hashikawa, I. Trujillo-Pisanty, J. Guo, R. L. Ung, J. Rodriguez-Romaguera, E. S. Anton, G. D. Stuber, Paraventricular Thalamus Projection Neurons Integrate Cortical and Hypothalamic Signals for Cue-Reward Processing. *Neuron*. 103, 423-431.e4 (2019).
124. Y. Li, J. Zeng, J. Zhang, C. Yue, W. Zhong, Z. Liu, Q. Feng, M. Luo, Hypothalamic Circuits for Predation and Evasion. *Neuron*. 97, 911-924.e5 (2018).
125. J. G. Van Zoeren, E. M. Stricker, Effects of preoptic, lateral hypothalamic, or dopamine-depleting lesions on behavioral thermoregulation in rats exposed to the cold. *Journal of Comparative and Physiological Psychology*. 91, 989–999 (1977).
126. R. Refinetti, H. J. Carlisle, Effects of lateral hypothalamic lesions on thermoregulation in the rat. *Physiol. Behav.* 38, 219–228 (1986).
127. R. Refinetti, H. J. Carlisle, A reevaluation of the role of the lateral hypothalamus in behavioral temperature regulation. *Physiol. Behav.* 40, 189–192 (1987).
128. E. Arrigoni, M. J. S. Chee, P. M. Fuller, To eat or to sleep: That is a

lateral hypothalamic question. *Neuropharmacology*. 154, 34–49 (2019).
129. L. E. Mickelsen, M. Bolisetty, B. R. Chimileski, A. Fujita, E. J. Beltrami, J. T. Costanzo, J. R. Naparstek, P. Robson, A. C. Jackson, Single-cell transcriptomic analysis of the lateral hypothalamic area reveals molecularly distinct populations of inhibitory and excitatory neurons. *Nature Neuroscience*. 22, 642–656 (2019).
130. M. A. Rossi, M. L. Basiri, J. A. McHenry, O. Kosyk, J. M. Otis, H. E. van den Munkhof, J. Bryois, C. Hübel, G. Breen, W. Guo, C. M. Bulik, P. F. Sullivan, G. D. Stuber, Obesity remodels activity and transcriptional state of a lateral hypothalamic brake on feeding. *Science*. 364, 1271–1274 (2019).
131. E. H. Nieh, G. A. Matthews, S. A. Allsop, K. N. Presbrey, C. A. Leppla, R. Wichmann, R. Neve, C. P. Wildes, K. M. Tye, Decoding Neural Circuits that Control Compulsive Sucrose Seeking. *Cell*. 160, 528–541 (2015).
132. J. H. Jennings, R. L. Ung, S. L. Resendez, A. M. Stamatakis, J. G. Taylor, J. Huang, K. Veleta, P. A. Kantak, M. Aita, K. Shilling-Scrivo, C. Ramakrishnan, K. Deisseroth, S. Otte, G. D. Stuber, Visualizing hypothalamic network dynamics for appetitive and consummatory behaviors. *Cell*. 160, 516–527 (2015).
133. A. Garcia, A. Coss, J. Luis-Islas, L. Puron-Sierra, M. Luna, M. Villavicencio, R. Gutierrez, Lateral Hypothalamic GABAergic Neurons Encode and Potentiate Sucrose's Palatability. *Front Neurosci*. 14, 608047 (2020).
134. R. A. M. Marino, R. A. McDevitt, S. C. Gantz, H. Shen, M. Pignatelli, W. Xin, R. A. Wise, A. Bonci, Control of food approach and eating by a GABAergic projection from lateral hypothalamus to dorsal pons. *PNAS* (2020), doi:10.1073/pnas.1909340117.
135. L. T. Oesch, M. Gazea, T. C. Gent, M. Bandarabadi, C. Gutierrez Herrera, A. R. Adamantidis, REM sleep stabilizes hypothalamic representation of feeding behavior. *Proc Natl Acad Sci U S A*. 117, 19590–19598 (2020).
136. J. N. Siemian, M. A. Arenivar, S. Sarsfield, Y. Aponte, Hypothalamic control of interoceptive hunger. *Curr Biol*, S0960-9822(21)00877-0 (2021).
137. P. L. Carlton, R. A. Marks, Cold Exposure and Heat Reinforced Operant Behavior. *Science*. 128, 1344–1344 (1958).
138. W. W. Roberts, R. D. Mooney, Brain areas controlling thermoregulatory grooming, prone extension, locomotion, and tail vasodilation in rats. *J Comp Physiol Psychol*. 86, 470–480 (1974).
139. M. Navarro, J. J. Olney, N. W. Burnham, C. M. Mazzone, E. G. Lowery-Gionta, K. E. Pleil, T. L. Kash, T. E. Thiele, Lateral Hypothalamus GABAergic Neurons Modulate Consummatory Behaviors Regardless of the Caloric Content or Biological Relevance of the Consumed Stimuli. *Neuropsychopharmacology*. 41, 1505–1512 (2016).
140. M. J. Sharpe, N. J. Marchant, L. R. Whitaker, C. T. Richie, Y. J. Zhang, E. J. Campbell, P. P. Koivula, J. C. Necarsulmer, C. Mejias-Aponte, M.

Morales, J. Pickel, J. C. Smith, Y. Niv, Y. Shaham, B. K. Harvey, G. Schoenbaum, Lateral Hypothalamic GABAergic Neurons Encode Reward Predictions that Are Relayed to the Ventral Tegmental Area to Regulate Learning. *Curr Biol*. 27, 2089-2100.e5 (2017).

141. R. M. Cassidy, Y. Lu, M. Jere, J.-B. Tian, Y. Xu, L. R. Mangieri, B. Felix-Okoroji, J. Selever, Y. Xu, B. R. Arenkiel, Q. Tong, A lateral hypothalamus to basal forebrain neurocircuit promotes feeding by suppressing responses to anxiogenic environmental cues. *Science Advances*. 5, eaav1640 (2019).
142. K. C. Berridge, "Pleasure, pain, desire, and dread: Hidden core processes of emotion" in *Well-being: The foundations of hedonic psychology* (Russell Sage Foundation, New York, NY, US, 1999), pp. 525–557.
143. K. M. Tye, Neural Circuit Motifs in Valence Processing. *Neuron*. 100, 436–452 (2018).
144. J. C. Geerling, M. Kim, C. E. Mahoney, S. B. G. Abbott, L. J. Agostinelli, A. S. Garfield, M. J. Krashes, B. B. Lowell, T. E. Scammell, Genetic identity of thermosensory relay neurons in the lateral parabrachial nucleus. *Am J Physiol Regul Integr Comp Physiol*. 310, R41-54 (2016).
145. K. Nakamura, "Chapter 16 - Afferent pathways for autonomic and shivering thermoeffectors" in *Handbook of Clinical Neurology*, A. A. Romanovsky, Ed. (Elsevier, 2018; https://www.sciencedirect.com/science/article/pii/B9780444639127000163), vol. 156 of *Thermoregulation: From Basic Neuroscience to Clinical Neurology Part I*, pp. 263–279.
146. W. Z. Yang, X. Du, W. Zhang, C. Gao, H. Xie, Y. Xiao, X. Jia, J. Liu, J. Xu, X. Fu, H. Tu, X. Fu, X. Ni, M. He, J. Yang, H. Wang, H. Yang, X.-H. Xu, W. L. Shen, Parabrachial neuron types categorically encode thermoregulation variables during heat defense. *Sci Adv*. 6 (2020), doi:10.1126/sciadv.abb9414.
147. V. A. J. de Vrind, A. Rozeboom, I. G. Wolterink-Donselaar, M. C. M. Luijendijk-Berg, R. A. H. Adan, Effects of GABA and Leptin Receptor-Expressing Neurons in the Lateral Hypothalamus on Feeding, Locomotion, and Thermogenesis. *Obesity (Silver Spring)*. 27, 1123–1132 (2019).
148. W. W. Roberts, J. R. Martin, Effects of lesions in central thermosensitive areas on thermoregulatory responses in rat. *Physiol Behav*. 19, 503–511 (1977).
149. M. C. Almeida, A. A. Steiner, L. G. S. Branco, A. A. Romanovsky, Neural substrate of cold-seeking behavior in endotoxin shock. *PLoS One*. 1, e1 (2006).
150. E. Satinoff, D. Valentino, P. Teitelbaum, Thermoregulatory cold-defense deficits in rats with preoptic/anterior hypothalamic lesions. *Brain Res Bull*. 1, 553–565 (1976).
151. K. Nakamura, S. F. Morrison, Central efferent pathways mediating skin cooling-evoked sympathetic thermogenesis in brown adipose tissue. *Am J Physiol Regul Integr Comp Physiol*. 292, R127-136

(2007).
152. S. F. Morrison, K. Nakamura, Central Mechanisms for Thermoregulation. *Annu Rev Physiol*. 81, 285–308 (2019).
153. J. M. Lipton, Effects of preoptic lesions on heat-escape responding and colonic temperature in the rat. *Physiology & Behavior*. 3, 165–169 (1968).
154. K. Nakamura, S. F. Morrison, A thermosensory pathway that controls body temperature. *Nat. Neurosci.* 11, 62–71 (2008).
155. K. Nakamura, S. F. Morrison, A thermosensory pathway mediating heat-defense responses. *PNAS*. 107, 8848–8853 (2010).
156. E. Qualls-Creekmore, S. Yu, M. Francois, J. Hoang, C. Huesing, A. Bruce-Keller, D. Burk, H.-R. Berthoud, C. D. Morrison, H. Münzberg, Galanin-Expressing GABA Neurons in the Lateral Hypothalamus Modulate Food Reward and Noncompulsive Locomotion. *J Neurosci*. 37, 6053–6065 (2017).
157. J. A. Brown, A. Wright, R. Bugescu, L. Christensen, D. P. Olson, G. M. Leinninger, Distinct Subsets of Lateral Hypothalamic Neurotensin Neurons are Activated by Leptin or Dehydration. *Sci Rep*. 9, 1873 (2019).
158. J. N. Siemian, M. A. Arenivar, S. Sarsfield, C. B. Borja, C. N. Russell, Y. Aponte, Lateral hypothalamic LEPR neurons drive appetitive but not consummatory behaviors. *Cell Rep*. 36, 109615 (2021).
159. L. E. Fenno, J. Mattis, C. Ramakrishnan, M. Hyun, S. Y. Lee, M. He, J. Tucciarone, A. Selimbeyoglu, A. Berndt, L. Grosenick, K. A. Zalocusky, H. Bernstein, H. Swanson, C. Perry, I. Diester, F. M. Boyce, C. E. Bass, R. Neve, Z. J. Huang, K. Deisseroth, Targeting cells with single vectors using multiple-feature Boolean logic. *Nat Methods*. 11, 763–772 (2014).
160. D.-W. Kim, Z. Yao, L. T. Graybuck, T. K. Kim, T. N. Nguyen, K. A. Smith, O. Fong, L. Yi, N. Koulena, N. Pierson, S. Shah, L. Lo, A.-H. Pool, Y. Oka, L. Pachter, L. Cai, B. Tasic, H. Zeng, D. J. Anderson, Multimodal Analysis of Cell Types in a Hypothalamic Node Controlling Social Behavior. *Cell*. 179, 713-728.e17 (2019).
161. A. F. Schier, Single-cell biology: beyond the sum of its parts. *Nat Methods*. 17, 17–20 (2020).
162. J. H. Jennings, C. K. Kim, J. H. Marshel, M. Raffiee, L. Ye, S. Quirin, S. Pak, C. Ramakrishnan, K. Deisseroth, Interacting neural ensembles in orbitofrontal cortex for social and feeding behaviour. *Nature*. 565, 645–649 (2019).
163. A. M. Packer, L. E. Russell, H. W. P. Dalgleish, M. Häusser, Simultaneous all-optical manipulation and recording of neural circuit activity with cellular resolution in vivo. *Nat Methods*. 12, 140–146 (2015).
164. S. V. Mahler, E. M. Vazey, J. T. Beckley, C. R. Keistler, E. M. McGlinchey, J. Kaufling, S. P. Wilson, K. Deisseroth, J. J. Woodward, G. Aston-Jones, Designer receptors show role for ventral pallidum input to ventral tegmental area in cocaine seeking. *Nat Neurosci*. 17, 577–585 (2014).

165. F. Leroy, J. Park, A. Asok, D. H. Brann, T. Meira, L. M. Boyle, E. W. Buss, E. R. Kandel, S. A. Siegelbaum, A circuit from hippocampal CA2 to lateral septum disinhibits social aggression. *Nature*. 564, 213–218 (2018).
166. G. Corder, B. Ahanonu, B. F. Grewe, D. Wang, M. J. Schnitzer, G. Scherrer, An amygdalar neural ensemble that encodes the unpleasantness of pain. *Science*. 363, 276–281 (2019).
167. W. W. Roberts, Differential thermosensor control of thermoregulatory grooming, locomotion, and relaxed postural extension. *Ann N Y Acad Sci*. 525, 363–374 (1988).
168. D.-Y. Kim, G. Heo, M. Kim, H. Kim, J. A. Jin, H.-K. Kim, S. Jung, M. An, B. H. Ahn, J. H. Park, H.-E. Park, M. Lee, J. W. Lee, G. J. Schwartz, S.-Y. Kim, A neural circuit mechanism for mechanosensory feedback control of ingestion. *Nature*. 580, 376–380 (2020).
169. W. E. Allen, L. A. DeNardo, M. Z. Chen, C. D. Liu, K. M. Loh, L. E. Fenno, C. Ramakrishnan, K. Deisseroth, L. Luo, Thirst-associated preoptic neurons encode an aversive motivational drive. *Science*. 357, 1149–1155 (2017).
170. L. A. DeNardo, C. D. Liu, W. E. Allen, E. L. Adams, D. Friedmann, L. Fu, C. J. Guenthner, M. Tessier-Lavigne, L. Luo, Temporal evolution of cortical ensembles promoting remote memory retrieval. *Nat Neurosci*. 22, 460–469 (2019).
171. L. Madisen, T. A. Zwingman, S. M. Sunkin, S. W. Oh, H. A. Zariwala, H. Gu, L. L. Ng, R. D. Palmiter, M. J. Hawrylycz, A. R. Jones, E. S. Lein, H. Zeng, A robust and high-throughput Cre reporting and characterization system for the whole mouse brain. *Nat Neurosci*. 13, 133–140 (2010).
172. S. Jung, M. Lee, D.-Y. Kim, C. Son, B. H. Ahn, G. Heo, J. Park, M. Kim, H.-E. Park, D.-J. Koo, J. H. Park, J. W. Lee, H. K. Choe, S.-Y. Kim, A forebrain neural substrate for behavioral thermoregulation. *Neuron*. 110, 266-279.e9 (2022).
173. H. Lee, L. J. Macpherson, C. A. Parada, C. S. Zuker, N. J. P. Ryba, Rewiring the taste system. *Nature*. 548, 330–333 (2017).
174. D. G. R. Tervo, B.-Y. Hwang, S. Viswanathan, T. Gaj, M. Lavzin, K. D. Ritola, S. Lindo, S. Michael, E. Kuleshova, D. Ojala, C.-C. Huang, C. R. Gerfen, J. Schiller, J. T. Dudman, A. W. Hantman, L. L. Looger, D. V. Schaffer, A. Y. Karpova, A Designer AAV Variant Permits Efficient Retrograde Access to Projection Neurons. *Neuron*. 92, 372–382 (2016).
175. W. Han, L. A. Tellez, M. H. Perkins, I. O. Perez, T. Qu, J. Ferreira, T. L. Ferreira, D. Quinn, Z.-W. Liu, X.-B. Gao, M. M. Kaelberer, D. V. Bohórquez, S. J. Shammah-Lagnado, G. de Lartigue, I. E. de Araujo, A Neural Circuit for Gut-Induced Reward. *Cell*. 175, 665-678.e23 (2018).
176. G. de Lartigue, Role of the vagus nerve in the development and treatment of diet-induced obesity. *J. Physiol. (Lond.)*. 594, 5791–5815 (2016).
177. C. B. Saper, B. B. Lowell, The hypothalamus. *Current Biology*. 24,

R1111–R1116 (2014).
178. C. L. Hamilton, W. Sheriff, Thermal behavior of the rat before and after feeding. *Proc Soc Exp Biol Med*. 102, 746–748 (1959).
179. E. C. Harding, N. P. Franks, W. Wisden, Sleep and thermoregulation. *Curr Opin Physiol*. 15, 7–13 (2020).
180. M. J. McKinley, D. Martelli, G. L. Pennington, D. Trevaks, R. M. McAllen, Integrating Competing Demands of Osmoregulatory and Thermoregulatory Homeostasis. *Physiology (Bethesda)*. 33, 170–181 (2018).
181. K. Nagashima, Thermoregulation and menstrual cycle. *Temperature*. 2, 320–321 (2015).
182. K. Nakamura, Central circuitries for body temperature regulation and fever. *Am. J. Physiol. Regul. Integr. Comp. Physiol.* 301, R1207–1228 (2011).
183. C. L. Tan, E. K. Cooke, D. E. Leib, Y.-C. Lin, G. E. Daly, C. A. Zimmerman, Z. A. Knight, Warm-Sensitive Neurons that Control Body Temperature. *Cell*. 167, 47–59.e15 (2016).
184. T. Yoda, L. I. Crawshaw, K. Yoshida, L. Su, T. Hosono, O. Shido, S. Sakurada, Y. Fukuda, K. Kanosue, Effects of food deprivation on daily changes in body temperature and behavioral thermoregulation in rats. *Am J Physiol Regul Integr Comp Physiol*. 278, R134–139 (2000).
185. K. Song, H. Wang, G. B. Kamm, J. Pohle, F. de C. Reis, P. Heppenstall, H. Wende, J. Siemens, The TRPM2 channel is a hypothalamic heat sensor that limits fever and can drive hypothermia. *Science*. 353, 1393–1398 (2016).
186. T. A. Wang, C. F. Teo, M. Åkerblom, C. Chen, M. T.-L. Fontaine, V. J. Greiner, A. Diaz, M. T. McManus, Y. N. Jan, L. Y. Jan, Thermoregulation via Temperature-Dependent PGD2 Production in Mouse Preoptic Area. *Neuron*. 103, 309–322.e7 (2019).
187. J. D. Deem, C. L. Faber, C. Pedersen, B. A. Phan, S. A. Larsen, K. Ogimoto, J. T. Nelson, V. Damian, M. A. Tran, R. D. Palmiter, K. J. Kaiyala, J. M. Scarlett, M. R. Bruchas, M. W. Schwartz, G. J. Morton, Cold-induced hyperphagia requires AgRP neuron activation in mice. *Elife*. 9 (2020), doi:10.7554/eLife.58764.
188. Y. Livneh, A. U. Sugden, J. C. Madara, R. A. Essner, V. I. Flores, L. A. Sugden, J. M. Resch, B. B. Lowell, M. L. Andermann, Estimation of Current and Future Physiological States in Insular Cortex. *Neuron*. 105, 1094–1111.e10 (2020).
189. M. Schneeberger, L. Parolari, T. Das Banerjee, V. Bhave, P. Wang, B. Patel, T. Topilko, Z. Wu, C. H. J. Choi, X. Yu, K. Pellegrino, E. A. Engel, P. Cohen, N. Renier, J. M. Friedman, A. R. Nectow, Regulation of Energy Expenditure by Brainstem GABA Neurons. *Cell*. 178, 672–685.e12 (2019).

Abstract (초록)

영양분과 체온 등 체내 환경을 일정 수준으로 유지하는 성질인 항상성은 생명체의 중요한 특징이다. 여러 생물 종 중에서 특별히 동물들은 행동을 통해 자신의 필요를 채워 체내 항상성을 유지하는데, 따라서 항상성을 유지하기 위한 동물 행동을 매개하는 신경 기작을 이해하는 것은 신경생물학 및 생리학의 오랜 과제였다. 수십 년에 걸친 연구들로 많은 부분이 밝혀졌으나, 몇몇 근본적인 항상성 유지 행동을 매개하는 신경회로 기작은 여전히 알려지지 않고 있었다. 본 연구는 섭식 행동과 체온 유지 행동을 조절하는 데 관여하는 새로운 신경회로 기작을 밝힘으로써, 항상성 유지의 신경학적 원리에 대한 이해를 넓히는 것을 목표로 한다.

1장에서는 항상성 개념의 형성과 그 이후 이어진 항상성 조절 신경 기작에 관한 연구의 역사를 간략히 살펴보고자 한다. 2장에서는 소화관의 물리적 감각 신호를 이용하여 섭식을 모니터링하고 이에 따라 음식물의 섭취를 조절하는 후뇌부 신경세포 집단과, 그 집단을 중심으로 말초 신경절에서 시상하부까지 이어지는 장-뇌 신경회로에 관한 연구를 기술한다. 3장에서는 다양한 체온조절 행동에 필수적인 시상하부 신경 집단과 이를 중심으로 체온 조절 행동을 매개하는 신경회로 기작에 관한 연구를 기술한다. 4장에서는 본 논문에 기술된 연구 결과를 간략히 정리하고 그 의의에 관해 살펴본다. 본 연구들은 섭식 행동과 체온 조절 행동을 매개하는 신경회로 기작에 관한 새로운 이해를 더함으로써, 생명 유지에 필수적인 항상성 조절 행동의 신경학적 기반을 완전히 밝히는 데 기여할 것으로 기대한다.